Methods of Printing Passive Analog Beamforming Devices

by

Joseph S. Hyland, B.Eng.

A thesis submitted to the Faculty of Graduate and Postdoctoral Affairs in partial fulfilment of the requirements for the degree of

Master of Applied Science

in

Electrical and Computer Engineering

Carleton University

Ottawa, Ontario

Abstract

Analog beamforming is the process of controlling the amplitude and phase distribution across an antenna array to produce focused EM radiation. There are many ways of accomplishing this, but this thesis focuses on printing techniques to produce beamforming devices. The methods of production used for this work includes 3D polymer printing, PCB fabrication and knife tracing with copper cladding and tape. Three types of devices are designed and fabricated for this work including Luneburg lenses, Butler matricies and ferroelectric varactors. The Luneburg lenses are produced through 3D printing processes and measured in the far-field using with an anechoic chamber. Two different Butler matricies are designed and presented, one is designed at 2.4 GHz on Rogers 3006 substrate and fabricated using a knife tracing printing process. Radiation pattern measurements are made for this matrix in the far-field using an anechoic chamber. The other matrix is designed using lumped components and printed with standard PCB fabrication. Phase and amplitude measurements are made for this matrix with a VNA. Ferroelectric material for the varactors is produced through 3D printing and the electrodes are made from copper tape with knife tracing. A high frequency varactor is produced using knife tracing and measured using 250 um pitch circuit probes for flexible applications.

Acknowledgments

I would like to thank my supervisor Prof. Rony Amaya for all his support throughout my academic career, both getting me to the point of pursuing graduate school and seeing me through. I have learned a phenomenal amount from him over the last 5 years and owe a lot of where I am today to his guidance and expertise. I would also like to thank my NRC supervisors Bhavana Deore and Chantal Paquet for their tireless work supporting my project and without whom my thesis work would not have been possible.

To my fellow team members Shakeeb Abdullah, Wenyu Zhou, Nima Javanbakht and Jorden Labossiere thank you for your continued support and advice throughout this adventure.

I would also like to acknowledge the support I received from the team at NRC including Tom Lacelle, Luke Young and Derek Aranguren van Egmond for their help in production and optimising designs.

I am grateful to the committee members Prof. Shulabh Gupta, Prof. Emad Gad and Prof. Steven McGarry for taking the time to attend my defense and providing me with feedback to strengthen my thesis.

A huge thank you to Nagui Mikhail for being a huge support my entire time at Carleton University. He continually supported my projects provided solutions to problems big and small.

Finally, I would like to thank my friends and family for all the support they provided throughout my journey and to my past supervisor Dr. Ryan Griffin who played an instrumental role in my education and development both personally and professionally.

Contents

List of Tables

List of Figures

Acronyms

3D	Three Dimensional
ADC	Analog to Digital Converter
BST	Barium Strontium Titanate
CAD	Computer Aided Design
CNC	Computer Numerical Control
DC	Direct Current
DMM	Digital Multimeter
EM	Electromagnetic
EMI	Electromagnetic Interference
FDM	Fused Deposition Modelling
FEM	Finite Element Method
FPGA	Field Programmable Gate Array
GSG	Ground Signal Ground
HFSS	High Frequency Structure Simulator
LTCC	Low Temperature Co-fired Ceramic
RF	Radio Frequency
SLA	Stereolithography
SOLT	Short Open Load Through
SRF	Self Resonant Frequency
VNA	Vector Network Analyser

Nomenclature

c	speed of light in a vacuum 3.00 $\times 10^8$ m/s
r, R	radius m
d	distance m
h	height m
W	width m
L, ℓ	length m
A	area m^2
ε_r, ε_{eff}	relative, effective permittivity
tanδ	loss tangent
f, f_0	frequency, centre frequency Hz
Q_0	unloaded quality factor
α_T	transmission line attenuation constant
π	ratio of circumferande to diameter 3.14159...
Y_0	characteristic admittance Siemens
Z_0, Z_L, Z_{in}	characteristic, load, input impedance Ω
β, k_0	wavenumber, free space wavenumber m^{-1}
λ_g, λ_0	guided, freespace wavelength m
E	electric field V/m

Chapter 1

Introduction

Frequency spectrum is an intangible commodity in an ever-growing demand as the number of devices that are communicating wirelessly using EM radiation increa. Several solutions have been employed to address this issue with one of the more recent solutions being the introduction of 5G networks [1]. Fifth generation (5G) cellular networks alleviate strain on the frequency spectrum in two major ways. Moving to unused spectrum directly opens up bandwidth by making new domains accessible, but higher frequency bands also allow for more efficient use of spectrum through the use of phased arrays for beamforming on mobile devices [1][2]. Two factors that impact the performance of phased array systems are 1) the number of radiating elements and 2) their separation relative to their operating wavelength. Since antenna size typically scales linearly with wavelength, operating in a higher frequency band allows an increased number of radiating elements to be spaced optimally for beamforming. By focusing radiation at both ends of a wireless link, adjacent users can reuse frequency domain without interference.

The work presented in this thesis focuses on beamforming methods and their production through convenient printing techniques. While the devices produced in this work operate in the UHF, S and X band frequency ranges, they can be scaled to higher frequencies with smaller resolution. This is particularly true of the Cricut process where the size of trans-

mission lines directly scale with wavelength; for the 3D printing process, higher frequencies may begin to reduce the homogeneity of the cells but higher resolution for the Cricut cutter would be required first to characterize the materials up to the design frequency [3].

One method of beamforming investigated in this thesis is the use of antenna arrays. Radiation from an antenna array can be described as a combination of the individual element patterns and an array factor created by the unique positioning of elements and distribution of phase and amplitude across them. For an $M \times N$ array the array factor can be described by summing over the radiation contributions of each element as [4]

$$AF(\theta, \phi) = \sum_{m,n=0}^{M,N} A_{mn} exp(jk(\mathbf{r}'_{mn} \cdot \hat{r})) \tag{1.1}$$

where A_{mn} is a complex constant relating to the phase and amplitude feeding the mn^{th} element, k is the wavenumber and $\mathbf{r}'_{mn}$ is the radius vector from the mn^{th} element to the field point. To increase directivity for an array the number of elements can be adjusted or the phase progression can be tuned with larger numbers in either case typically narrowing radiation lobes. Increasing the number of elements typically results in more loss while larger phase progressions can create undesired grating lobes. Another method of increasing directivity is to use an antenna lens. Devices such as the Luneburg lens have been shown to increase the directivity of radiating elements providing an additional factor to control [5].

Traditional methods of producing electronics often require designs to be sent out for production. This can be a challenge for rapid prototyping as production times can delay the development process. The work presented here demonstrates several methods of rapid fabrication for RF beamforming circuits such as 3D printing and knife tracing with copper tape. Multiple methods of 3D printing exist and have been used in the production of electronics. Two common methods are Fused Deposition Modelling (FDM) and vat photopolymerization [6][7]. FDM involves the deposition of polymer filament while vat photopolymerization involves the hardening of polymer resin through application of a laser against a build plate.

For the work presented here a subset of vat photopolymerization known as stereolithography was used for its high precision and the ability to dope resin with functional materials [8].

1.1 Thesis objectives

The objectives of this thesis are:

1. Characterize the electrical properties of SLA printable resin to allow for the design and production of a 3D printed Luneburg lens antenna for improved gain and beamforming.

2. Introduce an alternative method of circuit fabrication using a CNC knife tracing tool Design and produce alternative beamforming circuitry such as a Butler matrix through printing or other convenient methods of fabrication.

3. Design and produce 3D printed varactors for circuit tuning.

1.2 Thesis contributions

The work done in this thesis has lead to the following contributions:

1. Characterization of Formlabs resin for SLA printing. The permittivity and loss tangent for resin doped with nano-particles was characterized up to 9 GHz leading to the following publication and submission:

    - **J. S. Hyland**, S. Abdullah, B. Deore, W. Zhou, C. Paquet, G. Xiao, R. E. Amaya, "Advancement of Printed Electronics for Use in IoT Applications and Wireless Health Care Devices" submitted to IEEE's Canadian Conference on Electrical and Computer Engineering.

    - B. Deore, K.L. Sampson, T. Lacelle, N. Kredentser, J. Lefebvre, L. S. Young, **J. Hyland**, R. E. Amaya, J. Tanha, P. R. L. Malenfant, H. W. de Haan and

C. Paquet, "Direct printing of functional 3D objects using polymerization induced phase separation". In: Nature Communications 12.1 (2021), p. 55. doi: 10.1038/s41467-020-20256-3.

2. Characterization of conductivity for deposited silver ink. Determining the conductivity of printed silver ink at x-band lead to the following publications:

   - S. Abdullah, G. Xiao, **J. Hyland**, W. Zhou and R. E. Amaya, "A First Implementation of a Single-Layer 4×4 Butler Matrix on Flexible PET Using Printed Silver," 2021 IEEE International Symposium on Antennas and Propagation and USNC-URSI Radio Science Meeting (APS/URSI), 2021, pp. 1385-1386, doi: 10.1109/APS/URSI47566.2021.9703776.
   - S. Abdullah, **J. Hyland**, W. Zhou, G. G. Xiao and R. E. Amaya, "A New Closed-Form Approach (Equation) for Accurately Predicting the Efficiency of Square Patch Planar Antennas," 2021 IEEE 19th International Symposium on Antenna Technology and Applied Electromagnetics (ANTEM), 2021, pp. 1-2, doi: 10.1109/ANTEM51107.2021.9518992.

1.3 Thesis organisation

The rest of this thesis is organised as follows:

- Chapter 2 provides background on 3D printing processes.
- Chapter 3 provides details on the characterisation of 3D printed materials and printing methods used in this work.
- Chapter 4 presents the design, simulation, fabrication and measurement of three Luneburg lens antennas.

- Chapter 5 presents the design, simulation, fabrication and measurement of a microstrip line Butler matrix and antenna array followed by a lumped element Butler matrix.
- Chapter 6 presents the design, simulation, fabrication and measurement of ferroelectric varactor circuits.
- Chapter 7 concludes this thesis with a discussion of future work.

Chapter 2

Methods of 3D Printing

Three dimensional (3D) printing has become a popular method for rapid production. There are several common methods of 3D printing by depositing filament through and extrusion device or polymerising a powdered or resin material [9]. In general the methods of 3D printing can be broken in to three main categories depending on the method by which materials are combined: selective binding, selective deposition, and selective solidification [10]. An example of each printer type can be seen in Figure 2.1.

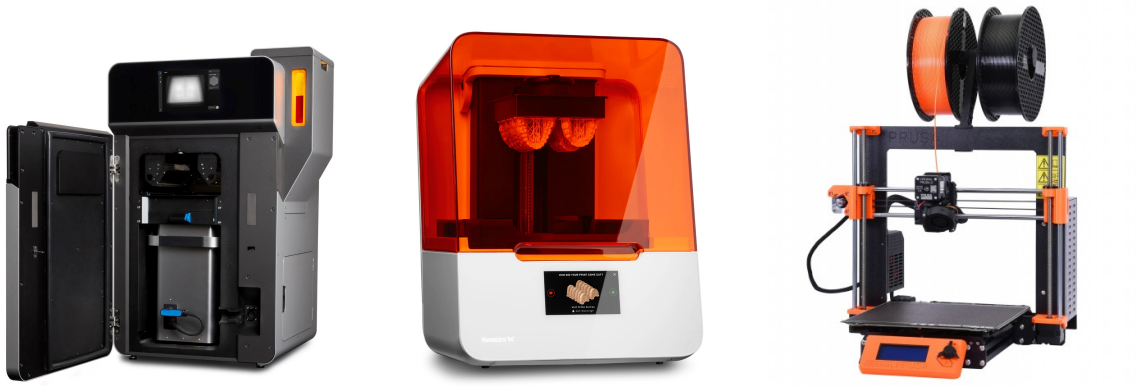

(a) Formlabs Fuse 1 (b) Formlabs Form 3B (c) Prusa i3 MK3S

Figure 2.1: Example 3D printers with Formlabs Fuse 1 selective laser sintering printer (a) Formlabs Forb 3B stereolithography printer (b) and Prusa i3 MK3S fused deposition modeling (c) [11][12]

2.1 Selective Laser Sintering

Selective laser sintering (SLS) is a process by which powdered polymer is deposited in thin layers and selectively bonded to the layers below. A laser is a common tool for the bonding of powdered polymer [10]. The SLS printing process is depicted in Figure 2.2.

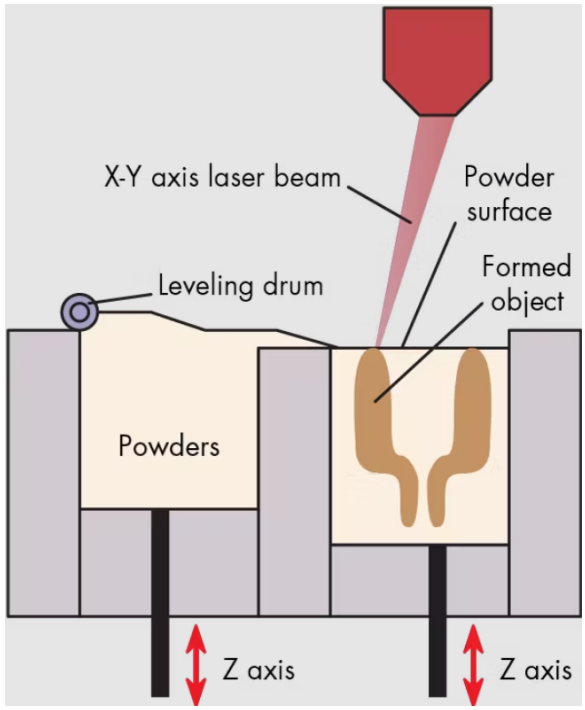

Figure 2.2: Selective laser sintering process [13]

2.2 Stereolithography

Stereolithography (SLA) is a process by which a liquid polymer resin is solidified against a build plate to create a model [10]. The SLA printing process is depicted in Figure 2.3. These printers are a useful tool for printing substrates due to the possibility of doping resins with foreign materials [8].

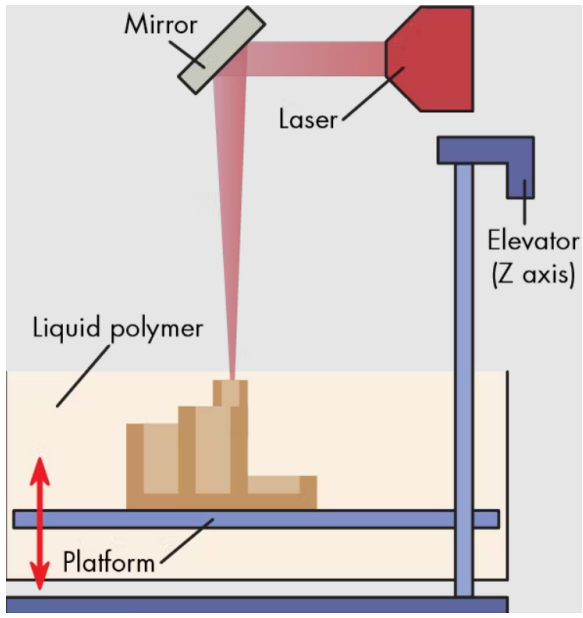

Figure 2.3: Stereolithography process [13]

2.3 Fused Deposition Modeling

Fused Deposition Modeling (FDM) is a process by which a polymer filament is deposited only where material is desired to form a model. When the filament reaches the extruding element it melts enough to be fused to the hardened layer below allowing a model to be built up [14].

2.4 Literature Review

Various methods of 3D printing electronics have been investigated. Some methods focus on dielectrics while others have been able to integrate conductive materials into the substrate to form electrical traces. Some examples of such projects will be reviewed here. Initially a review of dielectric based printing processes followed by some methods of embedding conductors.

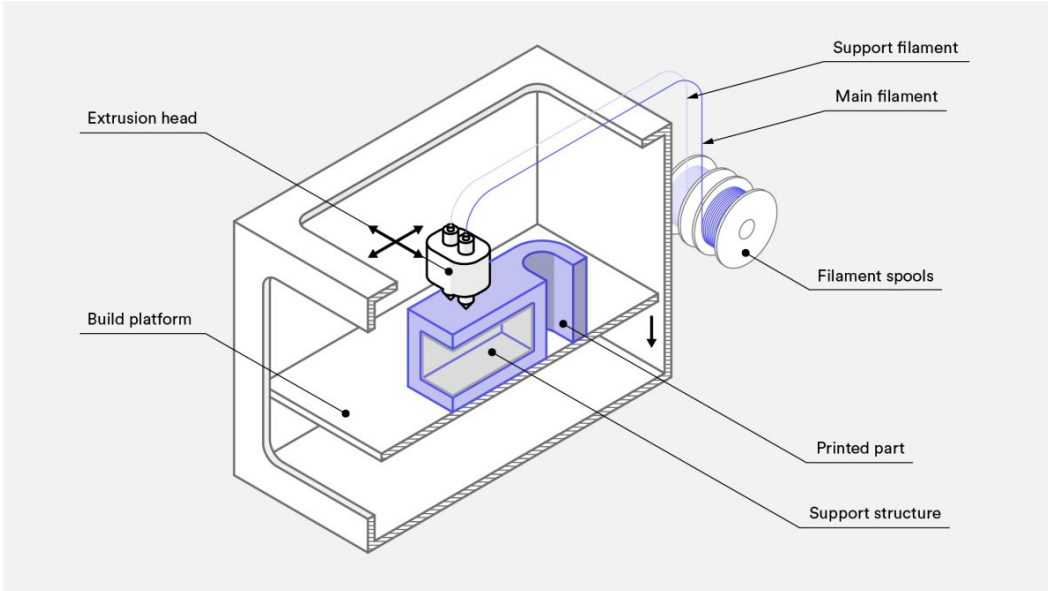

Figure 2.4: Fused Deposition Modeling process [14]

2.4.1 Dielectric printing processes

Some processes have used FDM printing to create electronics such as in [15]. This processed used FDM to create a spherical Luneburg lens at x band with the density varied across the radius of the lens to create an effective permittivity tapering profile. When fed with an open ended waveguide the combined system was capable of producing a total peak gain of 20.5 dBi (15 dB more than the waveguide without lens). Various other projects have produced similar lenses and a summary of their performance can be seen in Table 2.1.

Table 2.1: Summary of performance for dielectric printing processes applied to the production of Luneburg lenses.

Reference	Frequency (GHz)	Gain (dBi)
[15]	8 - 12	20.5
[16]	7 - 11	18
[17]	6	21.5
[18]	26 - 40	20
[19]	10	15

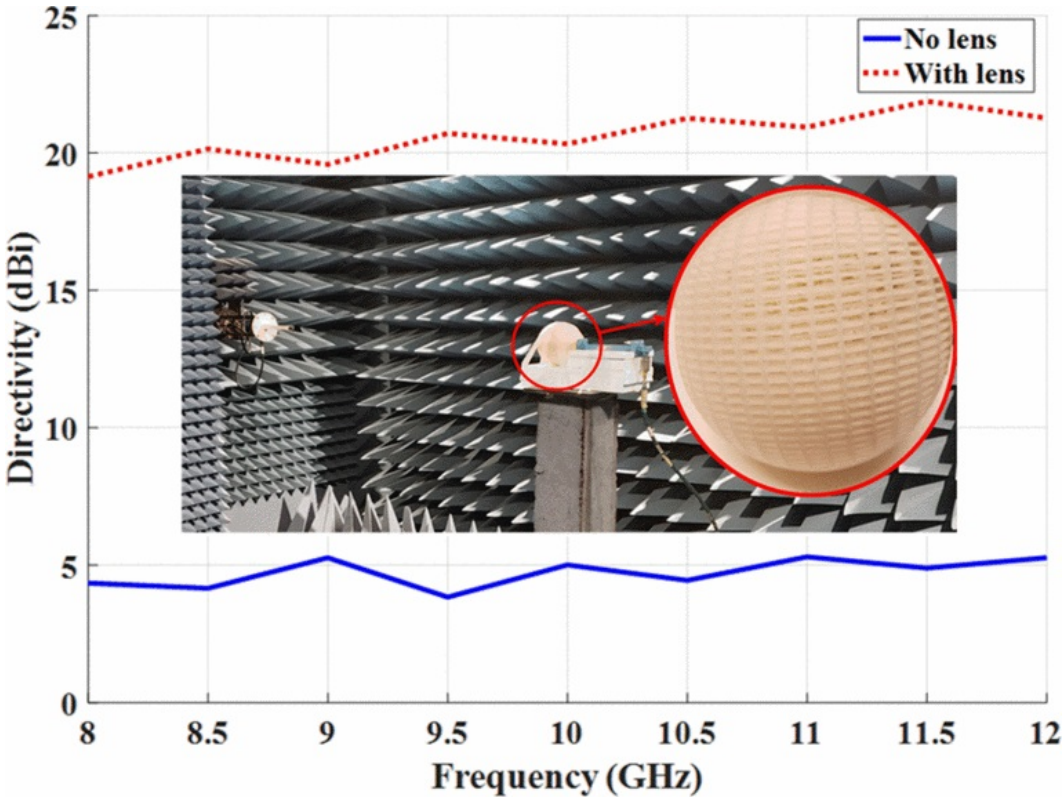

Figure 2.5: A fabricated lens under test and the measurement results for directivity of a standard X band open waveguide with and without lens. [15]

2.4.2 Conductor embedding printing processes

Various projects have been undertaken to embed conductors into 3D printed substrates and some have also included integrated circuits (ICs) such as shown in Figure 2.6. This project was able to generate the conductive traces using a direct ink writing technology and electrically connecting to surface mount ICs.

Another project used a conductive metal paste characterised in [21] to embed traces within mechanically stretchable substrate [22]. This substrate was then used to produce a strain sensor and embedded oscillator IC as shown in Figure 2.7

Conductors have also been added to 3D printed substrates through hybrid printing processes where a conductor negative is left embedded within a design and filled with conductive material after printing. This process was used to create a six-sided block substrate with integrated microprocessor, accelerometer, resistors and LEDs [23].

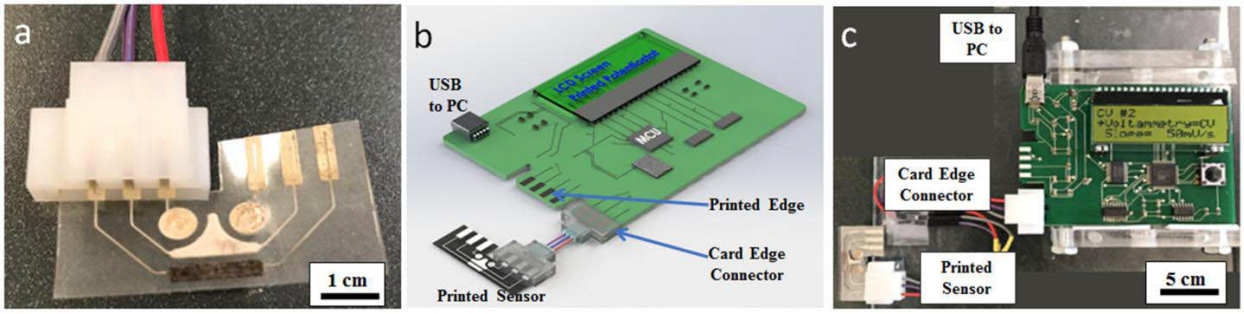

Figure 2.6: Printed lactate biosensor prototype with enzyme-covered electrode and chloridized electrode (a) design concept (b) and prototype with lactate sensor (c). [20]

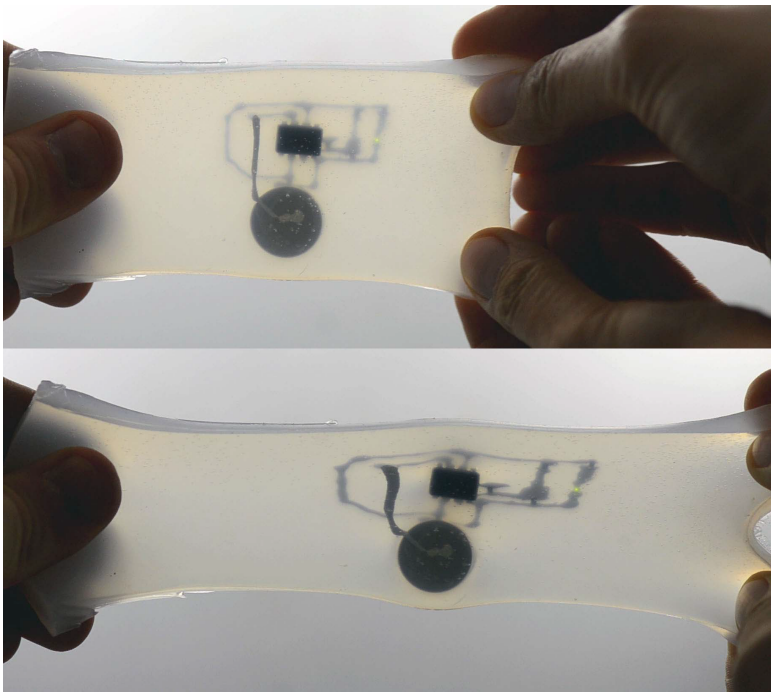

Figure 2.7: Printed, multi-layer stretchable oscillator circuit using liquid metal paste interconnects, shown in un-stretched and stretched states. The circuit continues to function while being stretched by hand. [22]

Bulk conductive copper has been added to 3D printed substrates with enough resolution to land 0.5 mm pitch QFN components as demonstrated in [24]. This process was able to use conductive copper strips embedded with in the substrate to create connections between layers and a surface land pattern for components. The printed QFN land pattern with 0.5 mm pitch can be seen in Figure 2.9.

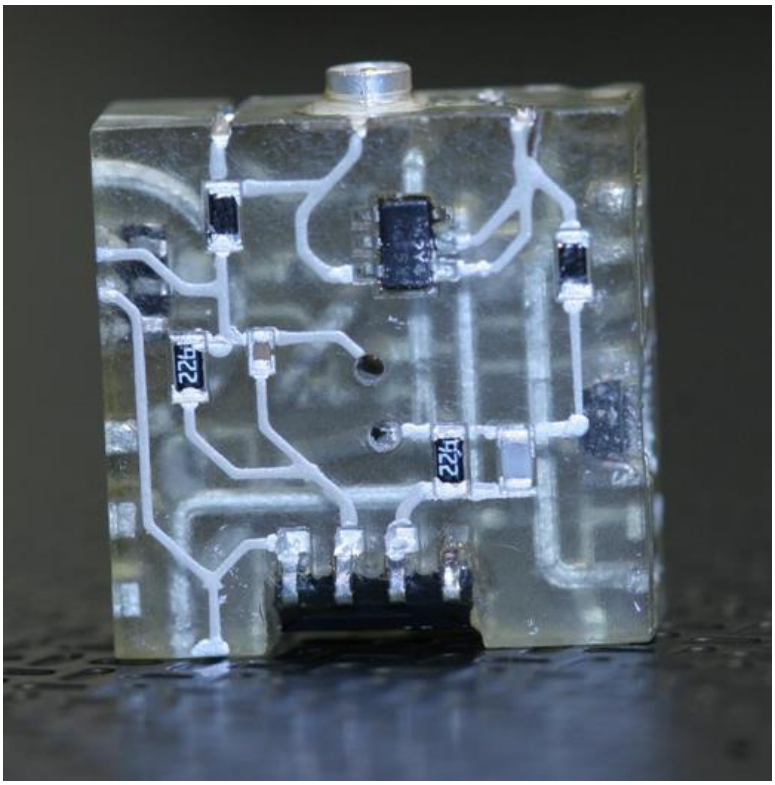

Figure 2.8: 3D printed signal conditioning circuit. [23]

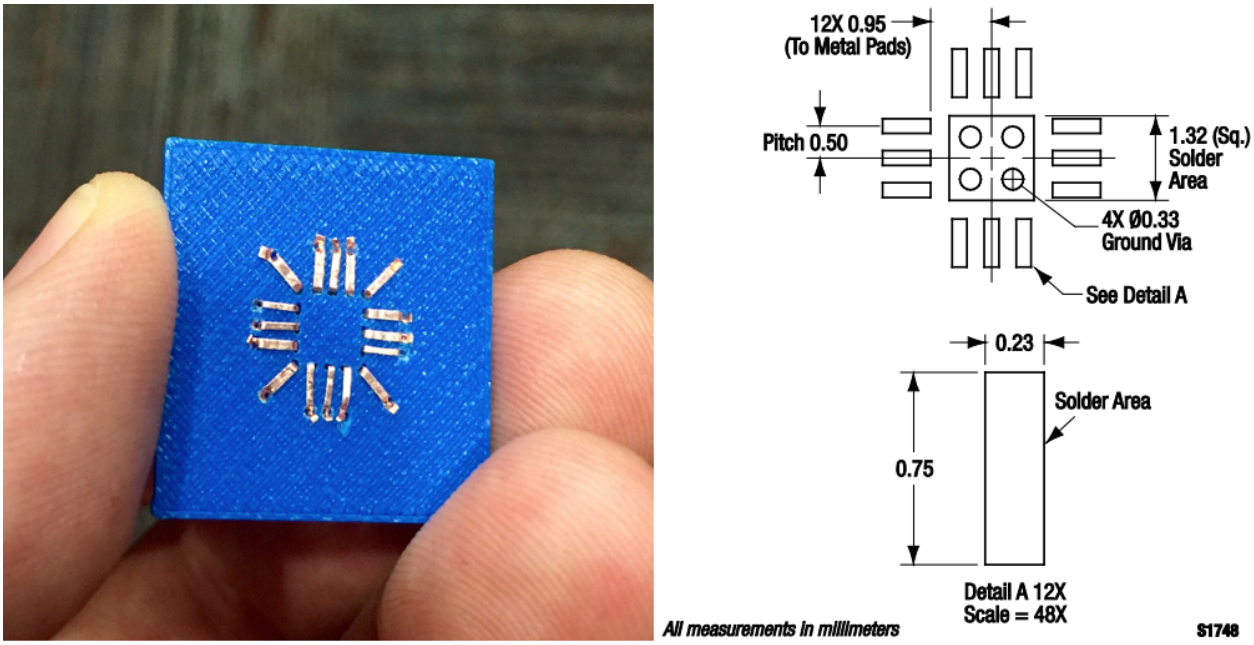

Figure 2.9: Top down view of structure where excess foil is folded down to provide a surface mount landing footprint for soldering a 12 pin QFN device with grounded corners (left) and manufacturers recommendations (right). [24]

2.5 Other printing methods

While 3D printing is the main focus of investigation presented in this thesis another significant source of printing used is the Cricut cutter knife tracing tool [3]. A knife tracing tool is useful for rapid prototyping of electronics and can be used to pattern conductors with roughly 300 um resolution. A picture of the knife tracing tool used in this work can be seen in Figure 2.10. This cutter is used in this work for production of ring resonators, Luneburg

Figure 2.10: Cricut Maker knife tracing tool [3]

lens platting covers, some varactor plates, a Butler matrix, and a patch antenna array.

Chapter 3

Characterisation of Materials and Printing

The process of creating electronics through 3D printing is not new, yet many 3D printable materials have, as of yet, undefined electrical properties [25][26][27]. This leaves the process of chacterisation up to the designer as the first step in a new 3D printing design. For most designs the characteristics of interest are material permittivity (ε_r) and loss tangent ($tan\delta$), both vary as functions of frequency across the design bandwidth. While some materials have magnetic properties that present a non-unity value for relative permeability, they are not usually printable polymers. As a result the materials characterised for the designs presented here will be assumed to have relative permeability values of one and the permittivity and loss tangent will be the properties of interest.

Materials can be characterised in a variety of ways including measurements of the phase shift and loss across a transmission line, or the phase shift and return loss from an open or short circuited stub; but the most common methods involve measurement of a resonator. There are many ways to make a resonator circuit to determine the dielectric properties of a material, but some of the most popular include T-resonators, split ring resonators and ring resonators coupled either from the end as a series element or from the side as a shunt stub

[28][29][30]. While all these methods can be effective, this investigation will focus on the end fed ring resonator for its simplicity and accuracy of characterisation [30].

3.1 Ring resonators

A ring resonator is a two port guided transmission line structure that can can be used to determine the properties of the dielectric it is mounted on. It is an ideal structure for characterising materials as both the location and shape of the resonance peaks can be used to obtain valuable information about the dielectric constant and the losses of the material [30]. The basic structure of the end fed ring resonator includes two feeding transmission lines coupled to the ring on either side through a gap as seen in Figure 3.1. By coupling

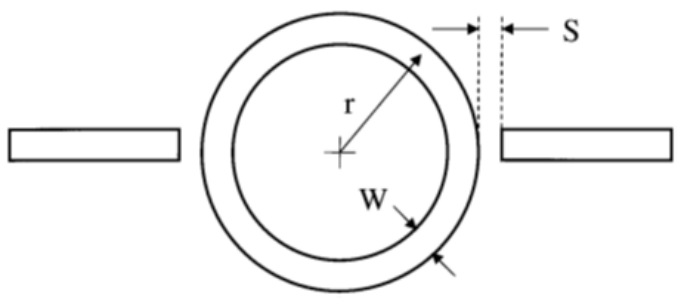

Figure 3.1: Ring resonator outline and parameters [30]

to the ring it allows the resonance to be measured while reducing the loading effect of the source and load impedance. A balance must be struck when designing the gap as increasing the coupling capacitance will allow more energy to couple through the circuit while simultaneously increasing the loading effect of the measurement apparatus. This can either reduce the sensitivity to unloaded quality factor or reduce sensitivity to the unloaded resonance [31].

3.2 Calibration method

Calibration for the ring resonator measurements was done using an SOLT (short, open, load, through) calibration. An alternative to SOLT would have been a TRL (through, reflect, load) calibration, but the quality of this calibration depends on the tolerances of the conductor and dielectric dimensions. To remove the added error from manufacturing tolerances the SOLT calibration process was used. The single end terminations were taken from the Agilent 85052D calibration kit as shown in Figure 3.2. To calibrate the through measurement a

Figure 3.2: Agilent 85052D 3.5 mm calibration kit short, open and broadband load [32]

section of transmission line with the characteristic impedance of the feedlines and twice the electrical length was used. This de-embedding was performed to move the reference point for measurement to the edges of the coupling gaps. Isolation calibration measurements were omitted for this process.

3.3 Ring resonator fabrication

Fabrication of the ring resonators was performed using a Cricut knife tracing tool [3]. This is a commercially available tool commonly used for arts and crafts but also happens to have an excellent application for electronics.

By using copper tape as the conductive material the excellent bulk conductivity of copper can be used to produce almost no conductor losses. The cutting and placement of copper tape was done using a low adhesive transfer tape as seen in Figure 3.3. By using the transfer

Figure 3.3: Transfer tape cutting process for placing ring resonators

tape as backing to form a decal the rings could be cut and then stuck to the surface of the substrate under test with fine precision and without scoring knife marks around the conductor. This method was used to create rings as shown in Figure 3.4 which depicts a ring resonator on a commercial substrate and a printed control substrate. This process allowed high conductivity copper ring resonators to be placed on delicate 3D printed substrates.

3.4 Measurements and results

Ring resonantor measurements were captured as a two port s-parameter measurement on a VNA. An example of a ring resonantor being measured on a substrate doped with graphene can be seen in Figure 3.5. The s-parameters were extracted from the VNA for analysis. With the s-parameters characterising the function of the ring resonator the extraction of permittivity and loss tangent data for the substrate was modelled off the process described in [30]. A parallel lumped model of the ring resonator was used to describe its operation during regions of maximum transmission when the circumference of the ring is equal to an integer multiple of a wavelength. A model of the lumped circuit used to model the ring can

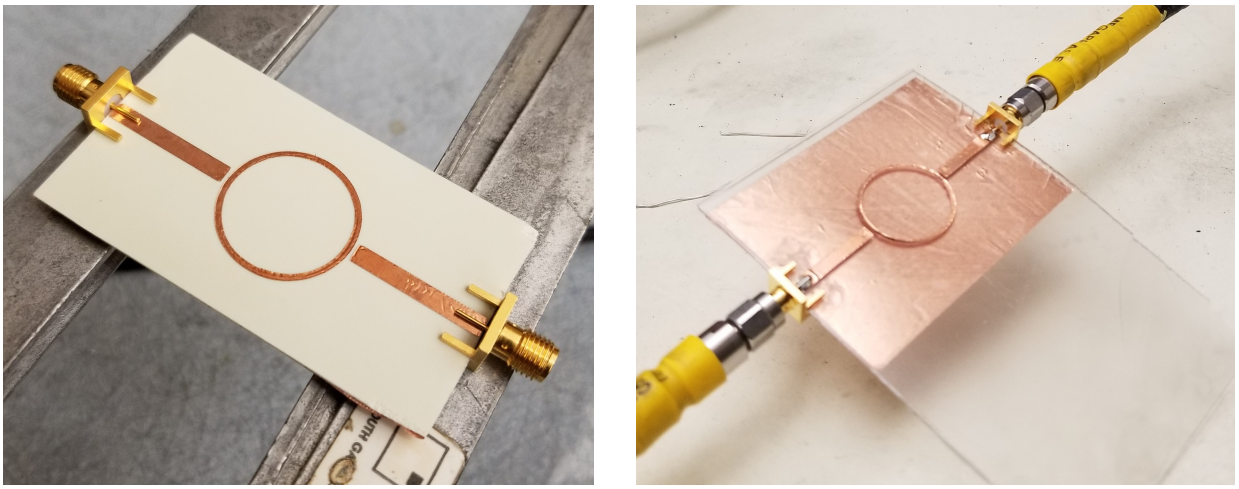

(a) (b)

Figure 3.4: Copper tape ring resonators deposited on commercial RO3006 substrate (a) and undoped Formlabs control resin (b)

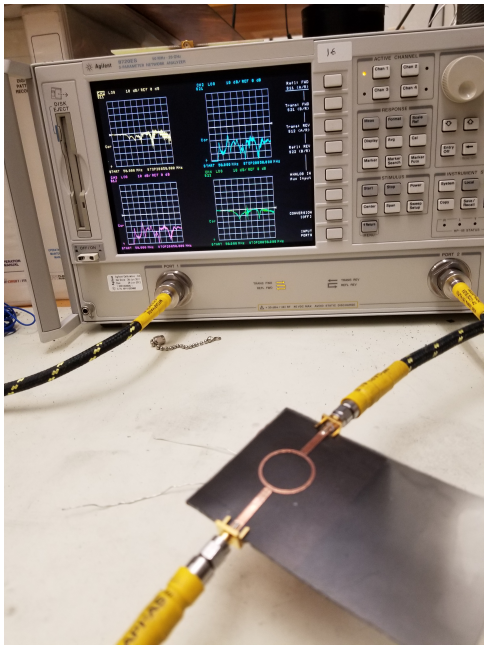

Figure 3.5: Ring resonator VNA measurement setup

be seen in Figure 3.6. This model not only accounts for the parallel resonance behavior of the ring at peak transmission but also the coupling gaps between the ring and the feedlines. These gaps can be seen modelled as gap capacitors C_g and parallel capacitors C_p. The values of these capacitors were estimated using an ADS [33] simulation so their effects could be removed from the calculations. To fit the model to the measurements a signal analysis

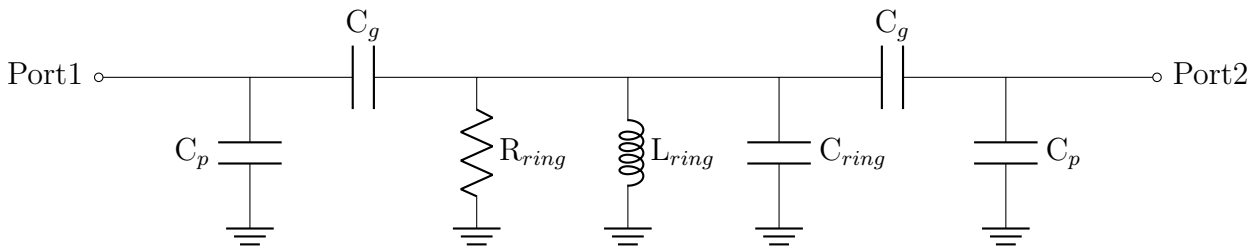

Figure 3.6: Lumped model of ring resonator at peak transmission [30]

was done to determine the transfer function of the lumped circuit model. Shunt values L, C, and R were then used as optimization parameters in MATLAB to minimise the square of the difference between the fit function and the measured data using *fminbnd*. A ring resonator measurement on the control sample along with a function fit to the first resonance peak can be seen in Figure 3.7. This plots shows a clear resonance at 3.2 GHz with some minor ripple

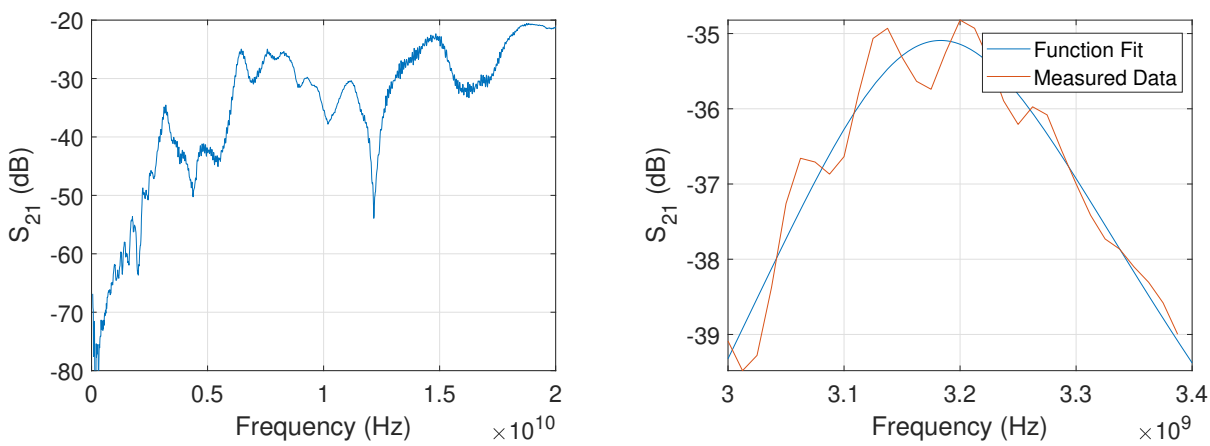

(a) (b)

Figure 3.7: Measured ring resonator S-parameters for control substrate

possibly due to inaccuracy in the calibration causing the presented impedance to oscillate about 50 Ω. Higher order resonances can be seen with reducing clarity around 6 GHz and 9 GHz. The lumped model was fit to the data at the second and third order resonances as well, but for most substrates no fits were made above the third order resonance. This gives permittivity and loss tangent data at approximately 3, 6 and 9 GHz for the printed substrates.

Once values for R, L and C were determined using the MATLAB [34] fit the permittivity

and loss tangent were found as follows. Knowing the resonance frequency of the ring allows the effective permittivity to be easily calculated knowing the circumference of the ring is an integer multiple of the guided wavelength as [30]

$$\varepsilon_{eff} = \frac{cN}{2\pi r f_{0N}} \tag{3.1}$$

where N is an integer giving the resonance order and f_{0N} is the centre frequency of the Nth order resonance. To extract the relative permittivity of the substrate from the effective value found above a another equation relating the two must be used. Calculating the effective permittivity as [35]

$$\varepsilon_{eff} = \frac{\varepsilon_r + 1}{2} + \frac{\varepsilon_r - 1}{2}\left[\frac{1}{\sqrt{1 + \frac{12d}{W}}}\right] \tag{3.2}$$

where d is the dielectric height and W is the trace width allows the relative permittivity to swept in MATLAB to match the values. This relative permittivity value can then be assigned to the substrate for the centre frequency of the resonance.

To determine the loss tangent of the substrate, unloaded quality factor was calculated first. The unloaded quality factor differs from the loaded quality factor in that it neglects the effects of the loading ports and circuitry. It represents the losses of the resonant circuit alone. Using the values for R and L from the resonant modelling circuit allows the unloaded quality factor to be calculated as [35]:

$$Q_0 = \frac{R}{2\pi f_0 L} \tag{3.3}$$

(although the capacitor could have been used in place of the inductor for this calculation since the point of operation is at resonance). From the unloaded quality factor, the atenuation constant of the transmission line can be calculated as [30]:

$$\alpha_T = \frac{\pi N}{Q_0 L} \tag{3.4}$$

where L is the resonator inductance. From the attenuation constant for the ring transmission line the substrate loss tangent can be calculated as [35]:

$$tan\delta = \frac{\alpha_T c}{\pi\sqrt{\varepsilon_r} * f_0} \tag{3.5}$$

which completes the electrical characterisation of the substrate. A summary of the measured parameters for the printed substrates can be seen plotted in Figure 3.8.

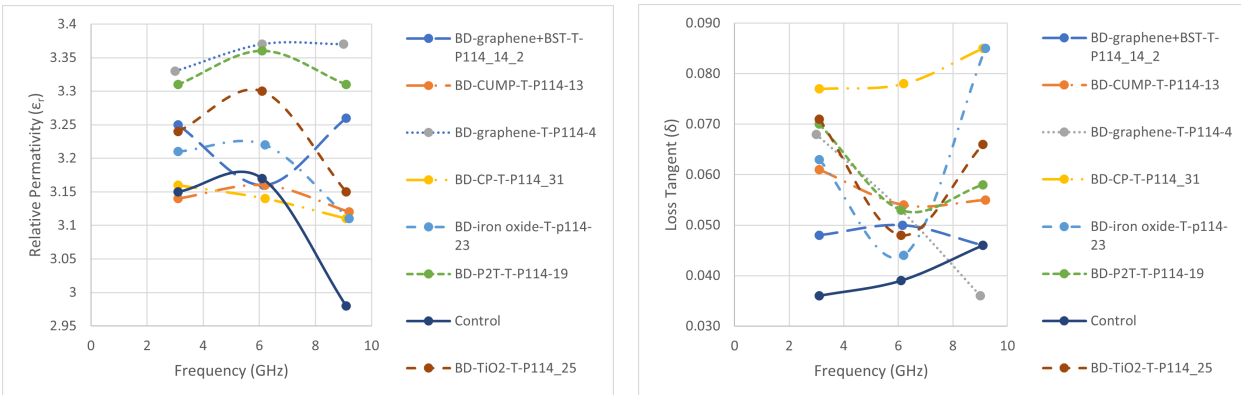

(a) Permittivity (b) Loss tangent

Figure 3.8: Measured electrical properties of printed substrates with material properties presented in Table 3.1. The loss tangent presented here also includes conductor losses in the copper tape, but these are assumed to be small relative to substrate losses.

Table 3.1: Summary of characterised SLA printed substrates

Label	Doping Material	Percent Weight
BD-graphene+BST-T-P114_14_2	Graphene and BST	0.1% and 0.2%
BD-CUMP-T-P114-13	Copper	0.1%
BD-graphene-T-P114-4	Graphene	0.1%
Control	None	NA
BD-CP-T-P114_31	PDOT ink	0.2%
BD-iron oxide-T-p114-23	Iron Oxide	0.2%
BD-P2T-T-P114-19	Piezoelectric Particles	0.2%
BD-QD-T-P114_36	Silver Selenium	Quantum Dots
BD-TiO2-T-P114_25	Titanium Oxide	0.2%

These plots include a variety of doped substrates that were not used for any of the designs presented in this work. The main substrate that was used in the design of the Luneburg

lens antennas, which will be presented later, was the control. This substrate was used for its lower value of permittivity and loss tangent both of which are desirable for the Luneburg lens. A summary of the control substrate electrical properties can be seen in Table 3.2.

Table 3.2: Formlabs Control substrate electrical properties

Frequency	Er	Tanδ
3.1 GHz	3.15	0.036
6.1 GHz	3.17	0.039
9.1 GHz	2.98	0.046

Chapter 4

Guided Luneburg Lens Design

This chapter will present the design of a 3D printable Luneburg lens. With a homogeneous dielectric material a density variation method will be analysed and used to taper the permittivity of the lens. Finally the printed lens will be presented along with far-field radiation pattern measurement.

4.1 Lens design equations

The core design equation for the Luneburg lens governs the tapering of permittivity across the radius. This tapering can be described as [36]

$$\varepsilon_r(r) = 2 - \left(\frac{r}{R}\right)^2 \tag{4.1}$$

where R is the total radius of the lens. This is a fairly simple design requirement to have the lens permittivity taper across its radius. A more challenging aspect of the design is creating variation in the substrate to achieve this tapering. Various methods have been employed to this effect, including stepping the permittivity with physically distinct materials and tapering the density of a homogeneous dielectric [37][38]. Either of these methods can be effective, but to take advantage of 3D printing for the production of the lens it will be designed with

a single dielectric and the density will be varied to create an effective permittivity gradient.

To taper the density of the dielectric there are a number of geometries available that can accomplish the task. In general the process involves creating air pockets within a substrate and varying the size or number of them to alter the effective permittivity. Some geometry examples of how the density of a substrate can be varied are shown in Figure 4.1. This plot

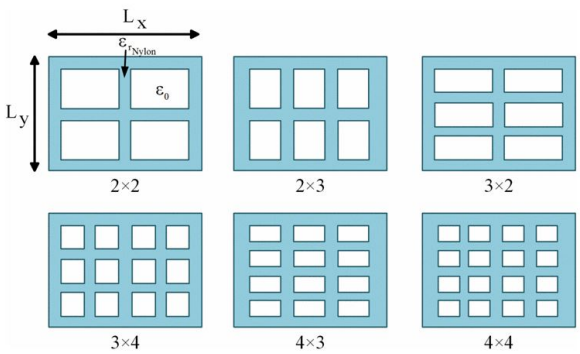

(a) Dielectric density [15]

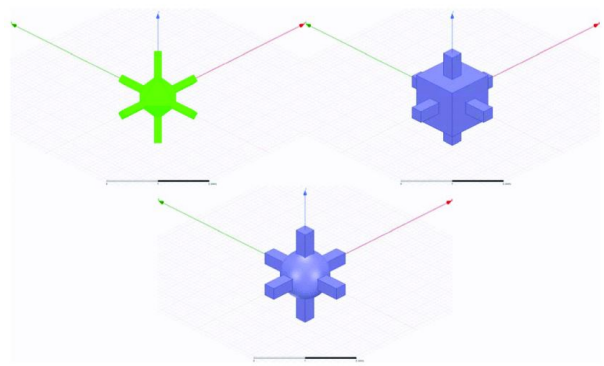

(b) Dielectric density [7]

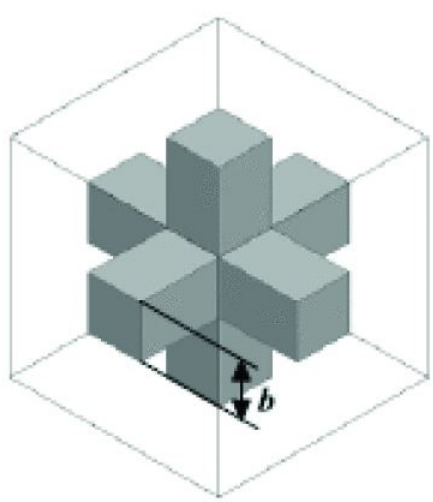

(c) Dielectric density [39]

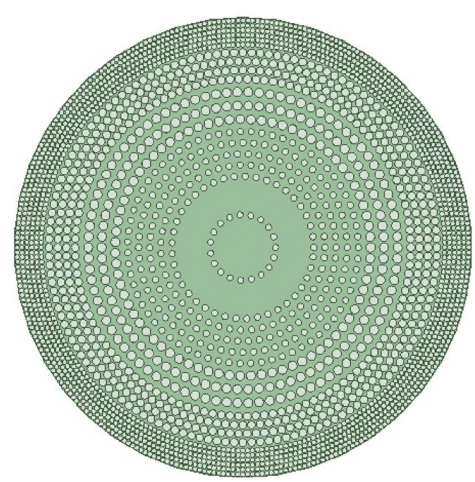

(d) Dielectric density [5]

Figure 4.1: Dielectric density variation techniques

shows a variety of geometries for density tapering. For this investigation it is desired to have a single cell with uniform dimensions so that it can be easily assembled into a model for printing. This makes a geometry similar to the ones shown in Figures 4.1b,c ideal.

4.2 Simulation and radius impact

To analyse the effect of lens radius on performance, an HFSS model was made as shown in Figure 4.2.

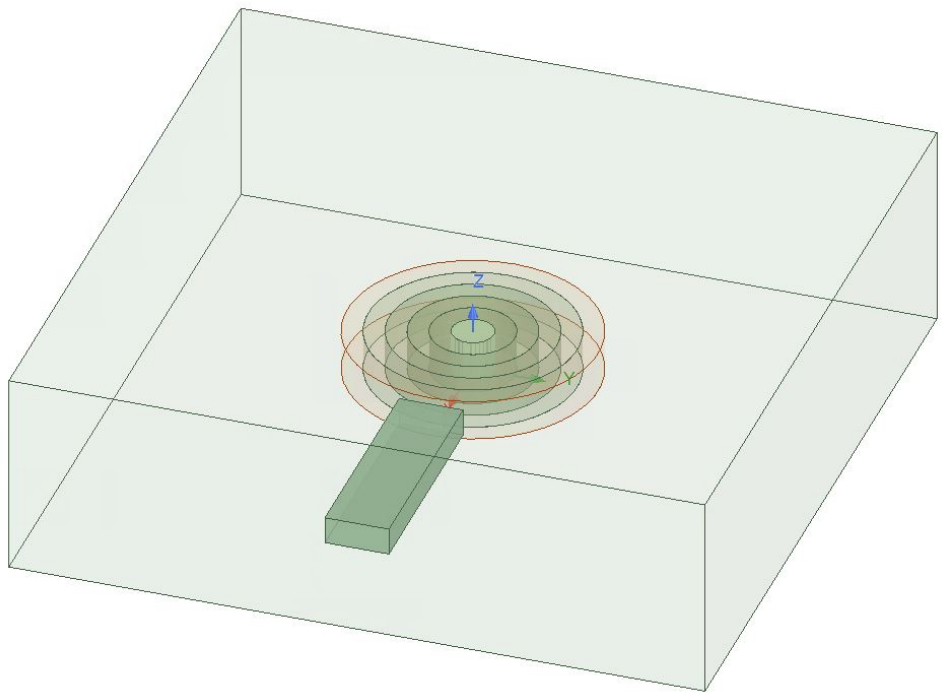

Figure 4.2: HFSS Luneburg lens model with 6 concentric rings each exhibiting a permittivity value associated with its median radius to create a stepped gradient lens.

4.3 Dielectric cell density

To create a permittivity taper across the radius of the lens there are a number of techniques that have been used. Metamaterials have become a popular choice for creating a permittivity gradient. Some designs have been used to add capacitance to a substrate and increase its

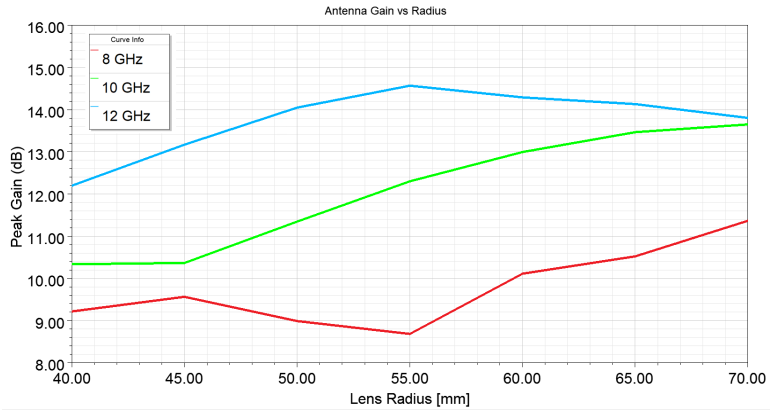

Figure 4.3: Peak gain across radius sweep for simulated Luneburg lens

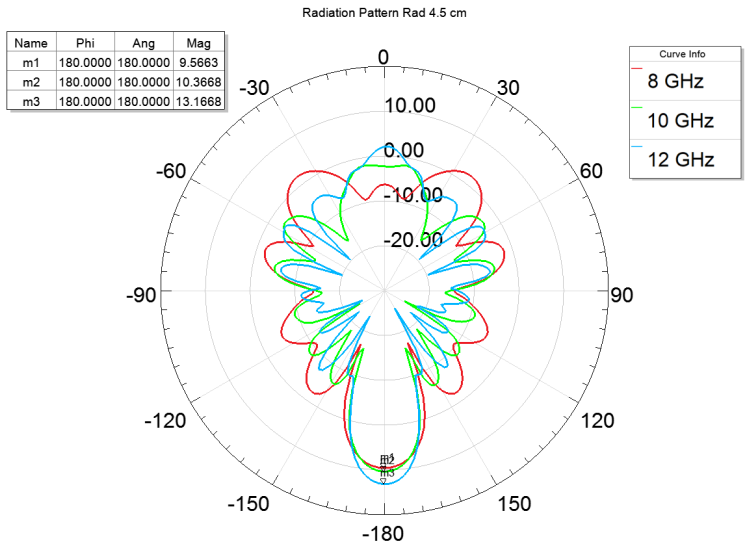

Figure 4.4: Simulated radiation pattern for Luneburg lens with 4.5 cm radius where markers M1-M3 show the peak gain at frequencies 8 - 12 GHz respecively

ability to store electrical energy as in [37][40]. Split ring resonators have also been used with transmission lines to simultaneously control the storage of electrical and magnetic energy as in [41][42]. A stepped graded index can be created by placing dielectric shells with varying permittivity concentrically as in [38][43][44]. A stepped graded index can also be created by varying the density of a homogeneous dielectric as in [5][45][46][47]. This method is ideal for 3D printing as a single polymer can be used to create the gradient. Another method that is well suited for printing involves tapering density continuously with radius as in [48][49].

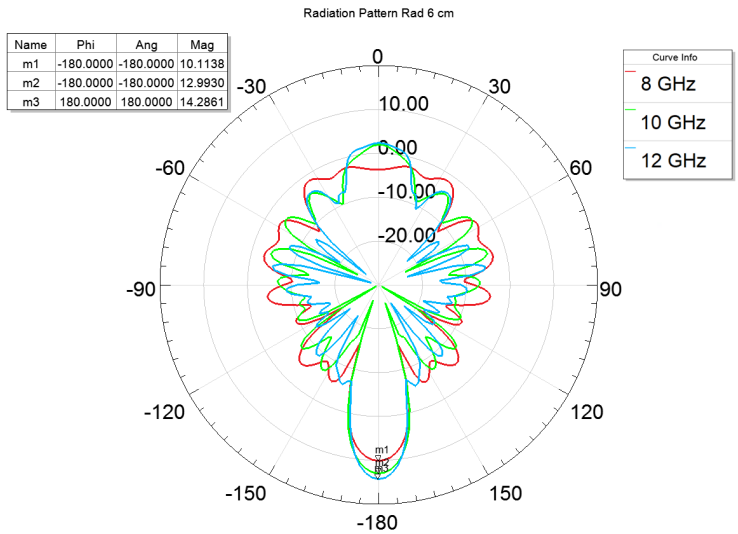

Figure 4.5: Simulated radiation pattern for Luneburg lens with 6 cm radius where markers M1-M3 show the peak gain at frequencies 8 - 12 GHz respecively

4.3.1 Modelling and simulation

To simulate the cells, an HFSS model was used with a Floquet analysis. Using a Floquet analysis allows the cells to be analysed as an infinite periodic sheet with boundary conditions causing the fields to be replicated from primary to secondary surfaces. A phase shift between the primary and secondary boundaries can be used to simulate an angle of incidence other than perpendicular but for this analysis it will be neglected as the method or parameter extraction presented later will consider a plane wave at broadside. The dimensions of the cell must be large enough for strong printing resolution but small enough to provide a smooth dielectric profile across the lens. In Figure 4.6a the density cell is shown in (a) while the HFSS model with a highlighted pair of primary and secondary Floquet boundaries is shown in (b).

4.3.2 Function fit for block permittivity

To determine the required block density as a function of radius, the S-parameters of the cells were simulated for a range of fill box widths. Since the S-parameters can characterise a

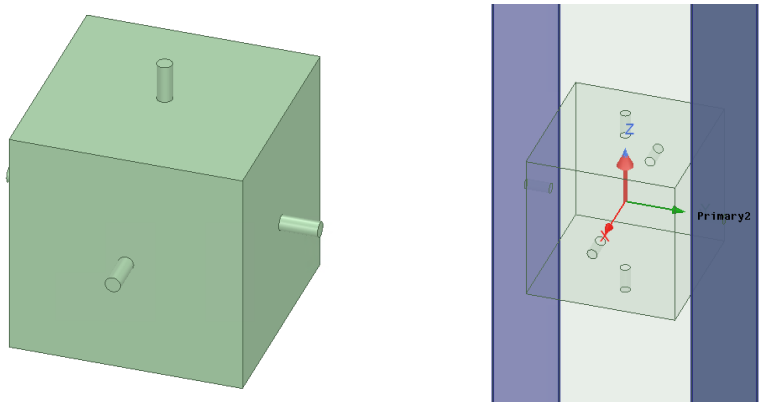

(a) Fill box with supports (b) Cell with Floquet ports

Figure 4.6: HFSS density cell model

two port device at a given frequency they can also be used to reverse engineer the material properties of a device assuming certain characteristics. In this case the equivalent permittivity of a slab dielectric can be determined using the process shown in [50]. While this process provides a useful estimate of the effective permittivity, it is derived for an incident broadside wave and lossless material. While After determining the effective refractive index and impedance of the cell the permittivity can be found as the ratio of refractive index to impedance:

$$\varepsilon = n/z \tag{4.2}$$

to characterise each unit cell as a function of fill box width. Determining the refractive index and impedance is a more involved process that is described in [50]. One of the core equations for the calculation of characteristic impedance is:

$$z = \pm\sqrt{\frac{(1+S_{11})^2 - S_{21}^2}{(1-S_{11})^2 - S_{21}^2}} \tag{4.3}$$

and the determination of refractive index can be defined as:

$$n = \frac{1}{k_0 d}\{[\Im[ln(exp(ink_0 d))] + 2m\pi] - i\Re[ln(exp(ink_0 d))]\} \tag{4.4}$$

where k_0 is the freespace wavenumber of the incident wave, d is the distance across the cell in the direction of wave propagation, and m is an integer referring to the branch index of the periodic solution for $\Re\{n\}$.

After extracting the permittivity, an experimental equation was determined to fit the data. After noting that the relationship between effective permittivity and fill box radius was logarithmic in nature, the following equation was used to fit the data:

$$W_{block}(\varepsilon_r) = A + B\log(C(\varepsilon_r + D)) \tag{4.5}$$

where the coefficients A - D are determined through curve fitting.

4.3.2.1 4 mm cells

To curve fit the 4 mm cells, Equation (4.5) was applied to the simulated data using the MATLAB curve fitting toolbox. The data and curve fit can be seen in Figure 4.7 while the

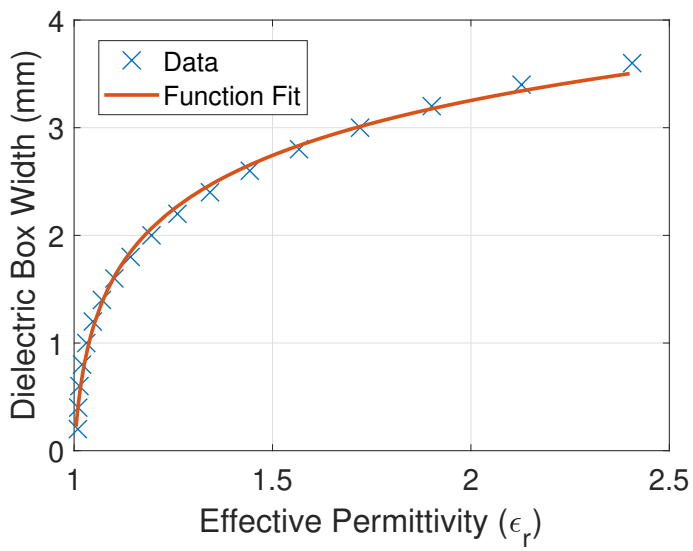

Figure 4.7: Dielectric fill box width as a function of effective permittivity for 4 mm cells at 10 GHz

function coefficients can be seen in Table 4.1. This function describes the relation between permittivity and dielectric box width yet to map the box width to a value for radius it must

be combined with the Luneburg lens permittivity equation described previously in Equation (4.1). Combining these equations gives the box width as a function of radius. This is the

Table 4.1: Function fit parameters for 4 mm cells

Parameter	Value
A	3.066
B	1.726
C	1.267
D	-0.9872

relation which can be used to build a CAD model for the lens by determining the fill box width for each cell. The design equation to give the box width for 4 mm cells making a lens with 4.5 cm radius is

$$W_{block}(r) = 3.066 + 1.726\log(1.267(1.0128 - \left(\frac{r}{45}\right)^2)) \tag{4.6}$$

where all dimensions are mm. This equation can then be used through scripting to build a printable file for the lens and can be seen plotted in Figure 4.8.

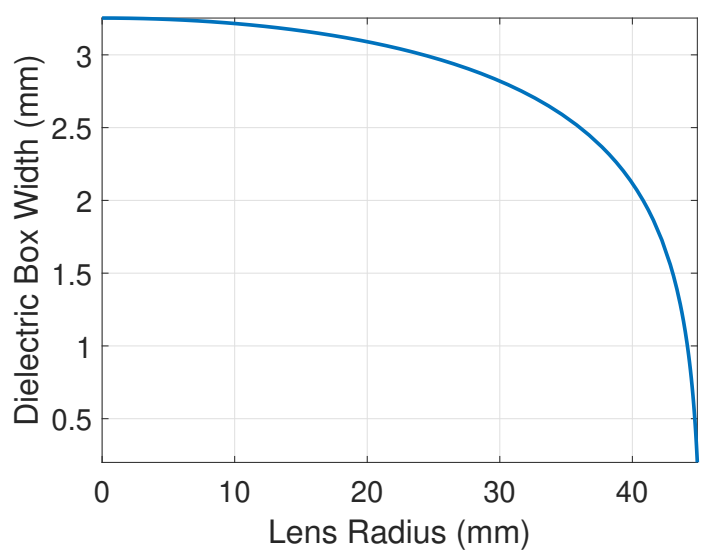

Figure 4.8: Dielectric fill box width as a function of lens radius for 4.5 cm radius with 4 mm cells at 10 GHz

4.3.2.2 2 mm cells

To curve fit the 2 mm cells, Equation (4.5) was applied to the simulated data using the MATLAB curve fitting toolbox. The data and curve fit can be seen in Figure 4.9 while

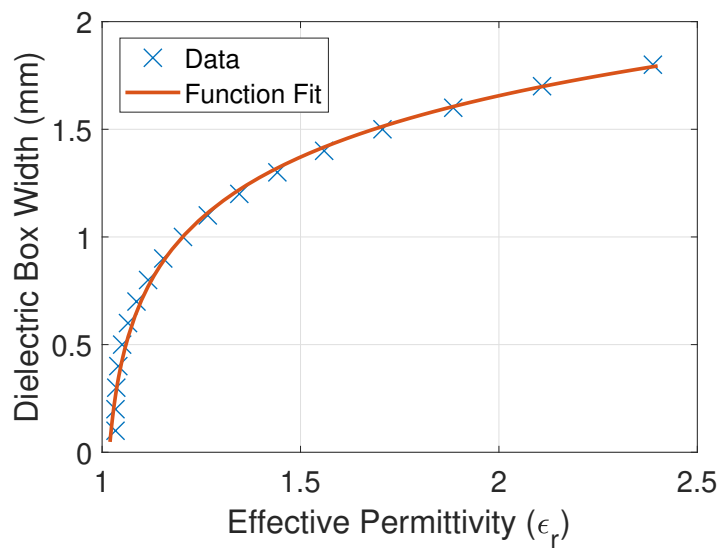

Figure 4.9: Dielectric fill box width as a function of effective permittivity for 2 mm cells at 10 GHz

the function coefficients can be seen in Table 4.2. This function describes the relationship between permittivity and dielectric box width; yet to map the box width to a value for radius it must be combined with the Luneburg lens permittivity equation described previously in Equation (4.1). Combining these equations gives the box width as a function of radius. This

Table 4.2: Function fit parameters for 2 mm cells

Parameter	Value
A	1.404
B	0.9463
C	1.846
D	-1

is the relation which can be used to build a CAD model for the lens by determining the fill box width for each cell. The design equation to give the box width for 2 mm cells making a

lens with 4.5 cm radius is

$$W_{block}(r) = 1.404 + 0.9463\log(1.846(1 - \left(\frac{r}{45}\right)^2)) \tag{4.7}$$

where all dimensions are mm. This equation can then be used through scripting to build a printable file for the lens and can be seen plotted in Figure 4.10.

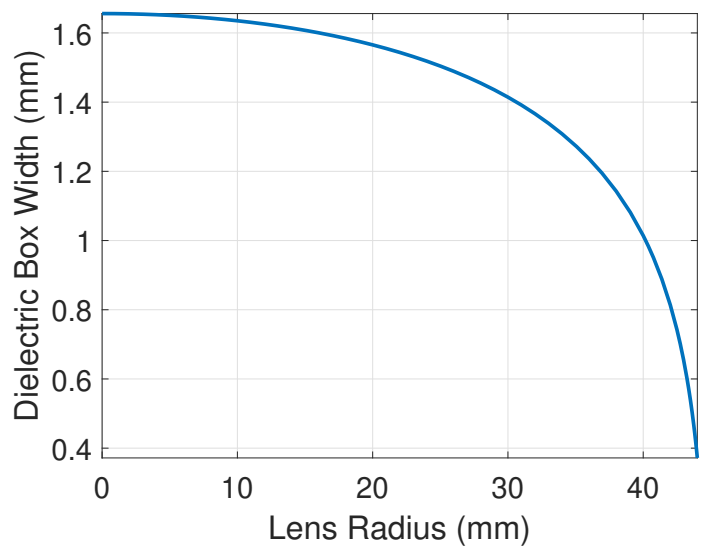

Figure 4.10: Dielectric fill box width as a function of lens radius for 4.5 cm radius with 2 mm cells at 10 GHz

The simulated equation for 2 mm cells can also be combined with the Luneburg lens equation using 6 cm as the radius to give

$$W_{block}(r) = 1.404 + 0.9463\log(1.846(1 - \left(\frac{r}{60}\right)^2)) \tag{4.8}$$

as the relationship between radius and cell fill box width. This equation can be seen plotted in Figure 4.11.

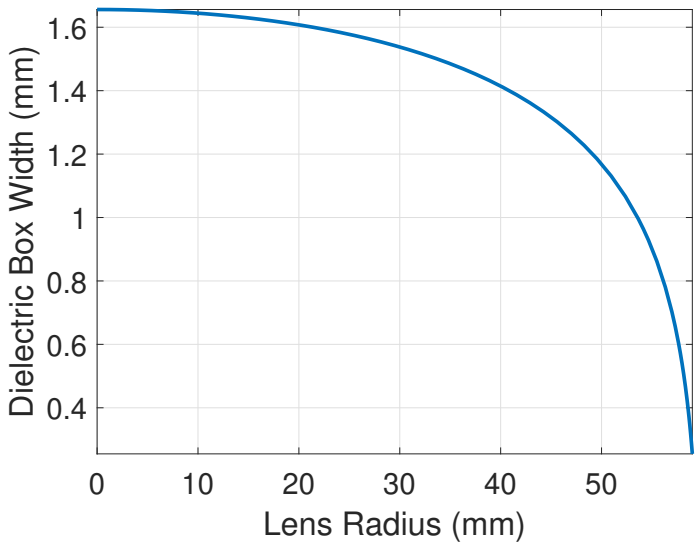

Figure 4.11: Dielectric fill box width as a function of lens radius for 6 cm radius with 2 mm cells at 10 GHz

4.3.3 CAD model generation

To build CAD models for printing a Python script was created and executed using the *"Run Script..."* command in HFSS. Generation of the file was initiated through the *"Record Script To File..."* command then altered to create the required geometry. An example of the Luneburg lens CAD model generated using the Python script can be seen in Figure 4.12. For the logistics of the printing process the model was broken into quarters to fit on the printer build plate.

4.3.4 Physical implementation

Printing of the lens antennas was performed by the Security and Disruptive Technologies group at the National Research Council Canada. Three different variants of the lens were printed, 2 and 4 mm cell width versions with a 4.5 cm radius, and a 2 mm cell width version with a 6 cm radius. All three lenses can be seen before plating with copper in Figure 4.13. Each of these lenses were printed in quarters and glued together to form the complete lens. The lens with 4 mm cells printed with excellent resolution and separation across the radius.

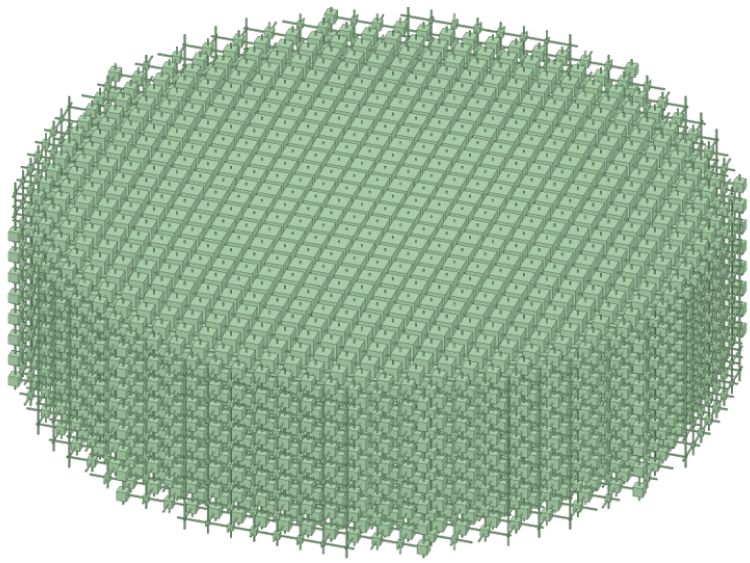

Figure 4.12: Luneburg lens CAD model generated through scripting in HFSS for printing

For the 2 mm cells some merging can be observed in the centre of the lens along with some structural issues towards the perimeter. All three lenses were plated with copper tape as seen in Figure 4.14.

4.3.5 Measurement and results

Far-field measurements were made using the anechoic chamber at Carleton University. Measurements were calibrated using an H-1498 standard gain horn antenna; the gain values for which were taken from [51]. The chamber was setup with a transmit horn antenna, operational range from 1 to 18 GHz, closest the door as seen in Figure 4.15. Calibration measurements were made at the three primary frequencies spanning x-band from start to middle to end (8, 10 and 12 GHz) by measuring the radiation pattern of the gain standard horn and comparing to the known gain plots. The difference between the measured and known gain can be used as a correction factor taking into account all the losses in the measurement setup. For the correction factor peak values were used both from the measured and known gain plots and the difference was used to determine the correction factor. Each correction factor can be seen in Table 4.3. These values can then be used to convert anechoic

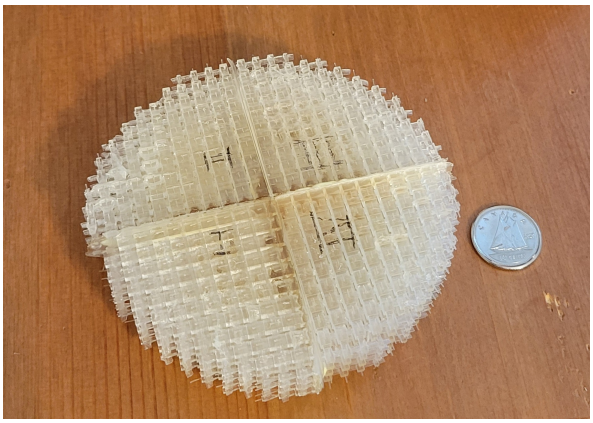

(a) 4 mm cell with 4.5 cm radius

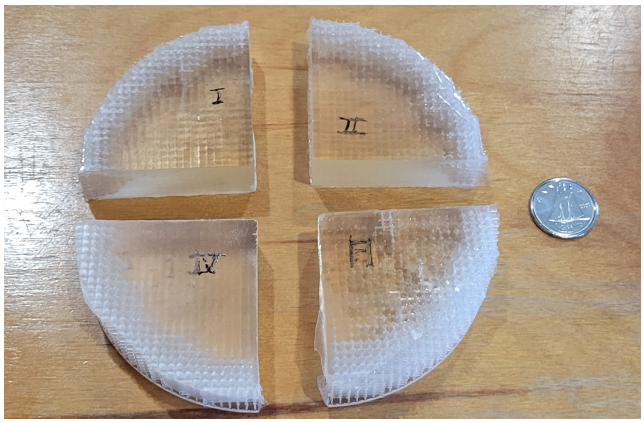

(b) 2 mm cell with 4.5 cm radius

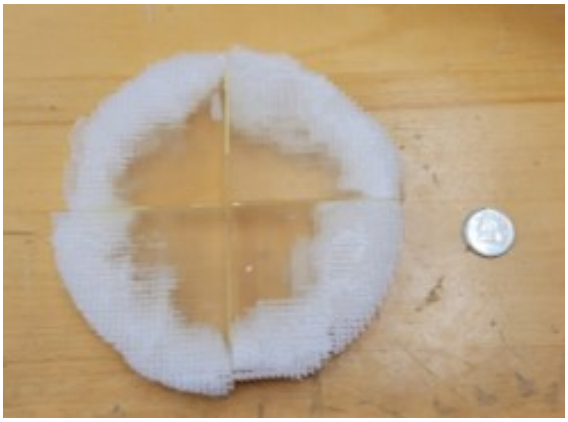

(c) 2 mm cell with 6 cm radius

Figure 4.13: Assembled Luneburg lens antennas before plating. The 2 mm cell versions of the lens are seen to experience some merging between adjacent fill boxes due to the resolution of the curing laser. Merging between the cells occurs for gaps less than 400 μm.

Figure 4.14: Assembled Luneburg lens antennas plated with copper tape

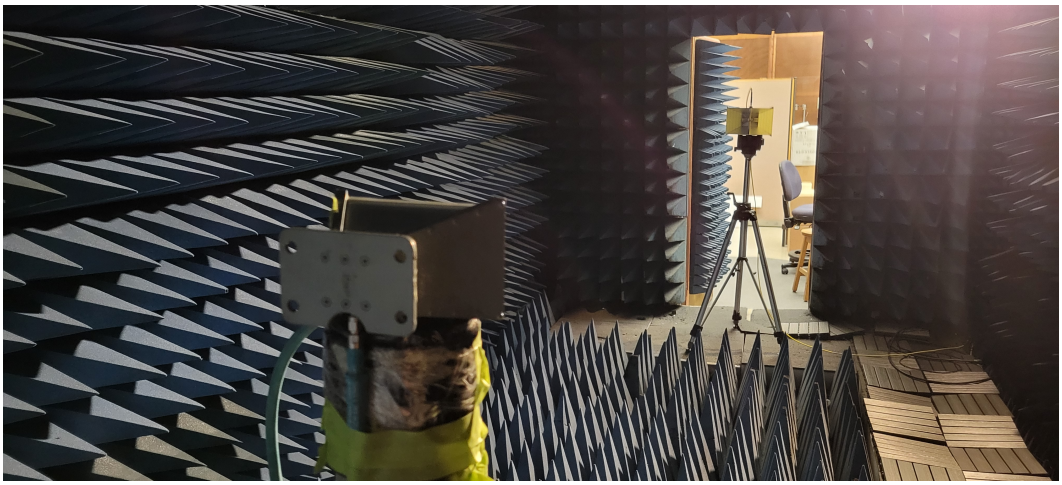

Figure 4.15: Anechoic chamber measurement setup for H-1498 gain standard horn

Table 4.3: Anechoic chamber gain correction factors

Frequency	Measured	Known	Correction Factor
8 GHz	-47.7 dB	11.0 dBi	58.7 dB
10 GHz	-50.8 dB	11.0 dBi	61.8 dB
12 GHz	-53.0 dB	11.5 dBi	64.5 dB

chamber measurements to antenna gain values in units of dBi. This process can also be done by measuring the loss of all cables and calculating the free-space path loss, but it is more efficient and reliable to calibrate the losses with a gain standard.

Another calibration measurement performed for the Luneburg lens antennas involved the inherent waveguide gain. Since the waveguide used to feed the Luneburg lens itself has gain measuring it separately allows the lens gain to be isolated. Replacing the gain standard horn with the waveguide as seen in Figure 4.16 allowed the radiation pattern to be measured.

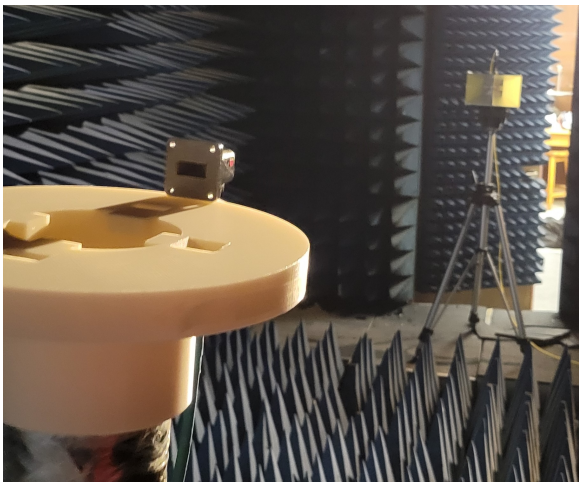

Figure 4.16: Anechoic chamber measurement setup for the waveguide feed

After calibrating the waveguide radiation pattern using the correction factors in Table 4.3 the gain values in dBi can be seen in Figure 4.17.

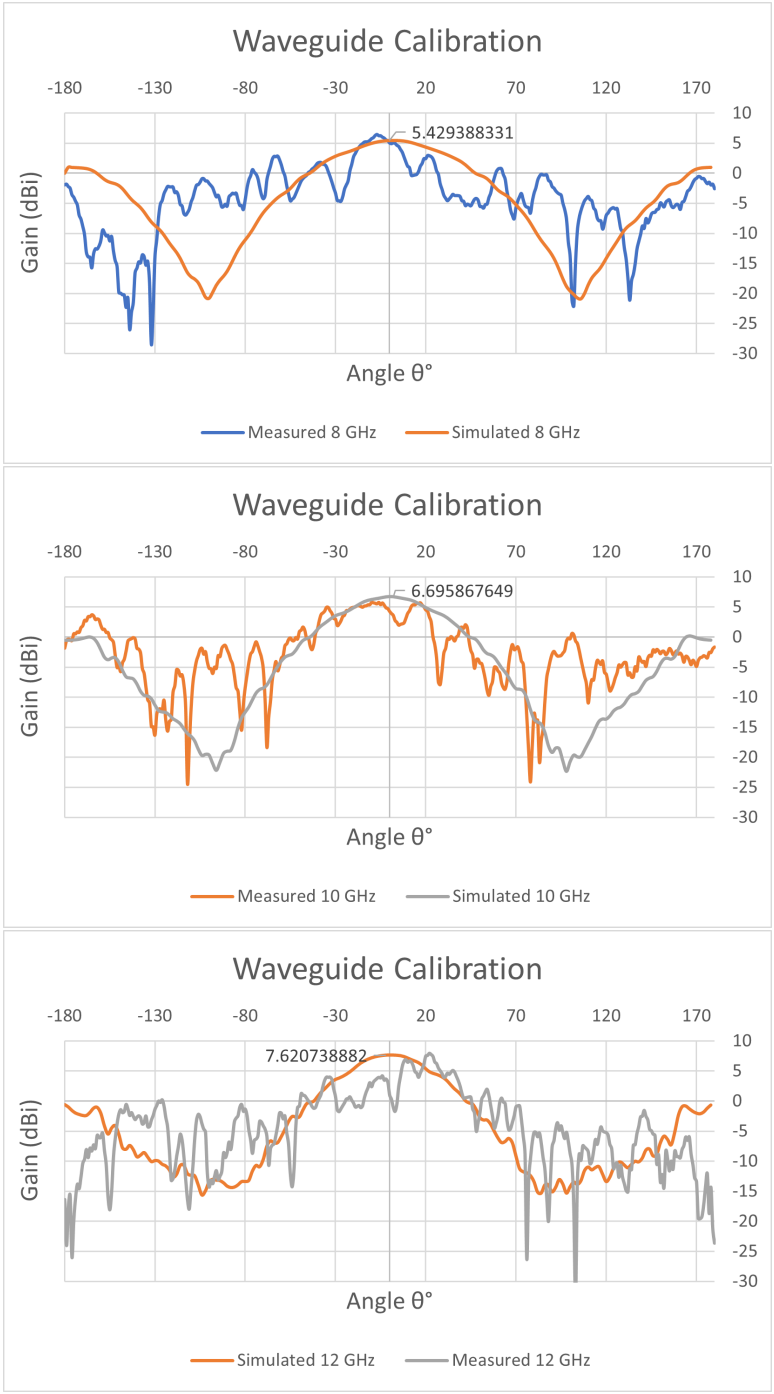

Figure 4.17: Far-field radiation pattern measurements for the waveguide connector compared with HFSS simulation

A main lobe of radiation can be seen at each frequency with a summary of the peak gain values in Table 4.4.

Table 4.4: Waveguide radiation peak gain summary

Frequency	Peak Gain
8 GHz	6.5 dBi
10 GHz	5.8 dBi
12 GHz	7.9 dBi

4.3.5.1 Lens with 4 mm cells and 4.5 cm radius

Three different frequency measurements at 8, 10 and 12 GHz were made for the 4 mm cell lens with 4.5 cm radius. To combine the lens with the waveguide feed, the former was placed on a cardboard shim to align the waveguide between the conductive plates of the lens as seen in Figure 4.18. Far-field measurements were captured for this setup and are compared

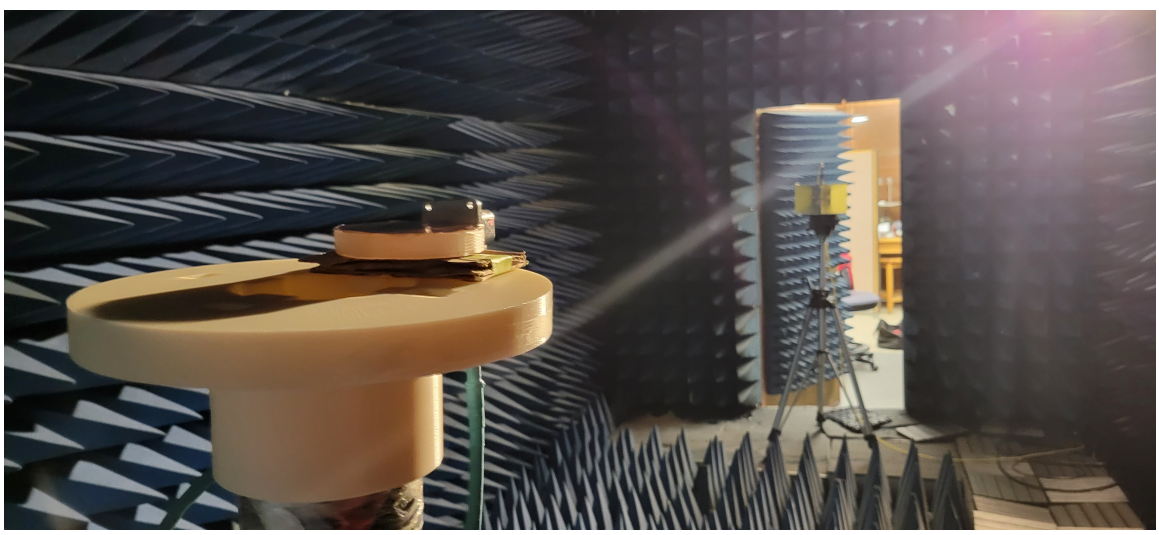

Figure 4.18: Anechoic chamber measurement setup for Luneburg lens antenna with 4.5 cm radius and 4 mm cells

with simulation, waveguide feed and 2 mm cell lens in Figure 4.20.

4.3.5.2 Lens with 2 mm cells and 4.5 cm radius

Three different frequency measurements at 8, 10 and 12 GHz were made for the 2 mm cell lens with 4.5 cm radius. To combine the lens with the waveguide feed the former was placed on a cardboard shim to align the waveguide between the conductive plates as was done for the 4 mm cell lens with 4.5 cm radius. This setup was used to measure the radiation pattern of the lens antenna and waveguide combined. A comparison of these measurements with simulation, waveguide feed and 4 mm cell lens can be seen in Figure 4.20 and a summary of the peak gain values are presented in Table 4.5. To better visualise comparisons between the

Table 4.5: Peak gain values in dBi for each of plotted measurements in Figure 4.20

Frequency	Lens 4 mm	Lens 2 mm	Lens Sim.	WG Meas.	WG Sim.
8 GHz	7.9	7.8	9.6	6.5	5.4
10 GHz	8.1	3.2	10.4	5.8	6.7
12 GHz	10.8	8.7	13.2	7.9	7.6

radiation patterns the data from Table 4.5 can be seen plotted in Figure 4.19. Across the

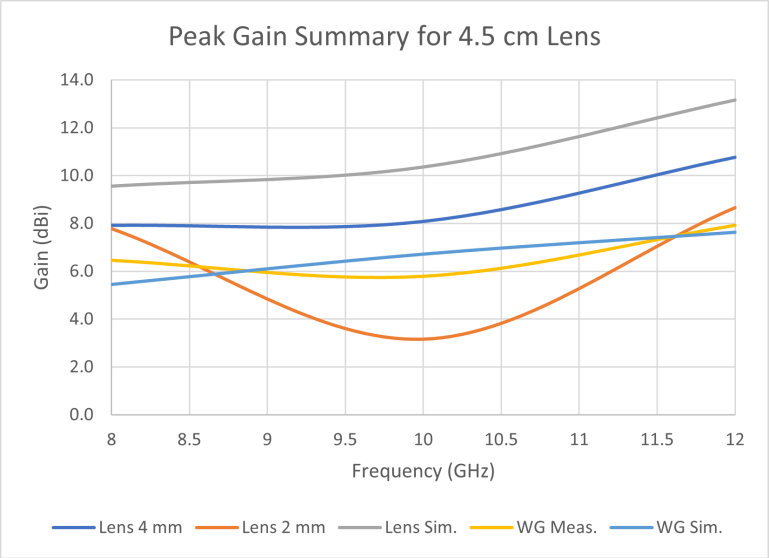

Figure 4.19: Peak gain plots to visualise the radiation pattern comparison with 4.5 cm radius lenses

three frequencies the Luneburg lens with 4 mm cells shows the best measured performance and consistently outperforms the waveguide baseline by roughly 2 dB. While this is less

than the gain increase of the simulated lens at roughly 4 dB, it is still demonstrates how 3D printing can be used to generate a lens capable of focusing RF radiation in the x-band.

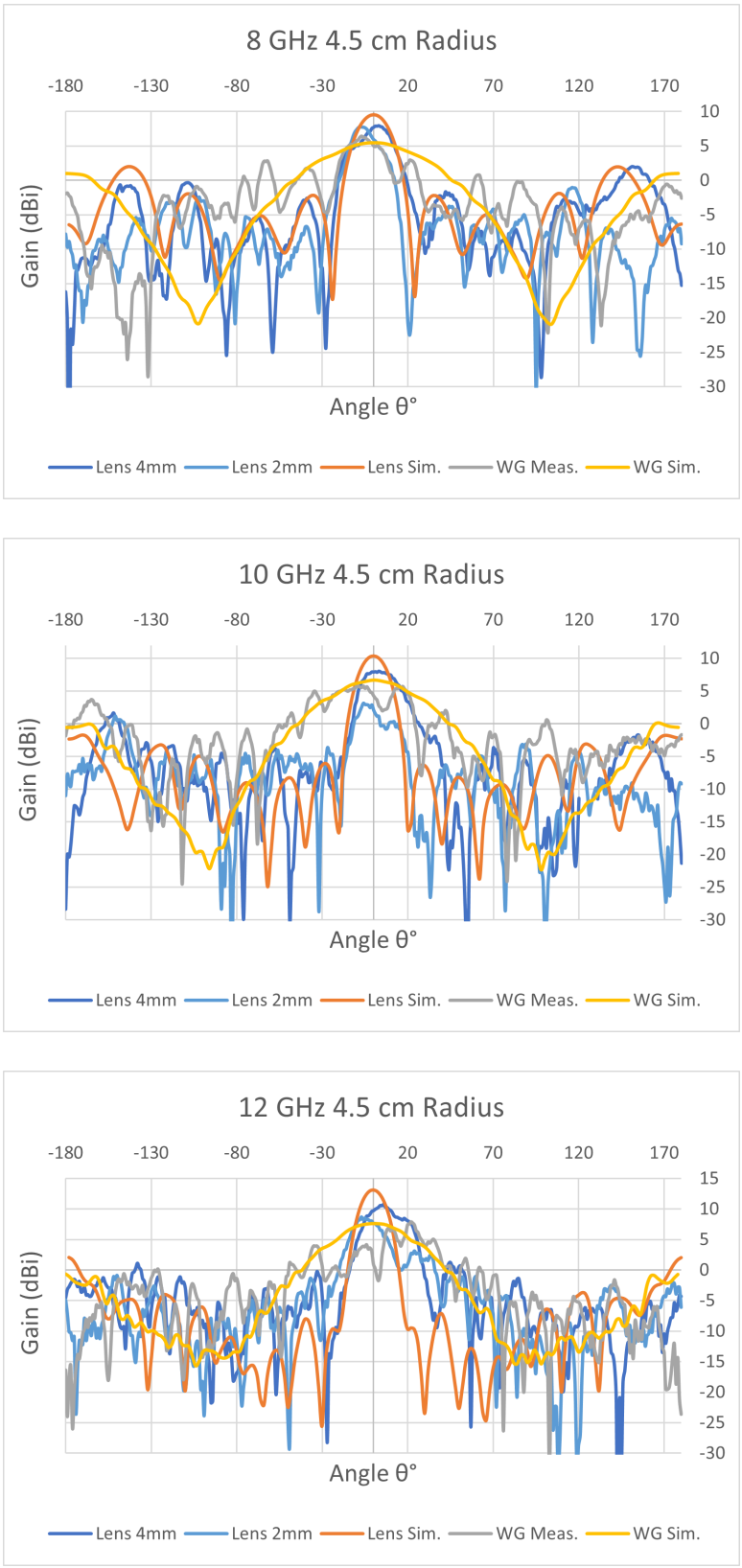

Figure 4.20: Comprehensive 4.5 cm radius Luneburg lens comparison with simulation and waveguide radiation

4.3.5.3 Lens with 2 mm cells and 6 cm radius

Three different frequency measurements at 8, 10 and 12 GHz were made for the 2 mm cell lens with 6 cm radius. To combine the lens with the waveguide feed the former was placed on a cardboard shim to align the waveguide between the conductive plates of the lens as seen in Figure 4.21. This setup was used to measure the radiation pattern of the lens antenna

Figure 4.21: Anechoic chamber measurement setup for Luneburg lens antenna with 6 cm radius and 2 mm cells

and waveguide combined. The results can be seen in Figure 4.23 compared with simulation and radiation from the waveguide and a summary of the peak gain values are presented in Table 4.5. To visualise the data a plot of the peak values for all compared radiation

Table 4.6: Peak gain values in dBi for each of plotted measurements in Figure 4.23

Frequency	Lens Meas.	Lens Sim.	WG Meas.	WG Sim.
8 GHz	3.1	10.1	6.5	5.4
10 GHz	4.0	13.0	5.8	6.7
12 GHz	8.5	14.3	7.9	7.6

patterns can be seen in Figure 4.22. From the plots it can be seen that the performance of the lens is worse than simulated by roughly 7 dB and displays very similar peak gain as the waveguide radiation pattern. This indicates that the lens is redundant and is not impacting

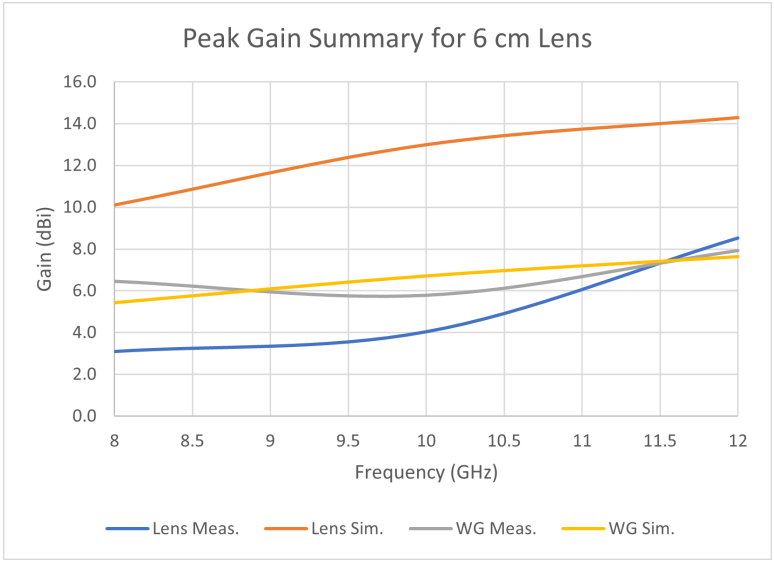

Figure 4.22: Peak gain plots to visualise the radiation pattern comparison with 6 cm radius lenses

the radiation. Since the increased radius should improve performance based on the theory, the issue must be with the construction of the lens. A future comparison should be done with a 6 cm radius lens using 4 mm cells for better resolution.

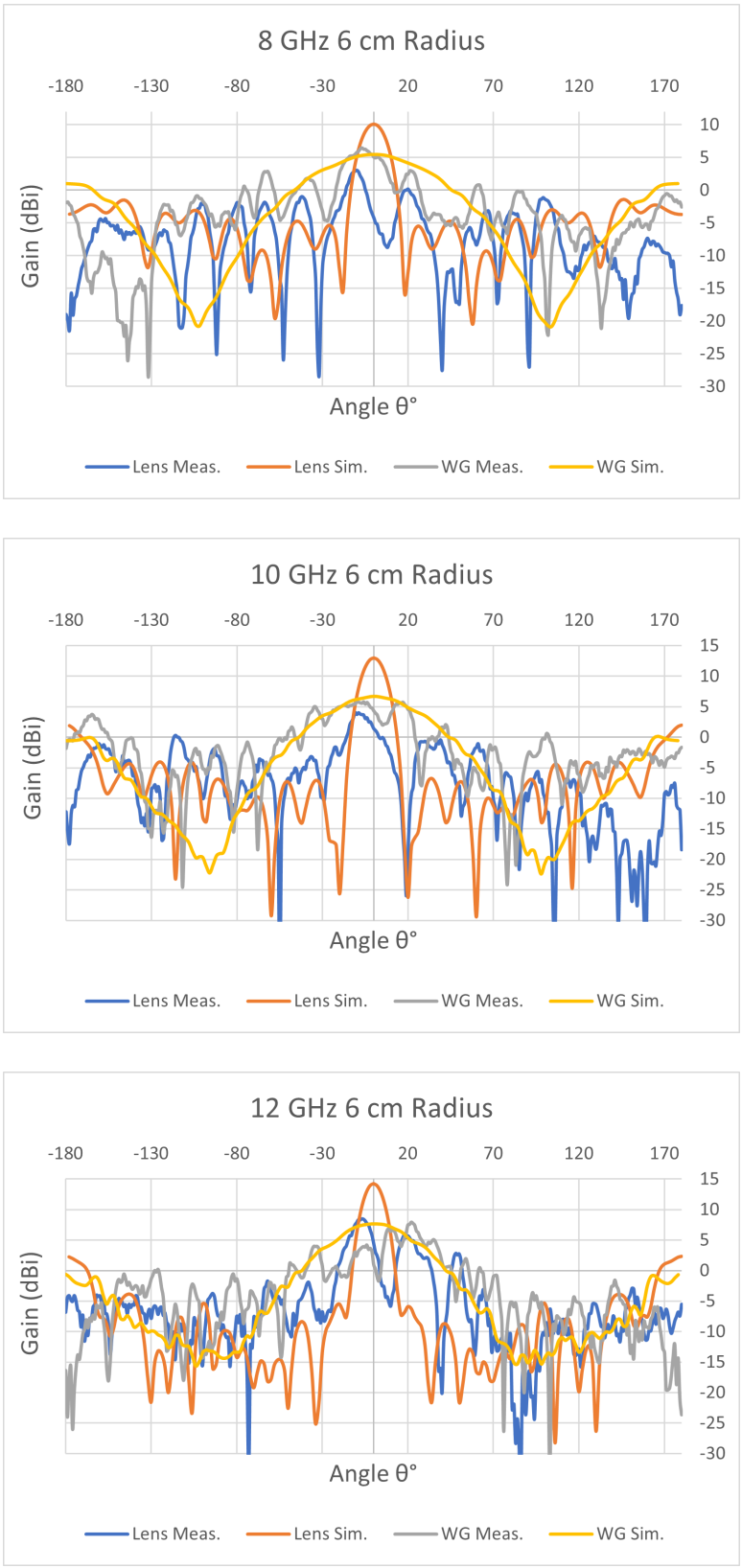

Figure 4.23: Comprehensive 6 cm radius Luneburg lens comparison with simulation and waveguide radiation

Chapter 5

Butler Matrix Design for Beam Steering

The Butler matrix is a passive beamforming device capable of providing a unique phase progression across its array ports for each input (beam) port [52][53][54][55]. This allows an antenna array to form a main lobe of radiation with orientation dependant on the beam port. A general block diagram layout of the Butler matrix can be seen in Figure 5.1. The Butler matrix design process is further broken up into sub-components: phase shifters, crossovers, and hybrid couplers. These devices work together to accept a signal applied to one of the four beam ports and distribute it evenly across the array ports with a unique phase progression corresponding to a given beam port. Each of the beam ports creates a unique phase progression $\Delta\theta$ (See Table 5.1) which determines the orientation of the main radiation lobe generated by the antenna array. Table 5.1 shows the relationships between the phases at the input and output ports of the Butler matrix. These phases progressions result in the specified beam direction for the main radiation lobe.

For this investigation two methods of creating a Butler matrix for passive beamforming will be investigated. The first method involves the use of transmission lines which are commonly used for this type of design [52][53][54]. Transmission lines are an excellent de-

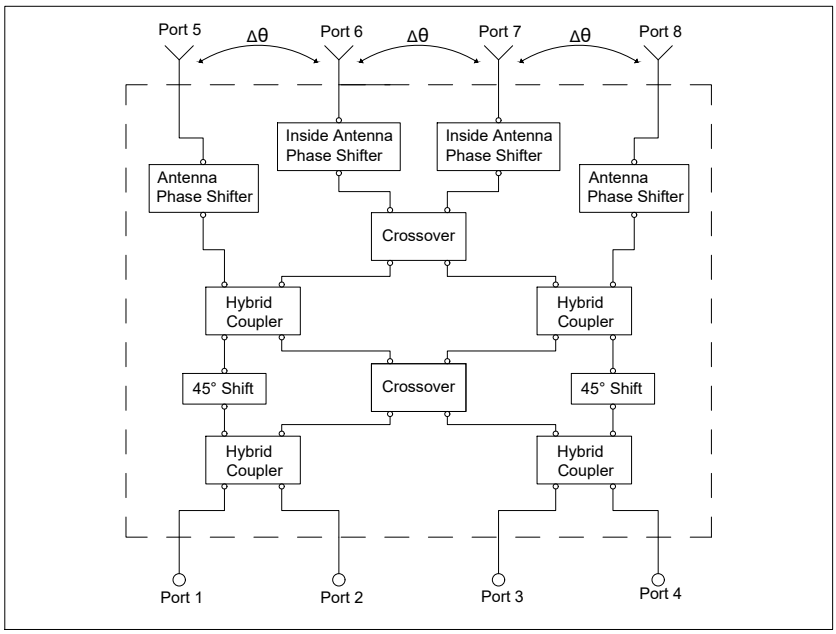

Figure 5.1: Layout of the Butler matrix design. Ports 5 - 8 present their signals to the associated patch antenna in the array. [56]

sign choice as they can provide low loss on high quality substrates and produce a design proportional in size to an antenna array both being dependant on wavelength. A second method which is often less utilised involves the use of lumped passive elements [57][58]. An advantage of lumped components is that their size is less coupled to wave length allowing for a more compact matrix design at low frequencies. Two disadvantages of the lumped design however are that components are often lossy compared to transmission lines and have a self resonant frequency that can impede high frequency designs.

5.1 Transmission line matrix

In this section a transmission line Butler matrix and patch antenna array will be designed using ADS for Rogers RO3006 substrate at a centre frequency of 2.4 GHz. Fabrication of the matrix was done using a Cricut knife tracing tool, a drill press and soldering iron.

Design of the components was completed individually for a 50Ω system. For a transmis-

Table 5.1: Relative phases and beam directions across the Butler matrix. [56]

Array \ Beam	Port 1	Port 2	Port 3	Port 4
Port 5	135°	45°	90°	0°
Port 6	90°	180°	-45°	45°
Port 7	45°	-45°	180°	90°
Port 8	0°	90°	45°	135°
Phase $\Delta\theta$	-45°	135°	-135°	45°
Beam Direction	1R (15°)	2L (-45°)	2R (45°)	1L (-15°)

sion line Butler matrix the two main design parameters are electrical length and impedance for each line. In the case of the phase shifters and crossover the desired characteristic impedance is 50Ω making phase the only design variable. However the hybrid couple requires a combination of impedance transforms to evenly split power at the output ports with the desired phase. In order to calculate electrical length the wavelength of the signal at the desired frequency must be known. This can be calculated as $\lambda_0 = c/f$ where λ_0 is the wavelength of the signal in free-space, c is the speed of wave and f is the frequency of operation. This wavelength can be mapped to the medium of propagation as the effective wavelength described as $\lambda_{eff} = \lambda_0/\sqrt{\varepsilon_{eff}}$ where the effective permittivity (ε_{eff}) for a microstrip transmission line is described by Equation (3.2). Knowing the effective permittivity for a microstrip transmission line allows the characteristic impedance to be calculated as [35]

$$Z_0 = \begin{cases} \frac{60}{\sqrt{\varepsilon_{eff}}} \ln\left(\frac{8d}{W} + \frac{W}{4d}\right) & \text{for } W/d \leq 1 \\ \frac{120\pi}{\sqrt{\varepsilon_{eff}}[W/d + 1.393 + 0.667\ln(W/d + 1.444)]} & \text{for } W/d \geq 1 \end{cases} \tag{5.1}$$

Using Equations (3.2) and (5.1) initial values can be determined that ignore coupling between sections and parasitic loading at transitions. To more accurately capture the physical properties of each component, an EM simulator can be used to generate a numerical model. Numerical models are a useful design tool that can capture many effects which are imprac-

tical to describe analytically. For the matrix design presented here initial values will be calculated and simulated using a schematic model before translating to an EM model for final tuning. A combined EM model of the assembled matrix will then be simulated before adding a patch antenna array.

5.1.1 Hybrid coupler design

The hybrid coupler is a common RF component that is characterised by an even splitting of power between two output ports with 90° phase shift between them. A common hybrid coupler topology uses microstrip transmission lines to create the desired splitting and phase shift [35]. This method is practical at high frequencies when the required line lengths are small and many lumped components are close to self-resonance. The required transmission line parameters of a hybrid coupler are shown in Figure 5.2.

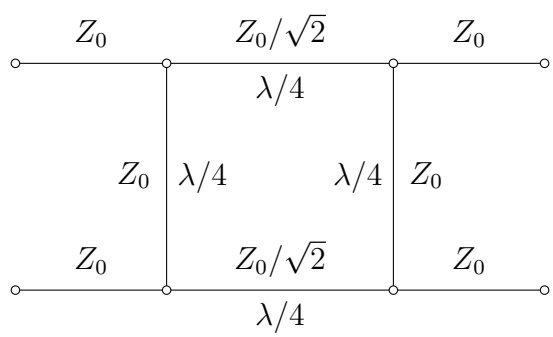

Figure 5.2: Branch-line hybrid coupler [35]

5.1.2 Simulation

To design the coupler a model was made in Keysight ADS using schematic microstrip components as shown in Figure 5.3. The microstrip dimensions were calculated using the design equations presented at the beginning of this section.

While microstrip equations can be used to calculate the properties of an isolated section of line, adjustments must be made after incorporating into a circuit. Most notably the loading

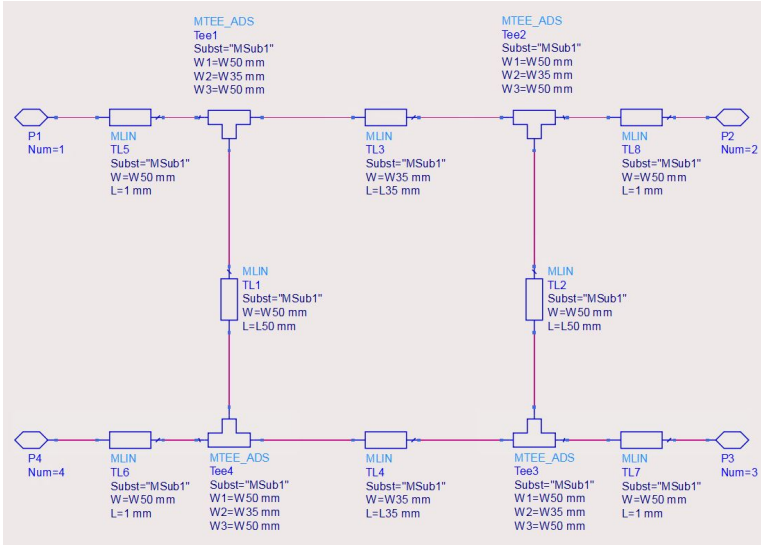

Figure 5.3: Schematic model and testbench for the transmission line hybrid coupler

effect of the shunt capacitance introduced by the T-section of transmission line. This loading capacitance has a tendency to add an additional phase shift that can increase the effective length of the transmission line. To counteract this effect the lengths of each transmission line were shortened through tuning until achieving the appropriate matching and phase shift at 2.4 GHz. This tuning process makes use of the ADS models for each transmission line section but does not account for the interaction between sections. These interactions can be captured by an EM model as shown in Figure 5.4. After tuning the transmission line lengths

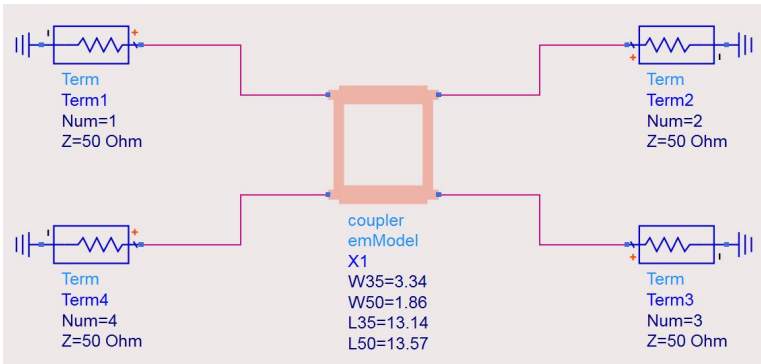

Figure 5.4: EM model and testbench for the transmission line hybrid coupler

of the EM model the final lengths can be seen shown alongside the the initial LineCalc values in Table 5.2. The line widths were kept constant trough the tuning process as the design

equations for characteristic impedance are generally robust, while the line lengths were tuned to account for the miniaturization effects of capacitive loading. The final simulated phase

Table 5.2: Hybrid coupler initial and final transmission line dimensions

Parameter	Initial	Final
W50	1.86 mm	1.86 mm
L50	14.77 mm	13.57 mm
W35	3.34 mm	3.34 mm
L35	14.33 mm	13.14 mm

difference at the output, transmission, isolation and input reflection parameters can be seen in Figure 5.5.

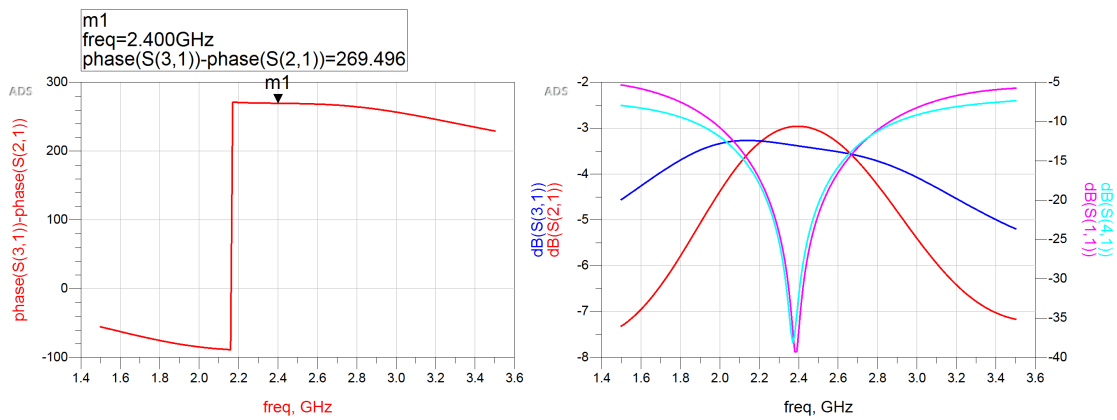

Figure 5.5: Simulated output phase difference (left) and transmission/reflection/isolation magnitude (right)

5.1.3 Crossover design

A simple approach was taken for the crossover design with one section of transmission line connecting to the bottom layer through a set of vias and crossing under the other section of transmission line. The initial design can be seen below in Figure 5.6. This design uses two direct paths between ports to reduce the overall size of the matrix. Other designs have been produced using back to back couplers to produce the crossover effect without the need to via through to the bottom layer [53]. The port to port connection through the vias was tuned

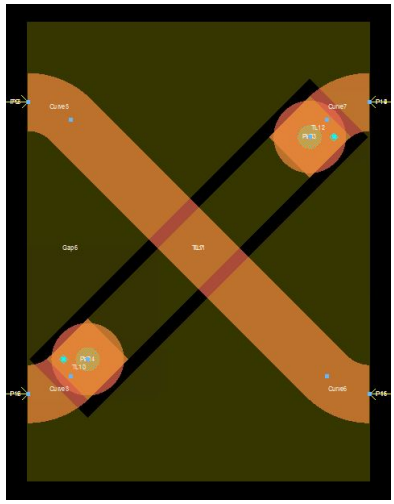

Figure 5.6: EM model for the initial transmission line crossover

for an insertion loss of less than one dB, yet the throughput on the single layer connection struggled. While the connection through the vias transitioned from a microtrip line to a coplanar microstrip on the lower layer, the top conductor encountered a discontinuity in the ground plane while crossing over the lower conductor. To counteract this discontinuity two ground strips were added beside the top conductor to form a coplanar microstrip making the discontinuity less disruptive. The added ground strips can be seen added to the model in Figure 5.4. With the added continuity of the coplanar ground strips the insertion loss for

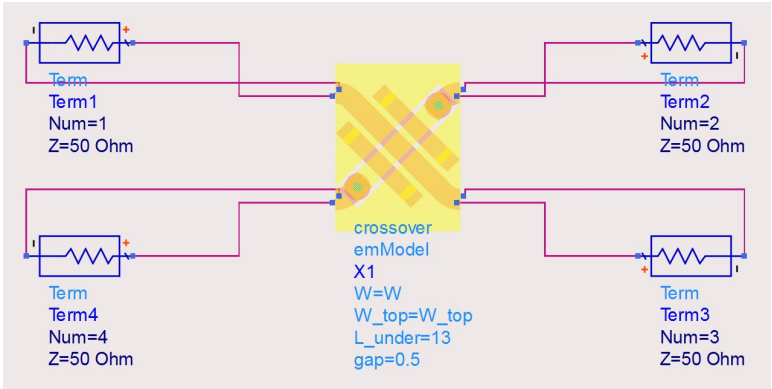

Figure 5.7: EM model and testbench for the transmission line crossover

both paths were brought below one dB as seen in Figure 5.8.

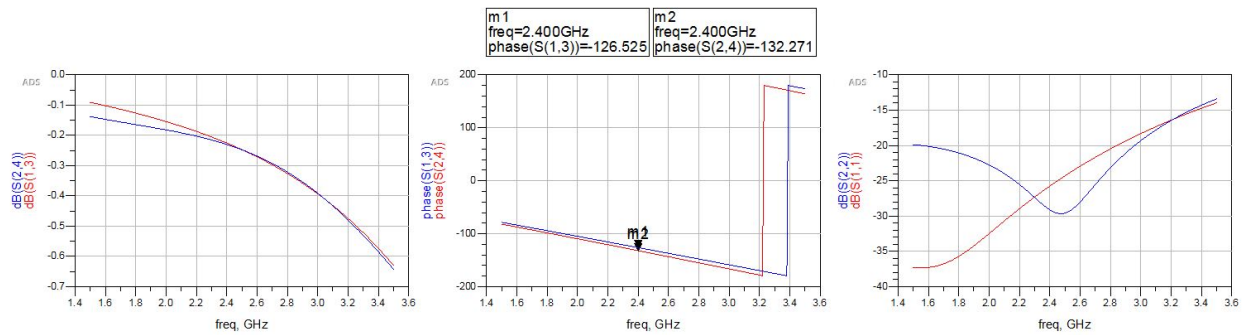

Figure 5.8: Simulated transmission magnitude (left) transmission phase (centre) and reflection magnitude (right)

5.1.4 Phase shifter design

For the proper phase progression of the Butler matrix it is required that the phase shifter provide a 45 degree phase shift relative to the phase shift of the crossover. Looking at the phase shift for the crossover in Figure 5.8 it can be seen to be 126 degrees and 132 degrees for the top plane and through via paths respectively. A phase shift across the shifter of approximately $mean(126,\ 132) + 45 = 174$ degrees is required. A simple meandered section of transmission line was used to provide the phase shift (see figure 5.9) with the length of the meander tuned to achieve the required phase shift value.

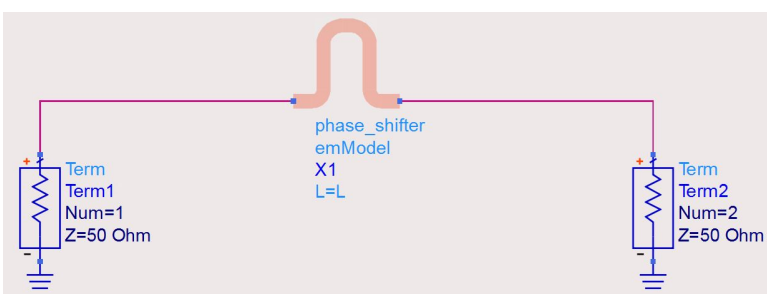

Figure 5.9: EM model and testbench for the transmission line phase shifter

5.1.5 Patch antenna design

As a microstrip antenna the patch is an ideal array element to use with a Butler matrix. Without disruption of continuity each patch can be connected to its appropriate array port

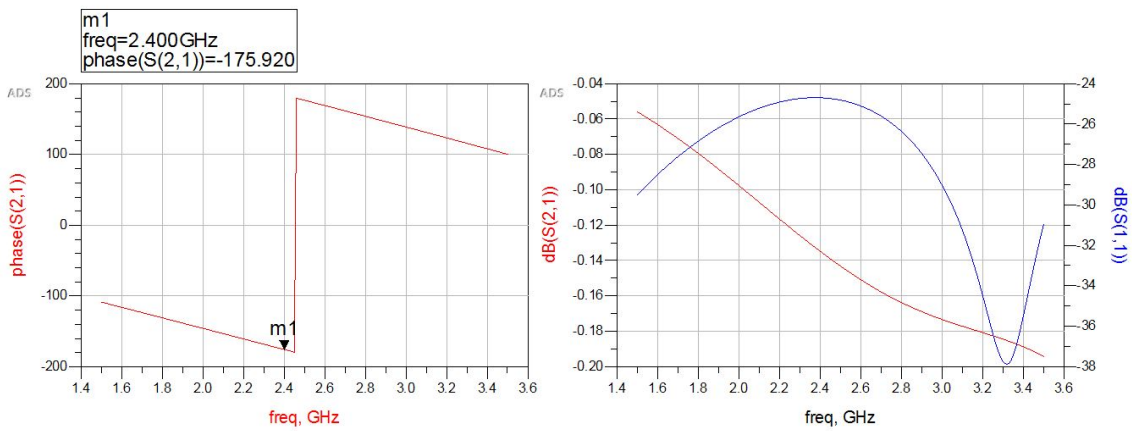

Figure 5.10: Simulated phase shift (left) and transmission/reflection magnitude (right)

with a transmission line matched to the characteristic impedance of the design, in this case 50Ω. A patch antenna radiates through the constructive interference of fringing fields separated by half a wavelength [4]. To accomplish this the length of the patch should be half a wavelength at the desired frequency of operation. Since the incident wave is travelling along the surface of the antenna it will be impacted by the dielectric substrate below the patch. To account for this the effective permittivity of the substrate must be calculated given the relative permittivity of the substrate and antenna dimensions [59]. The effective permittivity can be found using equation (3.2). The width of the patch is a less critical design parameter relative to the length and can take on a range of values impacting the impedance and bandwidth of the antenna [4]. For this design the antenna width was determined as [60]

$$W = \frac{c}{2f_0\sqrt{\frac{\varepsilon_r+1}{2}}} \tag{5.2}$$

where c is the speed of light in a vacuum and f_0 is the centre frequency of the design. With the width and effective permittivity of the patch antenna determined its length was found as [60]

$$L = \frac{c}{2f_0\sqrt{\varepsilon_{eff}}} - 0.824h\left(\frac{(\varepsilon_{eff}+0.3)(\frac{W}{h}+0.264)}{(\varepsilon_{eff}-0.258)(\frac{W}{h}+0.8)}\right) \tag{5.3}$$

where the second term is an experimental fill factor to centre the resonant frequency. Using this method to design a patch antenna at 2.4 GHz on Rogers RO3006 substrate with relative permittivity 6.15 and thickness 1.27 mm the length and width of the antenna were calculated to be 25 and 33 mm respectively.

Since a patch antenna is an open circuit at the edge except for parasitic capacitance it will have the largest magnitude of electric field at this location. Using a transmission line model for the patch the impedance should be seen to reduce moving away from the edge as described by [35]

$$Z_{in} = Z_0 \frac{Z_L + jZ_0 \tan\beta\ell}{Z_0 + jZ_L \tan\beta\ell} \tag{5.4}$$

where Z_0 is the characteristic impedance, Z_L is the load impedance, β is the phase constant and ℓ is the length along the transmission line. This equation is derived using a single value for voltage across the entire width of a transmission line. Since a patch antenna is typically much larger than the transmission line feeding it this assumption will not necessarily hold true yet it sill gives a good indication that the impedance of the antenna should be lower towards the centre.

To match the input impedance of the antenna to 50Ω an inset was added and experimentally swept to find the optimal match. An EM model of the patch was build in ADS and swept as seen in Figure 5.11. After sweeping the inset length a value of 9 mm was found

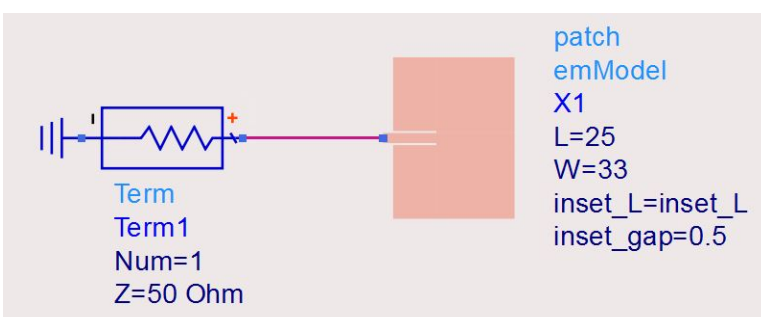

Figure 5.11: Patch antenna EM model and testbench

to be optimal. The input reflection coefficient with these parameters can be seen in Figure 5.12.

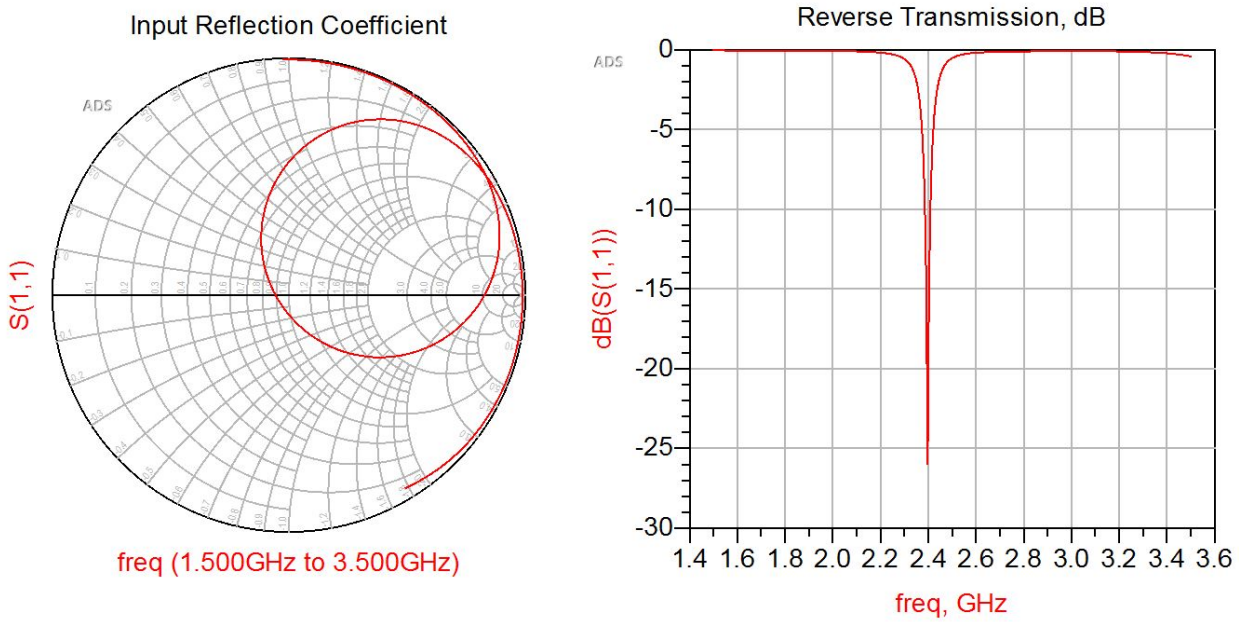

Figure 5.12: Simulated patch antenna input refection

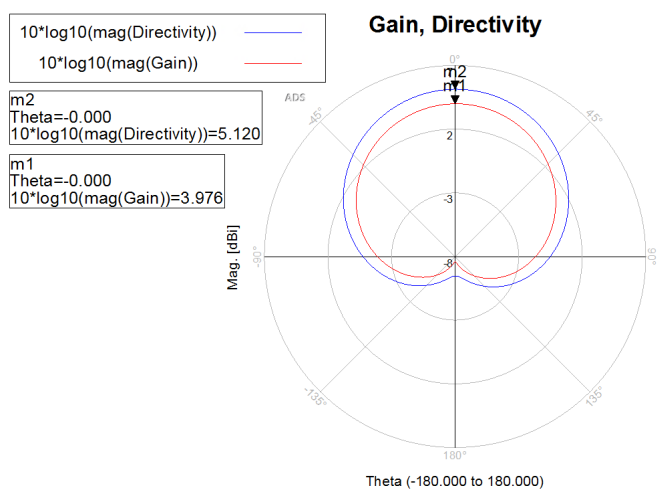

Figure 5.13: Simulated patch antenna radiation pattern

5.1.6 Matrix phase and amplitude performance

Assembling the matrix as an EM model allows the phase and amplitude between the beam array ports to be verified before connecting the antenna array. An ideal matrix would split power evenly across the four array ports for a transmission magnitude of -6 dB. Between the array ports the phase progression should be constant and consistent with Table 5.1. The

matrix EM model can be seen placed in a testbench in Figure 5.14. The input impedance

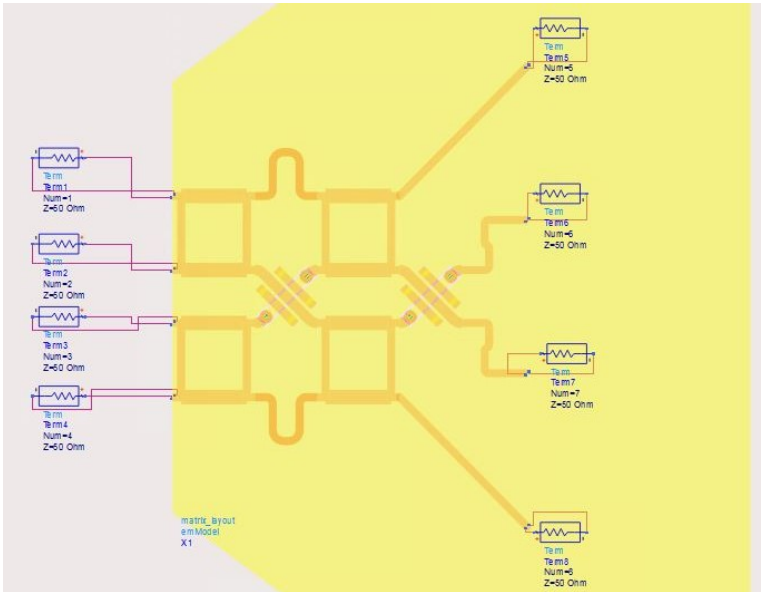

Figure 5.14: EM model and testbench for the assembled transmission line matrix without array

match for each port can be seen in Figure 5.15. Array ports 6 and 7 are the best matched at 2.4 GHz but all ports are below -20 dB return loss at the centre frequency. This match can be considered almost ideal with less than 1% of power being reflected from each port. For the transmission magnitudes Figure 5.16 shows a range of roughly 2.5 dB from -5.25

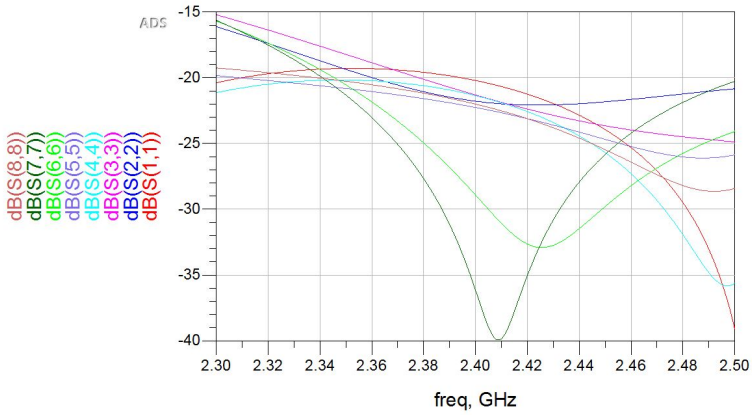

Figure 5.15: Simulated input reflection for the transmission line matrix

dB to -7.75 dB. The highest transmission occurs between ports 1 to 5 and 4 to 8 as these have the shortest paths and do not have to traverse either crossover. The least transmission

occurs between ports 4 to 6 where the signal crosses two hybrid couplers, adjacently then diagonally, a phase shifter and one crossover through the via section. Phase progressions

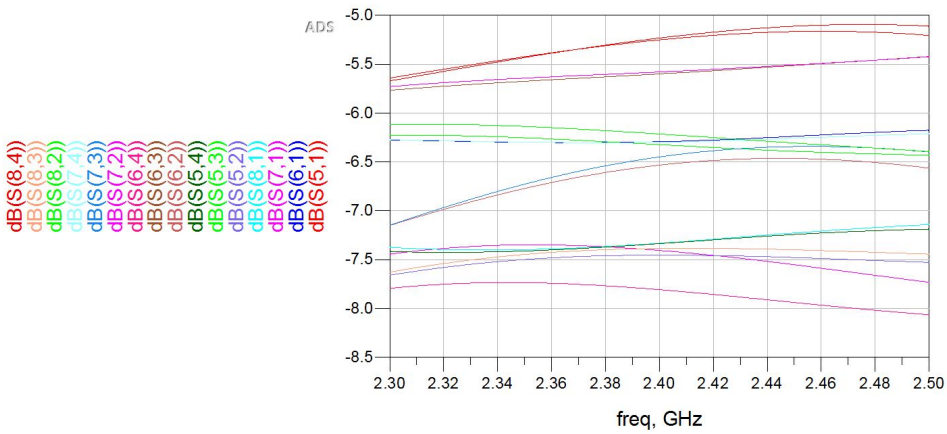

Figure 5.16: Simulated transmission magnitude for the transmission line matrix

across the matrix are dependant on the input port as shown in Table 5.1. On the left-hand plot in Figure 5.17 the phase progression from port 1 can be seen clustered about 45° while the phase progression from port 2 can be seen clustered around -135°. On the right-hand side the phase progressions from ports 3 and 4 can be seen clustered about 135° and -45° respectively. With an even distribution of power across array ports and consistent

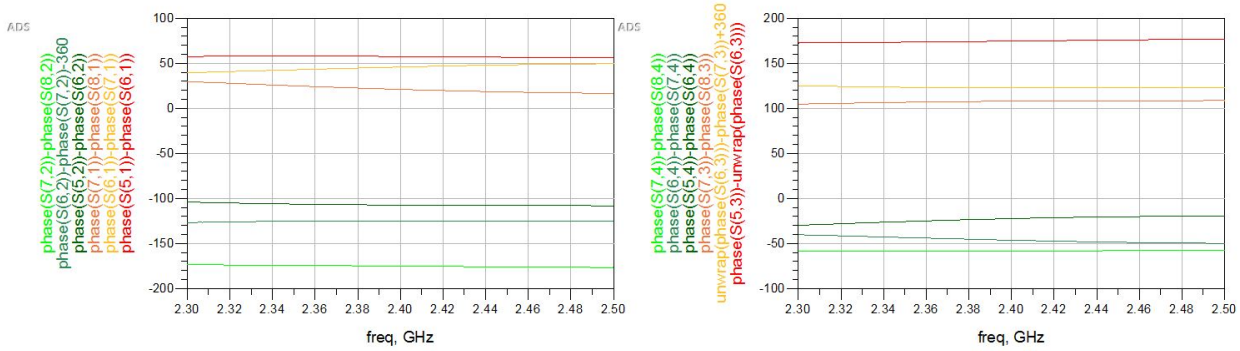

Figure 5.17: Simulated phase progression for the transmission line matrix

phase progressions the matrix can be expected to produce clearly defined radiation lobes in conjunction with an antenna array.

5.1.7 Beamforming capability

To simulate the Butler matrix and patch antenna array a finite element method (FEM) simulation was used with a convergence criteria of Delta error = 0.02. The simulated results were plotted in the far-field with cross sectional cuts taken across theta to display the beamforming of the antenna array. In Figure 5.18 the beamforming for each beam port is presented with ports 1 and 4 producing beams at -15° and 15° as indicted in Table 5.1. Ports 2 and 3 produce radiation lobes at obtuse angles as theoretically predicted except they occur at ± 60° rather than ± 45°. This could be due to the comparatively large phase progression spread from ports 2 and 3 relative to ports 1 and 4.

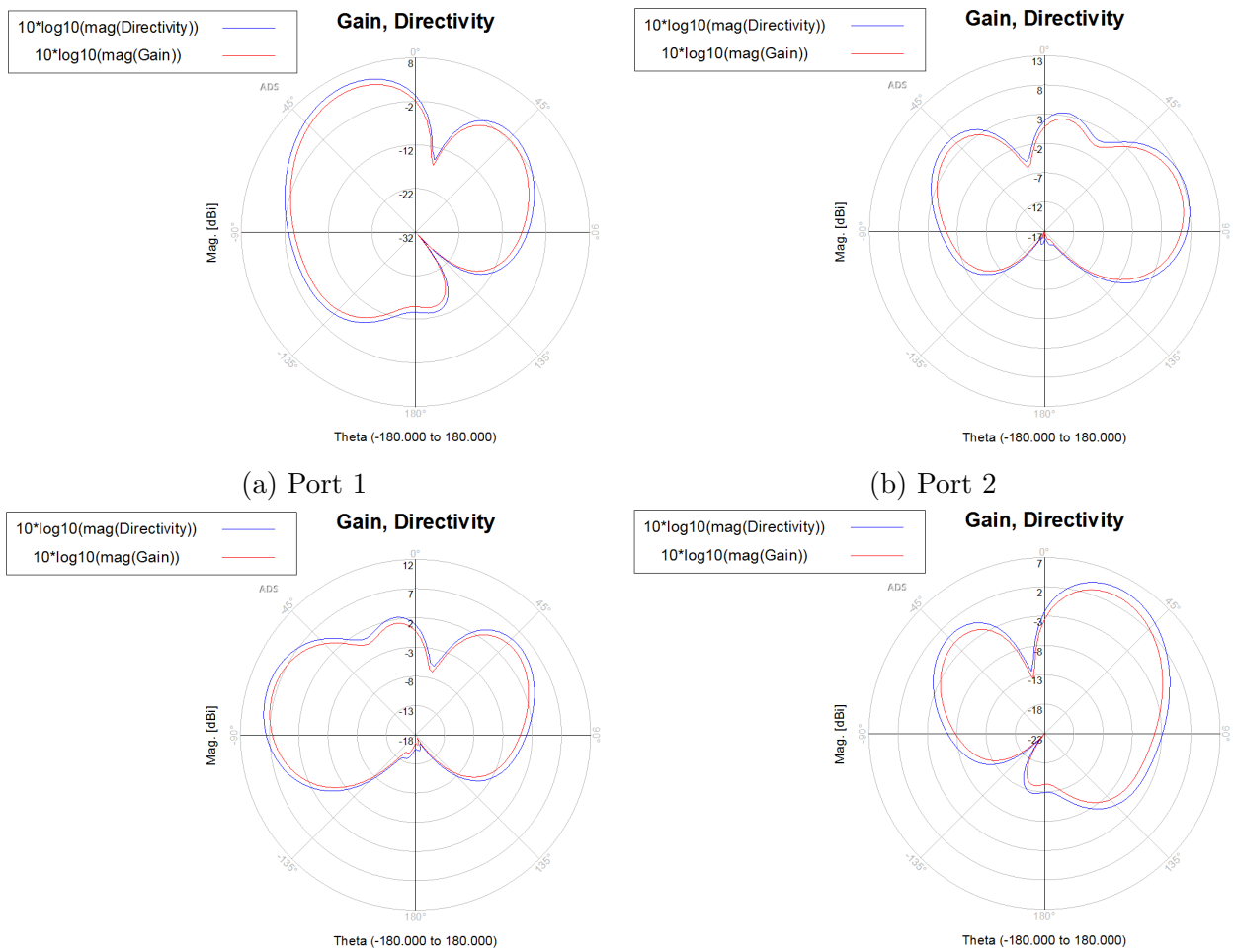

(a) Port 1

(b) Port 2

(c) Port 3

(d) Port 4

Figure 5.18: Fabricated and populated lumped Butler matrix

5.2 Fabrication and measurement

Fabrication of the matrix was performed with a Cricut cutter and board of Rogers RO3006 substrate [61]. With the Cricut cutting the outline in the cladding for the top conductor the via holes were made with a drill press for the crossover and to ground the sides of each SMA connector (Figure 5.19). After tracing the outline in the top conductor and drilling the vias

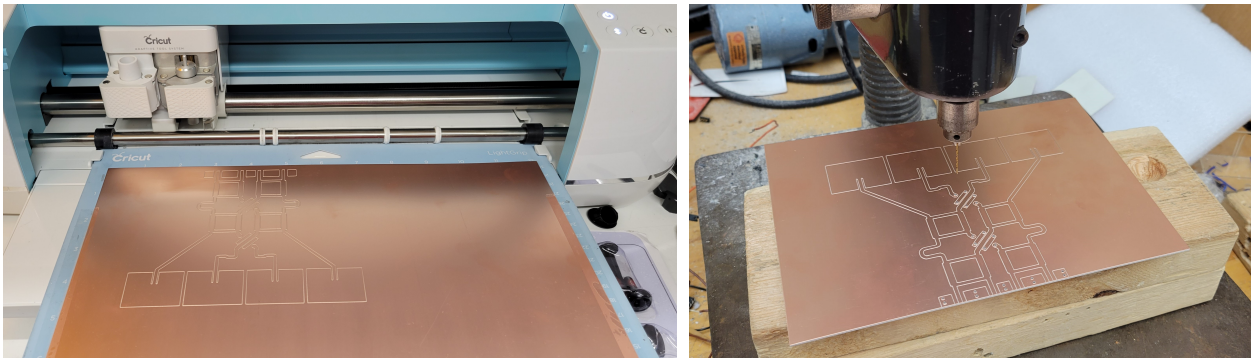

(a) Matrix fabrication with Cricut (b) Butler matrix via drilling

Figure 5.19: Fabrication of transmission line Butler matrix on Rogers RO3006 substrate

the cladding was removed manually and the bottom conductor was scored by hand to create clearance for the transmission line sections in the bottom section of the crossovers (Figure 5.20). Via filling was done by soldering a bare wire in each hole to ensure conductivity. The

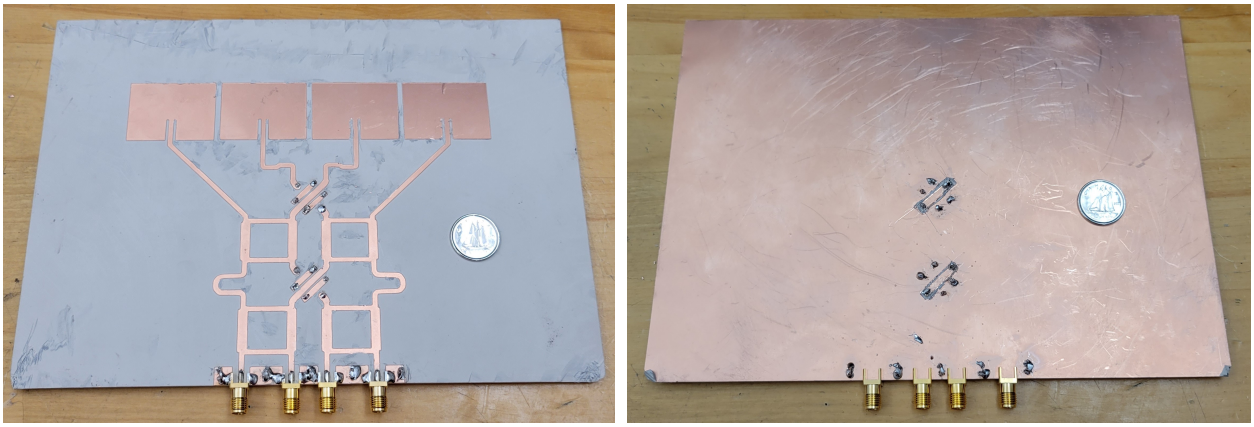

(a) Top view (b) Bottom view

Figure 5.20: Fabricated transmission line Butler matrix complete with connectors

input reflection was measured using a VNA calibrated with a single port open, short load

procedure. Calibration kit Agilent 85052D was used to provide the appropriate terminations [32]. To measure the input reflection of the matrix it was connected to the VNA as seen in Figure 5.21. Unused ports were terminated with 50Ω to ensure proper loading. With the

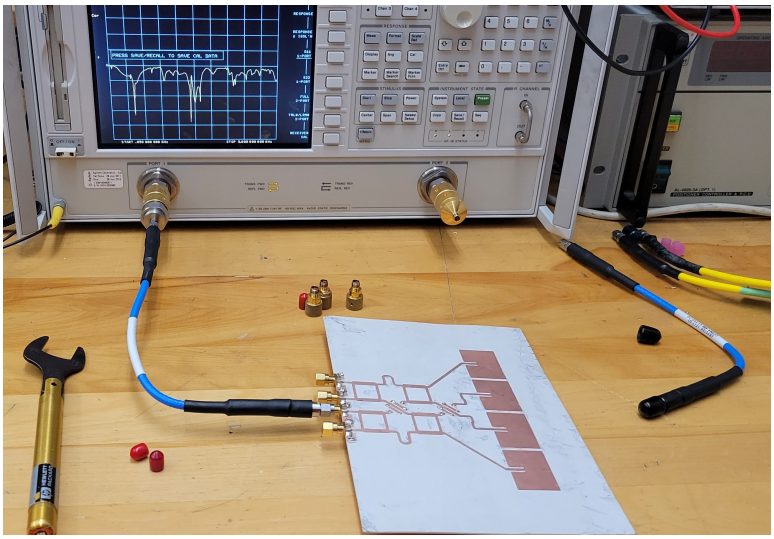

Figure 5.21: Inpur reflection measurement setup for the transmission line matrix

matrix connected input reflection measurements were recorded for each port. The results were then compiled and can be seen in Figure 5.22. Matching can be seen to be -5 dB or better and port 3 is particularly well matched at less than -20 dB at 2.4 GHz. Looking

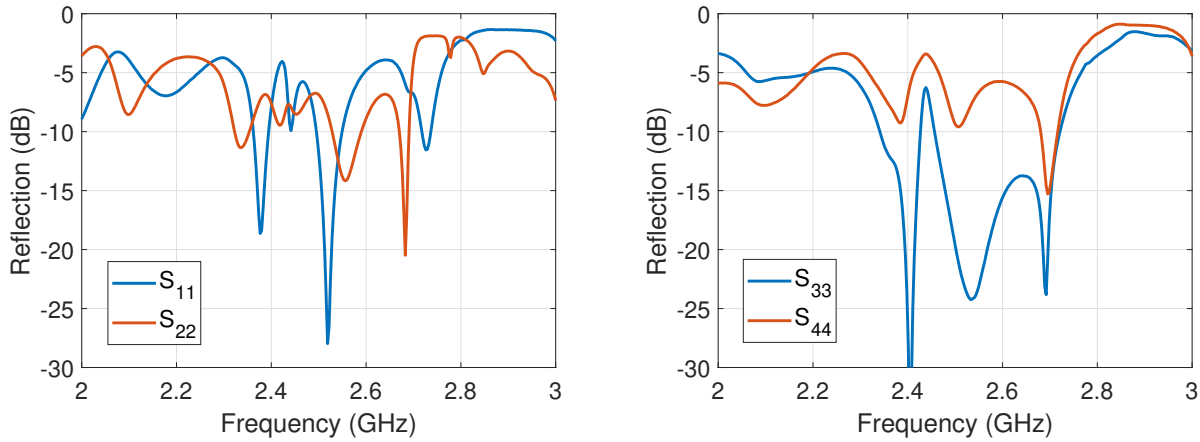

Figure 5.22: Measured input reflection for the transmission line matrix

at the reflection coefficient the location of best match seems to be 2.5 GHz with all ports

close to or better than -10 dB return loss. Despite this potential shift in matching far-field radiation measurements were made at the design frequency of 2.4 GHz. Far-field radiation measurements were made using the anechoic chamber at Carleton University. The chamber measurement setup can be seen in Figure 5.23. Calibration of the chamber was performed

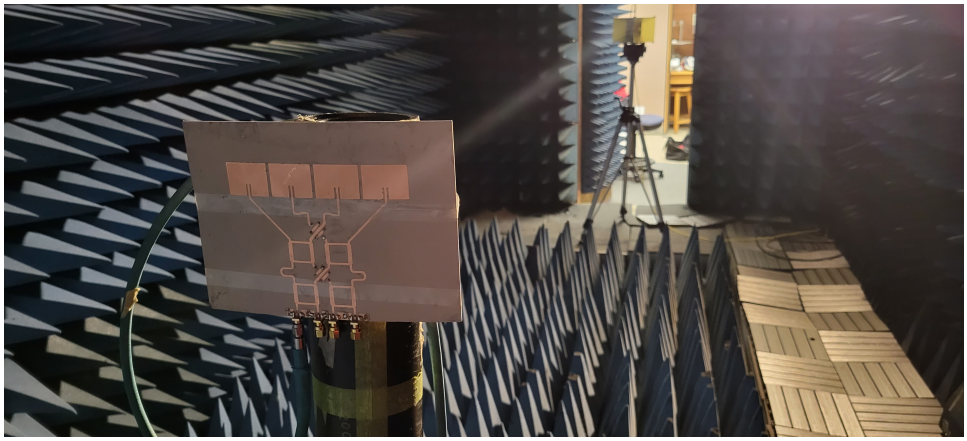

Figure 5.23: Anechoic chamber measurement setup with transmission line matrix

using the H-1498 standard gain horn antenna to account for system losses as was done for the Luneburg lens measurements [51]. Anechoic chamber gain measurements for the matrix can be seen in Figure 5.24 plotted with simulated radiation patterns taking into account tolerances on the via drilling process. Simulations are performed with each of the vias in turn disconnected and then for all the vias disconnected. The nominal simulation results with all vias connected are also shown. Based on the simulations there is a large amount of variability that can be introduced by poor connection of the the through hole vias. Yes this is not enough to fully capture the effects present in the physical measurements.

Comparing these results to the predicted values from Table 5.1 Port 2 produces the radiation lobe most consistent with the predicted theory. From Port 1 the beam peak can be seen outside of 50° while it should be at 15°. Port 2 as well produces a beam centered just outside 50° compared to the predicted value of 45° but the peak gain value is suppressed to just over 0 dBi. Port 3 produces a main lobe of radiation about 20° from broadside with the opposite polarity compared to the predicted value of 45°. Port 4 can be seen to produce

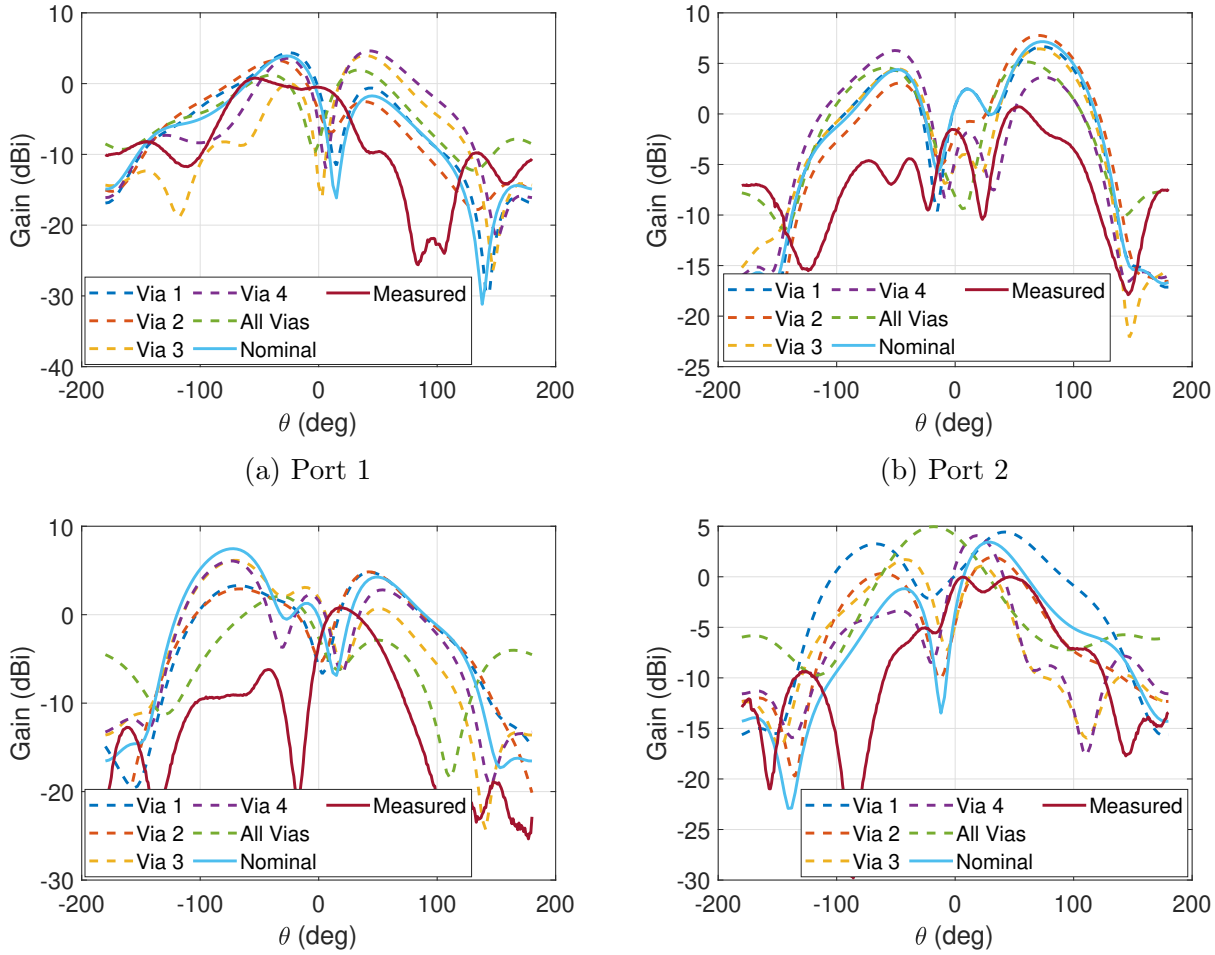

(a) Port 1

(b) Port 2

(c) Port 3

(d) Port 4

Figure 5.24: Far-field radiation patterns for transmission line matrix comparison between measurement and simulation with a sensitivity analysis performed on the through hole vias. Each via in order of proximity to the feeding beam ports is disconnected.

two radiation peaks with one close to broadside and the other close to 50°. Given that the predicted value is 15° the central value is reasonably close. To further investigate the beamforming, the antenna array could be removed so that the array ports could be measured with a VNA. This would allow the phase progression and transmission magnitudes to be investigated and potentially reveal some fabrication flaws.

While there is still work to do making this process capable of generating reliable results the matrix fabrication shown here demonstrates that it is capable of creating radiating elements with some degree of beam steering. One change to make to the design to more closely

reflect the quality of the CNC knife tracing process would be to redesign the crossover to a planar design eliminating the need to drill through hole vias and cut the bottom conductor by hand.

5.3 Lumped element matrix

While a transmission line Butler matrix can produce beamforming with very low loss its size can become cumbersome at low frequencies. When the frequency of operation is sub-GHz the space saving of a lumped matrix may make it a desirable alternative. In this section a Butler matrix will be designed using lumped components at a centre frequency of 915 MHz.

5.3.1 Hybrid Coupler

For the lumped coupler a compact design was used where the symmetry of the device is exploited to remove any connection to the ground plane [62]. Removing the ground connection is beneficial as through hole vias can be bulky and introduce parasitic inductance. Removing them allows the device to be more compact and improves the ability to model with a simple schematic simulator. A schematic of the coupler can be seen in Figure 5.25. For

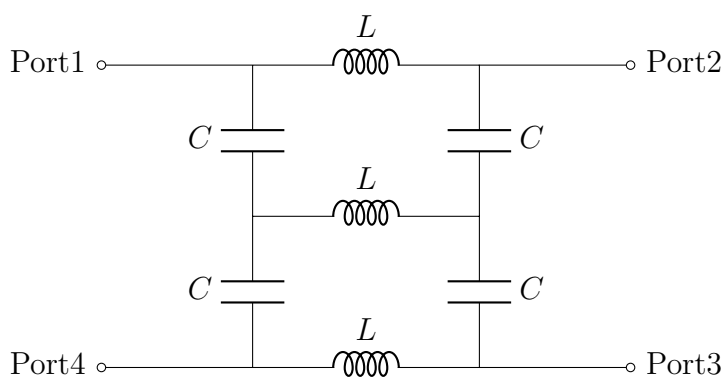

Figure 5.25: Compact quadrature hybrid coupler [62]

proper operation the values of inductance and capacitance must be chosen to preserve the impedance match while splitting power between the output ports with a 90° shift between

them. For this design the lateral circuit connections between Ports 1 and 4 (also 2 and 3) are effectively high pass creating a phase shift between Ports 2 and 3 where Port 3 is leading for a signal applied at Port 1. A redesign of the circuit around a lateral low pass filter topology would result in the opposite phase progression and would match the phase progression of the transmission line matrix but it will be shown that the phase shifter can simply be redesigned for the phase to lead at the output and still produce a functional Butler matrix. The values of inductance and capacitance were chosen for the design as [62]:

$$L = \frac{Z_0}{2\pi f_0} \tag{5.5}$$

$$C = \frac{1}{Z_0 2\pi f_0} \tag{5.6}$$

where Z_0 is the characteristic impedance for the match and f_0 is the centre design frequency. These equations were used to determine initial values which were then tuned in ADS. To increase the accuracy of the simulation an EM model of the coupler footprint was made based on an 0402 device footprint. Schematic components for the inductors and capacitors were then placed between the pads to create an EM co-simulation. This method allows the component values to be tuned with the simulation speed of a schematic model but with the added parasitics and coupling of the EM footprint. With the EM co-simulation the initial values of L and C were tuned to produce the results seen in Figure 5.26. From the initial values both L and C were reduced slightly through tuning as seen in Table 5.3. For the transmission line circuit the phase at Port2 tends to lead the phase at Port3 for an input signal from Port1. Yet for the lumped coupler the opposite holds true and the signal at Port3 leads. For the matrix design this does not pose a major challenge as the topology of

Table 5.3: Initial and final component values of the lumped element hybrid coupler

Component	Initial Value	Final Value
L	8.70 nH	8.2 nH
C	3.48 pF	3.3 pF

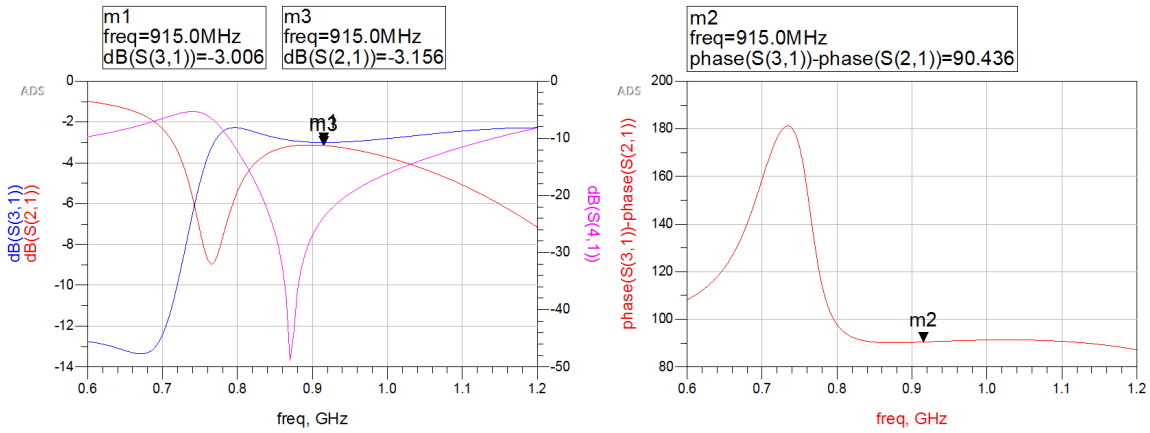

Figure 5.26: Simulated transmission and reflection magnitude (left) and output phase difference (right) for the lumped element hybrid coupler

the phase shifter can be changed to produce a leading phase shift rather than a lagging one.

5.3.2 Phase Shifter

The design requirements for the phase shifter are to provide a 45° phase shift while preserving 50Ω impedance at the input and output ports. Some simple phase shifter layouts that could meet these requirements include π and T networks in either high or low-pass configuration. Since a phase shift of 45° is required with a leading polarity a high-pass circuit should be used. To chose between the π and T network topologies the circuit assembly should be considered. Two considerations for design are:

- capacitors are typically easier to solder than inductors as the later often has a polymer coating that is easy to melt and delicate pads that can be difficult to contact
- soldering components to ground is more time consuming since ground planes often make effective heat sinks.

Based on these considerations the high-pass T-network is most convenient to assemble since it requires only one inductor and one connection to ground. A schematic of the high-pass T-network phase shifter used for the design can be seen in Figure 5.27. To set the initial

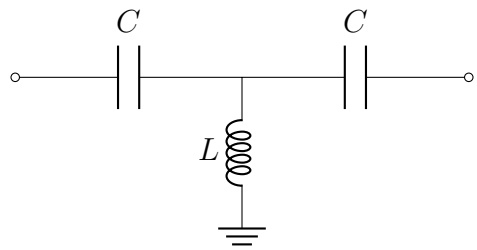

Figure 5.27: T-network phase shifter topology

component values for the phase shifter design, equations from [63] were used. The capacitors for the phase shifter were calculated as:

$$C = \frac{1}{2\pi f_0 Z_0(\cot(\theta) - \csc(\theta))} \tag{5.7}$$

and the inductor value was calculated as:

$$L = -\frac{Z_0 \csc(\theta)}{2\pi f_0} \tag{5.8}$$

where Z_0 is the design impedance, f_0 is the centre frequency, and θ is the effective electrical length of the phase shifter, in this case -45°. With the initial values calculated, a model of the phase shifter was made in ADS for tuning. As done for the coupler, an EM model of the footprint was made for simulation to account for the parasitics. With the schematic components simulated along side the EM footprint, the component values were tuned resulting in the circuit performance as seen in Figure 5.28. The initial and final tuned values for the phase shifter can be seen in Table 5.4.

Table 5.4: Initial and final component values of the lumped element phase shifter

Component	Initial Value	Final Value
L	12.3 nH	11.0 nH
C	8.4 pF	7.7 pF

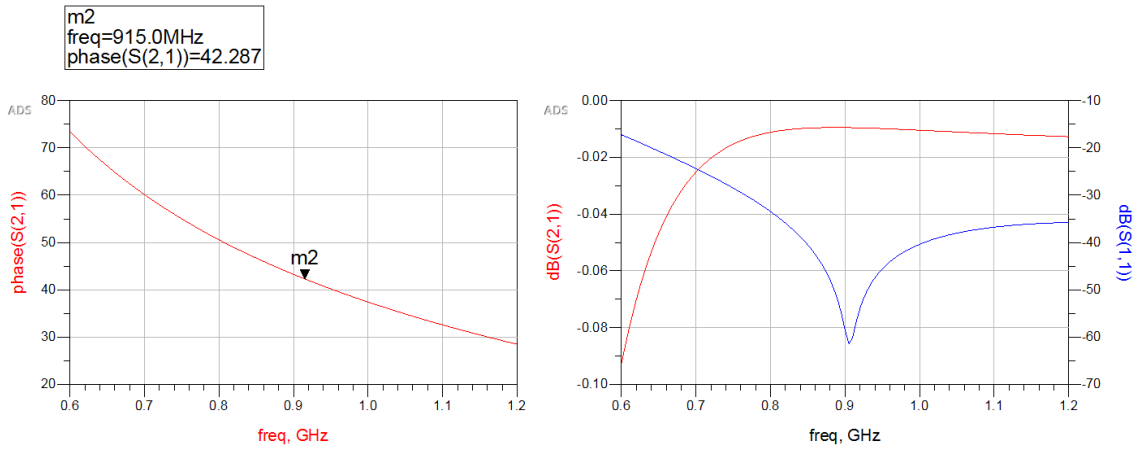

Figure 5.28: Phase shift (left) and transmission/reflection (right) for the lumped element phase shifter

5.3.3 Crossover

For the crossover design a simple approach was taken utilising the second conductor plane and through hole vias. Given the low frequency of operation, the electrical lengths of the crossover branches were considered negligible; although it can be seen in Figure 5.29 that they are about 10°. The size of the crossover was set to provide enough spacing at the input

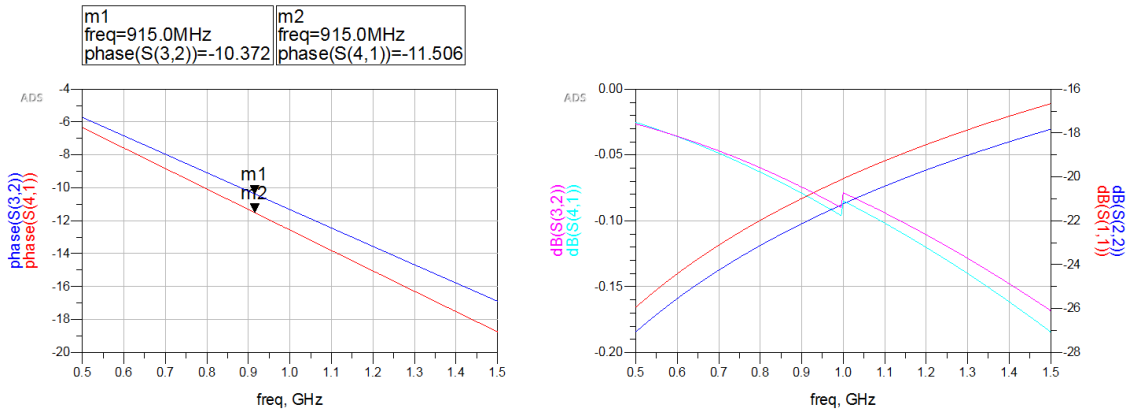

Figure 5.29: Lumped crossover simulated electrical length (left) and transmission magnitude (right)

ports for the SMA connectors to be soldered side by side. A square geometry was used so that the lines would cross each other at a perpendicular angle and minimise the coupling.

5.3.4 Layout Simulation

To verify the operation of the circuit as a whole before fabrication, an EM model was made with all components as seen in Figure 5.30. As for the constituent parts, the assembled

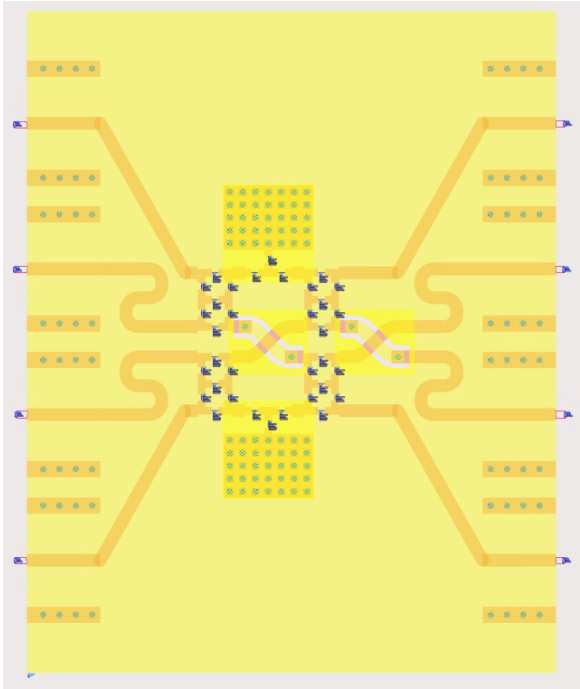

Figure 5.30: EM model and testbench for the lumped Butler matrix

circuit was simulated with a co-simulation model involving an EM footprint and schematic components placed between the pads. This method of simulation could allow a final tuning to be done on the circuit (although for this design the values found during the component designs were found to be sufficient). The simulated transmission parameters of the matrix can be seen in Figure 5.31. In this simulation the phase progression for each input port can be seen to follow that described in Table 5.1 except that the signs are reversed. This is to be expected since the lagging phase shifts of the transmission line matrix are leading in the lumped variant. In addition to the transmission parameters of the matrix, its input reflection was also simulated and plotted as seen in Figure 5.32. It can be seen that all ports are matched to better than -15 dB at the centre frequency of 915 MHz.

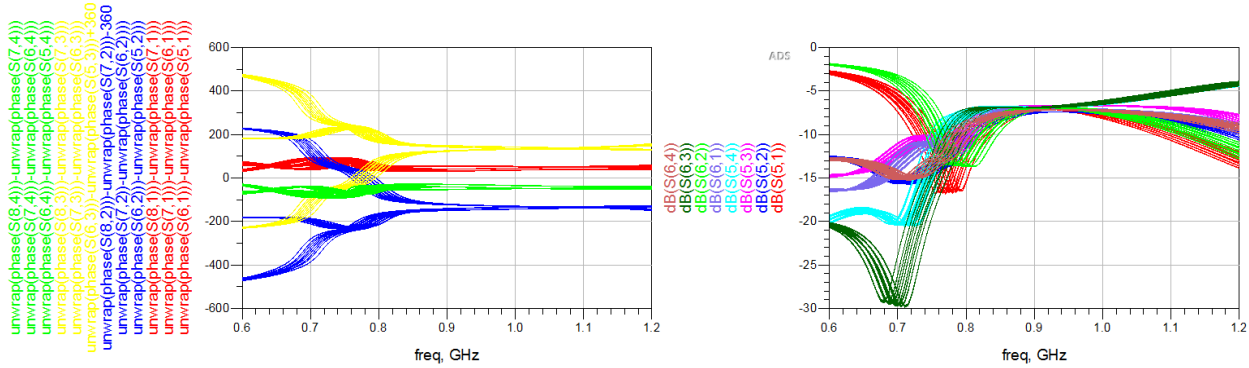

Figure 5.31: Simulated phase progression (left) and transmission magnitude (right) taking into account the tolerance on each of the components. In this case ±2% for the inductors and ±0.1 pF for the capacitors.

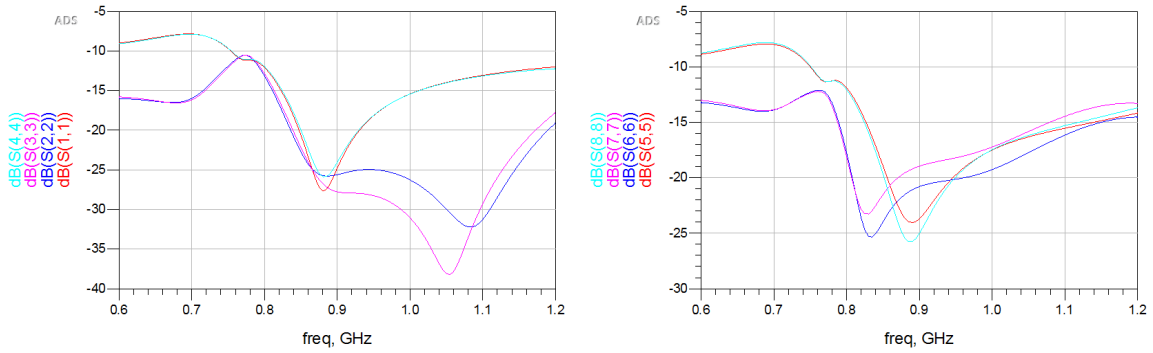

Figure 5.32: Simulated magnitude of reflection coefficient from beam (left) and array (right) ports

5.3.5 PCB Assembly and Measurement

Assembly of the lumped matrix was done manually using a microscope and soldering iron. Components for the matrix were chosen based on their nominal value and tolerance to ensure operation close to the simulated design. A summary of the components selected for the design can be seen in Table 5.5. Another important parameter to consider for component selection

Table 5.5: Component table for the lumped Butler matrix

Component	Nominal Value	Tolerance	Manufacturer	Part Number
$L_{coupler}$	8.2 nH	±2%	Delta Electronics	0402HP-8N2EGTS
$C_{coupler}$	3.3 pF	±0.1 pF	Johanson Technology	500R07S3R3BV4T
$L_{shifter}$	11 nH	±2%	Delta Electronics	0402HM-110EGTS
$C_{shifter}$	7.7 pF	±0.1 pF	KEMET	CBR04C779B5GAC

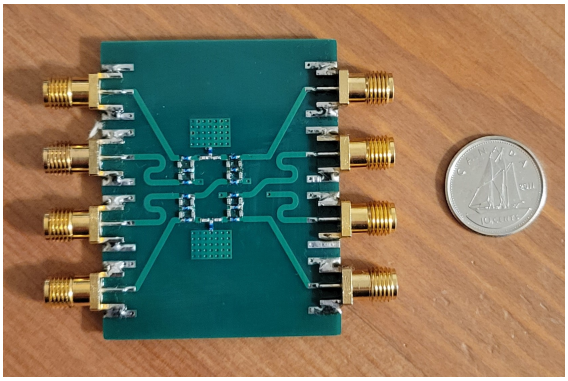

(a) Top view

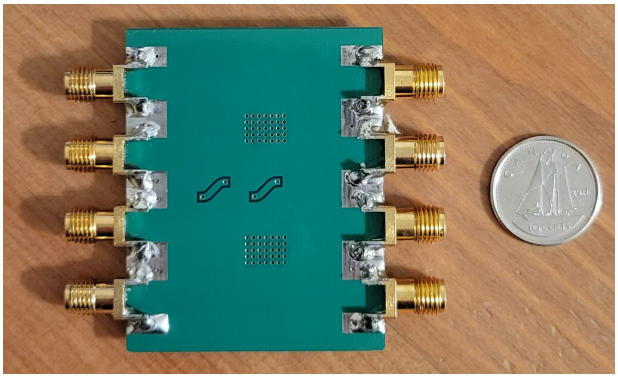

(b) Bottom view

Figure 5.33: Fabricated and populated lumped Butler matrix

is the self resonant frequency. While this figure was not available for all components selected it is important to operate well below the SRF for component values to be as quoted and consistent.

The components were assembled on the PCB and can be seen with both top and bottom views in Figure 5.33. Care was taken to ensure that all components were properly soldered by returning heat to the initial solder pad of each component and ensuring it was not floating. This is an important step, especially for capacitors, as their contact cannot easily be verified with a multimeter. To measure the matrix it was connected to a VNA for two part S-parameter measurements as shown in Figure 5.34. All ports not connected to the VNA were terminated with 50Ω loads to ensure proper loading for the circuit. A total of 16 separate two port measurements were made with each of the beam and array ports being connected to VNA ports 1 and 2 respectively (in turn). This gives a complete characterisation of the transmission and reflection characteristics of the circuit for comparison with the simulated circuit. A collection of the measured transmission magnitudes can be seen in Figure 5.35. Interestingly for this measurement there is one weak output signal for each of the beam ports. For the low transmission, from beam ports 1 and 2 to array port 5, a possible explanation could be an issue with the phase shifter. Possibly a poor solder joint or a component slightly melted by the iron during soldering. But if this were the case it should also affect the transmission from either of these beam ports (1 and 2) to port 7. For the low transmission

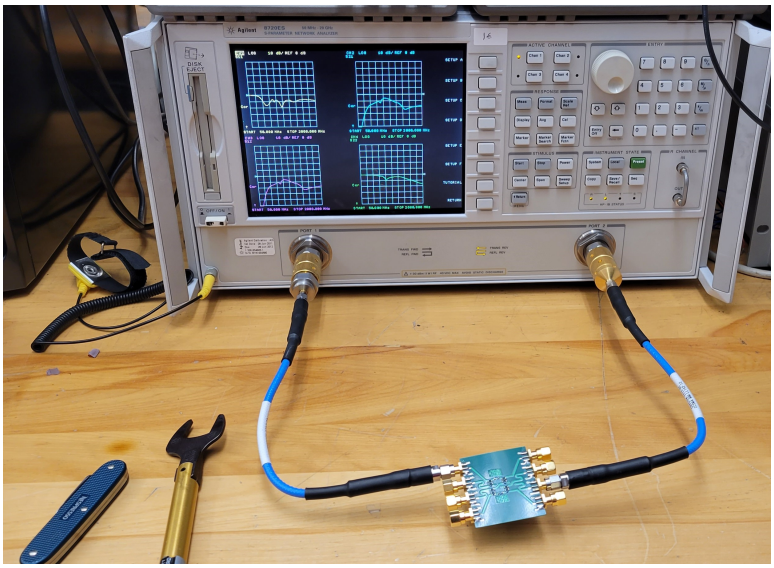

Figure 5.34: VNA measurement setup for the lumped Butler matrix with terminations

to port 7 from beam ports 3 and 4 an explanation could be that the signal must traverse both crossover circuits. Since the crossover circuits represent a discontinuity either from the vias or a disruption in the ground plane, this could explain the low transmission, yet it would not explain why numerous other signals traverse the crossovers without significant issue.

Uneven distribution of power across the array ports can cause distortions in the far-field beamforming but a far more important parameter for the matrix is the phase progression. Since the phase progression determines the locations of constructive and destructive interference if all array elements are adding together they can still form a coherent beam even if they providing different power levels. Plots of the phase progression for each beam port can be seen in Figure 5.36. Notably the phase progressions do not hold to a consistent grouping as simulated. Ports 1 and 4 show the most correspondence with their predicted values of 45° and -45° respectively while the phase progressions for Ports 2 and 3 overlap with those from Ports 1 and 4, and do not represent their predicted ±135°. A likely cause for this is that some components are approaching SRF and are displaying erratic values. To address this in a future design more attention could be made when picking the components to ensure a high SRF that is at least double the frequency of operation. This could be particularly

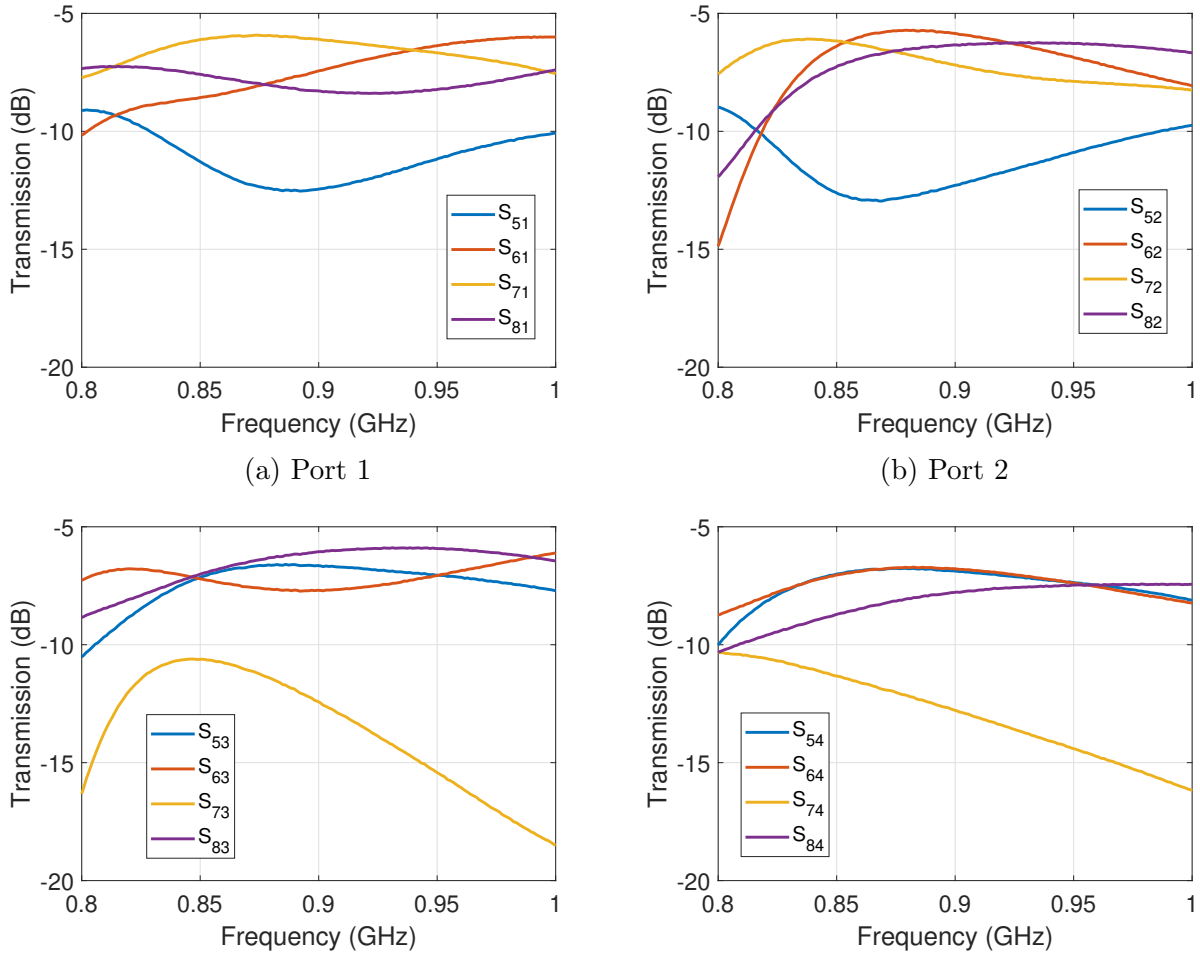

(a) Port 1

(b) Port 2

(c) Port 3

(d) Port 4

Figure 5.35: Measured transmission magnitude from beam ports to array ports

important for the inductors which can resonate with the parasitic capacitance between coils at small sizes. Possibly using larger 0603 inductors could raise their resonance and improve performance.

The final measurement to present for the lumped matrix is return loss from each port. Measured reflections in dB can be seen in Figure 5.37 where ports 2, 4, 6 and 8 show excellent matching at -15 dB or better while ports 1, 3, 5 and 7 show more return loss between -10 and -5 dB. While these values indicate that the majority of power is transitioning through the ports it is likely that they could be improved by different component selection as discussed above.

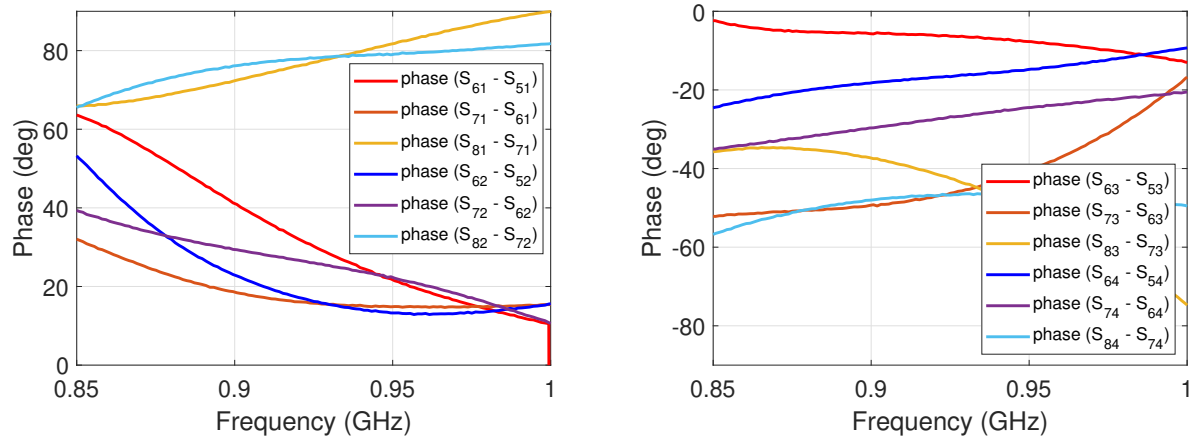

(a) Beam ports 1 and 2 (b) Beam ports 3 and 4

Figure 5.36: Phase progression across array ports for each of the beam ports

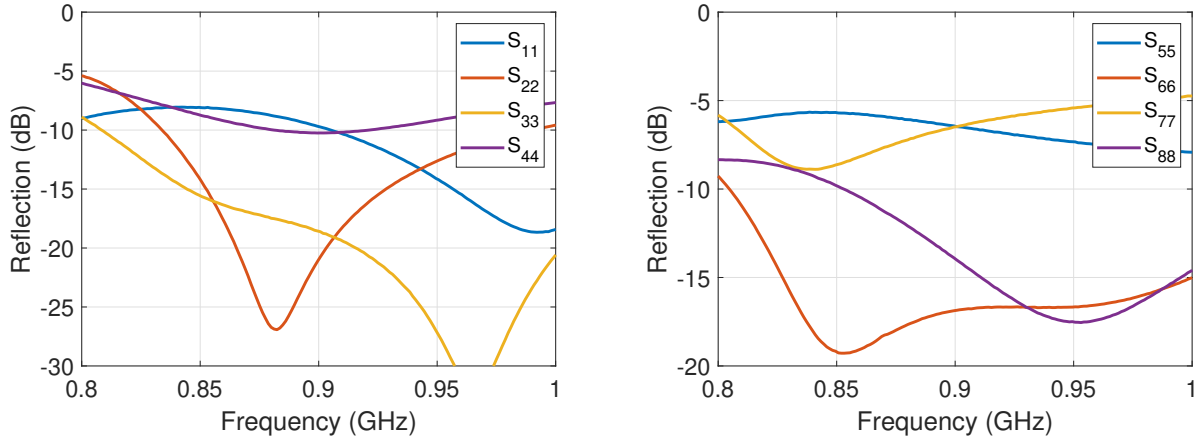

(a) Beam ports (b) Array ports

Figure 5.37: Measured magnitude of reflection coefficient from beam and array ports

Chapter 6

Ferroelectric Varactors

Ferroelectric materials have become a viable solution for microwave circuits requiring tunability [64]. One device that can benefit directly from a tunable dielectric permittivity is a capacitor. Typical varactor applications involve active semiconductor devices that introduce noise (particularly 1/f noise) into a system [65][66]. A ferroelectric varactor derives its tunability from the permittivity of the substrate rather than the size of the depletion region. For a parallel plate capacitor with capacitance [67]

$$C = \varepsilon \frac{A}{d} \tag{6.1}$$

the value is linearly dependant on the permittivity ε and the coefficient of the relation is determined by the plate area A and gap between them d. A linear relation is advantageous for tuning as it allows for simple relations between input voltage and tuning parameters. To preserve the linear relation, a ferroelectric substrate should be chosen that also exhibits a linear response over the tuning range of interest. An effective ferroelectric for this purpose is Barium Strontium Titanate (BST). This ferroelectric material has a large nominal permittivity with a linear tuning range; it is also 3D printable [68][69].

An ideal application for ferroelectric varactors is integration into a tunable bandpass filter on flexible electronics. With flexible substrates such as PET becoming popular for wearable

electronics [53][70][71] it is ideal to make as much of the supporting electronic circuit flexible as well. Printed ferroelectric materials can exhibit flexibility making them an ideal candidate for flexible, wearable electronics [68].

6.1 SMA connected varactors

The varactros were designed to interface with the VNA for measurement through SMA connectors for convenience. With a frequency rating up to 18 GHz 5mm SMA connectors make an ideal choice for many RF and microwave applications.

6.1.1 Simulation and modeling

An em model of the varactors was created in HFSS for simulation. The model used a commercial Rogers substrate for the feeding lines and to provide some mechanical stability to the device. With two 50 Ω transmission lines feeding parallel plates as shown in Figure 6.1 with the BST doped substrate insulating them. This varactor model provides a challenge to

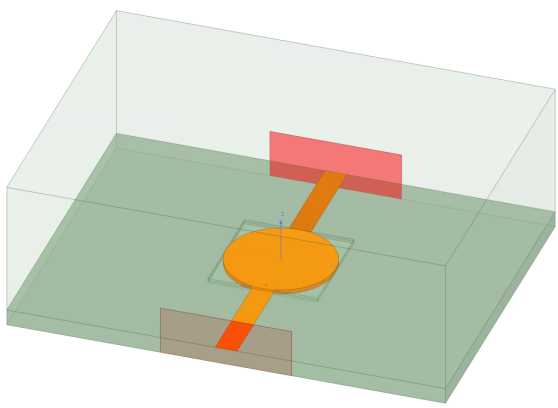

Figure 6.1: HFSS model of SMA connected varactor with RO4350 dielectric ($\varepsilon_r = 3.66$, tanδ = 0.0035) used for the base substrate and a tunable substrate with variable permittivity and loss tangent used for the dielectric between the varactor plates.

measuring the capacitance between the parallel plates, mainly the shunt paracitic capacitance to ground through the Rogers substrate. To extract the series capacitance of the parallel

plates they were modelled as a pi network with an admittance matrix as [72]

$$\mathbf{Y} = \begin{bmatrix} y_{10} + y_{12} & -y_{12} \\ -y_{12} & y_{20} + y_{12} \end{bmatrix} \tag{6.2}$$

where the admittance parameters have a circuit representation as in Figure 6.2. Converting the measured S-parameter matrix to a Y-parameter admittance matrix allows the series admittance to be extracted as the negative of either $\mathbf{Y}_{21}$ or $\mathbf{Y}_{12}$. Since the VNA measures

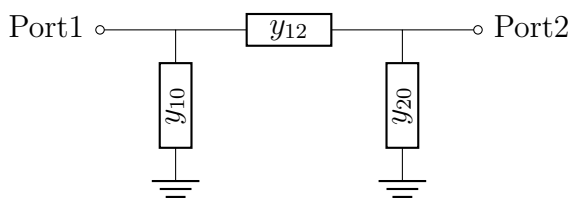

Figure 6.2: Pi-network model for reciprocal two-port device [72]

the S-parameter matrix of a network it is useful to write the conversion to Y-parameters for determining the series admittance. The series admittance can be written as [35]

$$y_{12} = -\mathbf{Y}_{21} = Y_0 \frac{2S_{21}}{(1 + S_{11})(1 + S_{22}) - S_{12}S_{21}} \tag{6.3}$$

where Y_0 is the characteristic admittance used as reference for the measurement of S-parameters. This measurement provides a complex number as a function of frequency for the admittance that can be modelled using lumped components. The real component can be modelled by a resistance while the imaginary component could be modelled as either inductive or capacitive. For this analysis a capacitor will be used as the reactive component. It should be noted that any negative values of capacitance will simply indicate that the reactance is inductive at the given frequency. Based on the admittance circuit model in Figure 6.3 the capacitance can be extracted as

$$C = \frac{\Im\{y_{12}\}}{\omega} \tag{6.4}$$

and the quality factor as

$$Q = \frac{\Im\{y_{12}\}}{\Re\{y_{12}\}} \tag{6.5}$$

where y_{12} is the admittance as calculated in Equation (6.3).

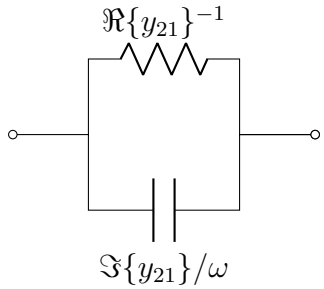

Figure 6.3: Capacitive admittance model with values derived from admittance parameters

6.1.2 Fabrication and measurement

The varactors were fabricated using the Cricut cutter knife tracing tool and copper tape. This method allows the copper tape to be cut with precision and aligned by hand with the ferroelectric material placed between the plates (Figures 6.5, 6.9). To calibrate the VNA before measuring the varactors a through section of transmission line as seen in Figure 6.4 was fabricated to remove the impact of the feedlines. A two port SOLT calibration was then performed using the Agilent 85052D 3.5 mm calibration kit as shown in Figure 3.2 and the through line. The calibration process was performed with RF bias tees on either port to allow a DC bias to be placed across the ferroelectric. A variable 25 V DC power supply was connected in series with a fixed 30 V supply to provide the bias. This allowed a sweep to be done from 0 V (or unbiased) to a maximum of 55 V. While this is a substantial bias range compared to many conventional semiconductor varactor circuits, it does not relate equivalently to the ferroelectric device. With a thickness of 350 um the electric field strength biasing the substrate can be calculated as:

$$E = \frac{V}{d} = \frac{55V}{350um} = 157kV/m \tag{6.6}$$

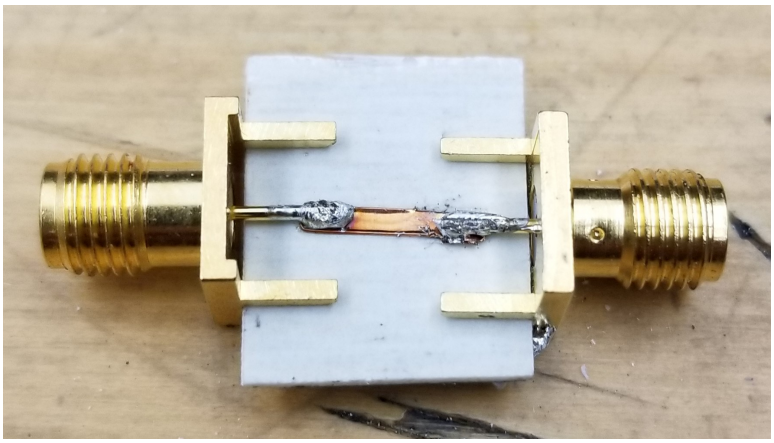

Figure 6.4: Through line for SMA connected varactor calibration

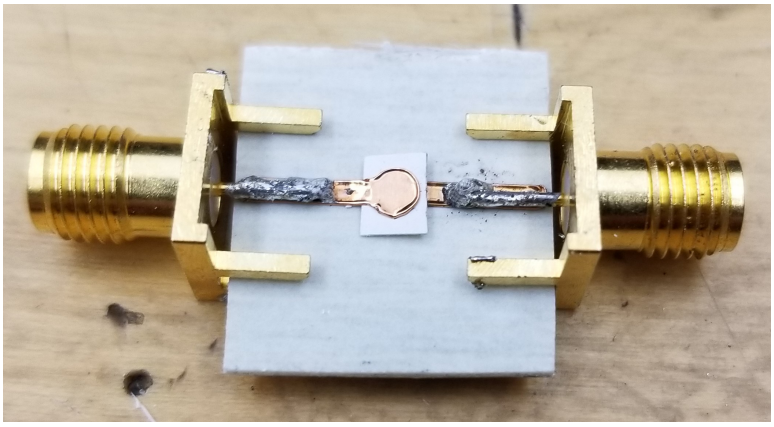

Figure 6.5: SMA connected varactor with a 3 mm plate width

for a maximum value compared to nominally unbiased. It has been shown that a BST doped substrate can achieve a tuning range of 63% for an applied electric field range of 1.4 MV/m [69]. Given that this range is roughly nine times what is achievable with the setup presented here, a tunability of roughly 7% can be expected. This tunability range depends on the substrate itself as not all doped substrates have the same concentration of BST nanoparticles. For the varactors presented here the density of BST doped by weight was 75%.

6.1.2.1 Measurement of 3 mm varactors

Measurements were made with the DC power supplies connected for the unbiased points as well to add consistency. Starting with the unbiased measurement, the DC power supply was left powered down and the 2-port S-parameter data was measured for the 3 mm varactor. After measuring the unbiased data point, the bias was increased to 30 V by turning on the power supply with the 30 V bias supplying the voltage and the variable 25 V supply set to 0 V. Before measuring the S-parameters, a DMM was used to meassure the voltage across the plates to ensure the appropriate value was applied. The S-parameters were then measured for this (30 V) bias point. Finally, the variable supply was set to 25 V for a total voltage across the plates of 55 V. This value was confirmed with a DMM before the S-parameter data was captured for this (55 V) bias point.

To convert the measured S-parameter data to capacitance and quality factor data for the varactors, Equations (6.4) and (6.5) were used in conjunction with Equation (6.3). The capacitance can be seen plotted in Figure 6.6 with two distinct frequency ranges for readability. At low frequencies below 100 MHz the capacitance was measured at 680 fF which

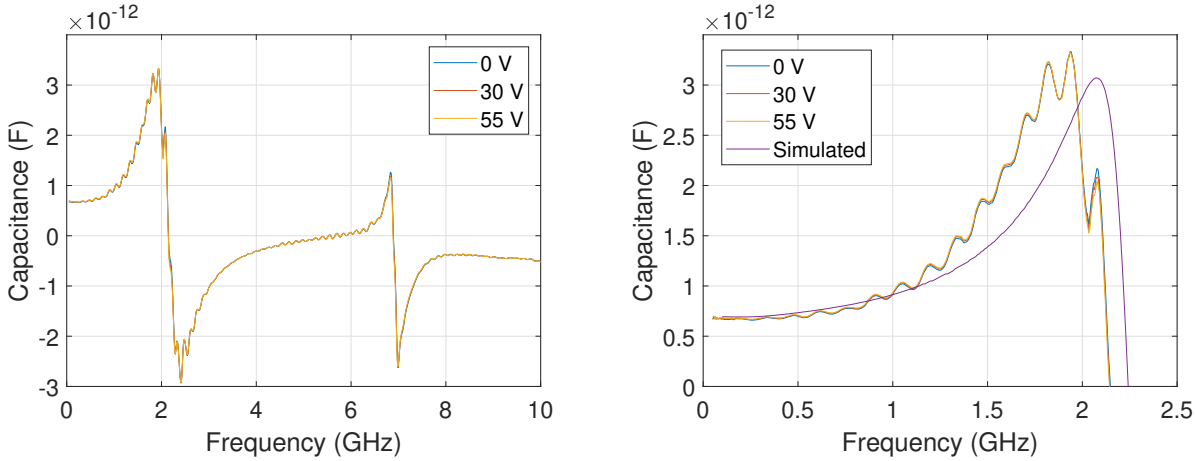

(a) (b)

Figure 6.6: Capacitance comparison between simulation and measurement for 3 mm SMA connected varactors using the HFSS model for simulation from Figure 6.1 ($\varepsilon_r = 3.4$, $\tan\delta = 0.25$)

can be back simulated to fit by tuning the properties of the ferroelectric. In Figure 6.6b

the HFSS simulation data can be seen fit to the measured data. To fit the simulated data, permittivity and loss tangent were tuned manually until a fit was achieved. This process resulted in ferroelectric values of $\varepsilon_r = 3.4$ and $\delta = 0.25$ which indicates the BST is not being polarised and contributing to the substrate permittivity, and it is simply adding a significant source of loss. To display the tunability of the varactor, two frequency points were used to plot the capacitance as a function of bias as seen in Figure 6.7. For each of these points the percentage tunability can be calculated as 0.9% at 230 MHz and 1.4% at 417 MHz. These values are significantly lower than the roughy 7% of expected tunability

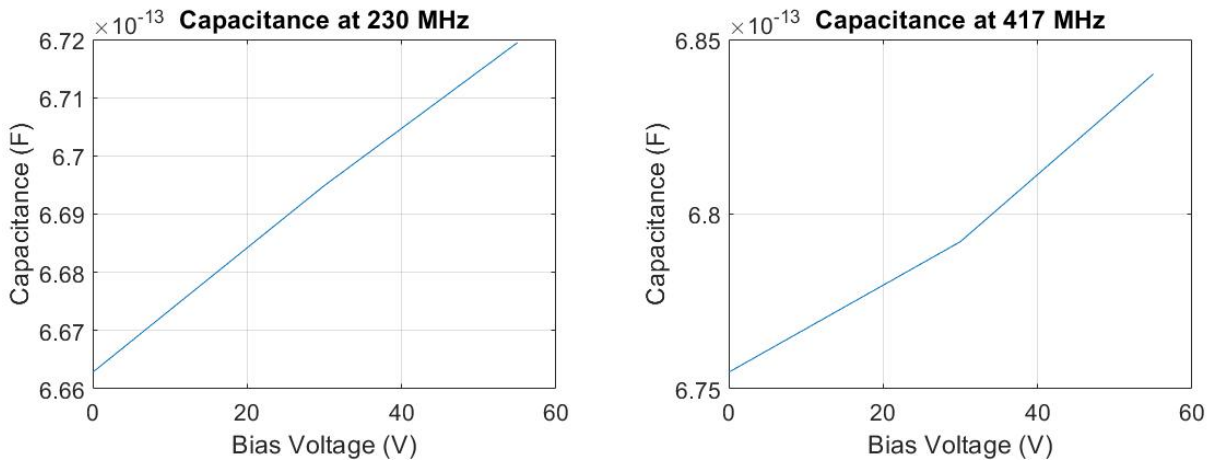

(a) (b)

Figure 6.7: Capacitance as a function of DC boas voltage for 3 mm SMA connected varactors

derived from literature. It is also notable that a value of 3.4 for permittivity was used to back simulate the capacitance while a reported value in the hundreds was found leading to 63% tuning at a 1.4 MV/m bias range [69]. To further compare the simulated HFSS model with measurement, the quality factor was calculated and plotted as seen in Figure 6.8. For the full frequency range to 10 GHz, the quality factor was considered negative at points where the varactor became inductive. This could be remedied by taking the absolute value of the imaginary component of admittance in Equation (6.5) but the investigation here is focused on the capacitive regions.

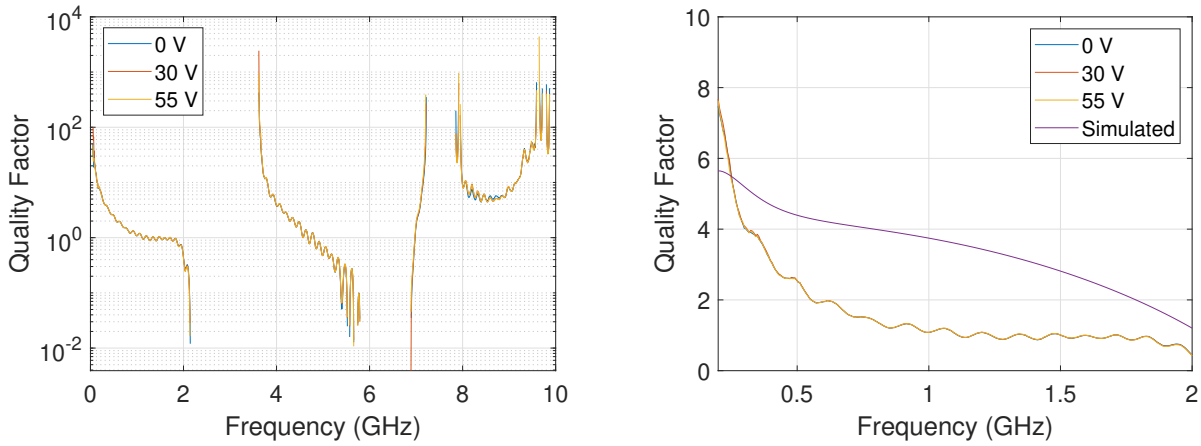

(a) (b)

Figure 6.8: Quality factor comparison between simulation and measurement for 3 mm SMA connected varactors using the HFSS model for simulation from Figure 6.1 ($\varepsilon_r = 3.4$, $\tan\delta = 0.25$)

6.1.2.2 Measurement of 5 mm varactors

Fabrication and measurement of the 5 mm varactros was done using the same procedure as for their 3 mm counterparts. Measurements were made with the DC power supplies

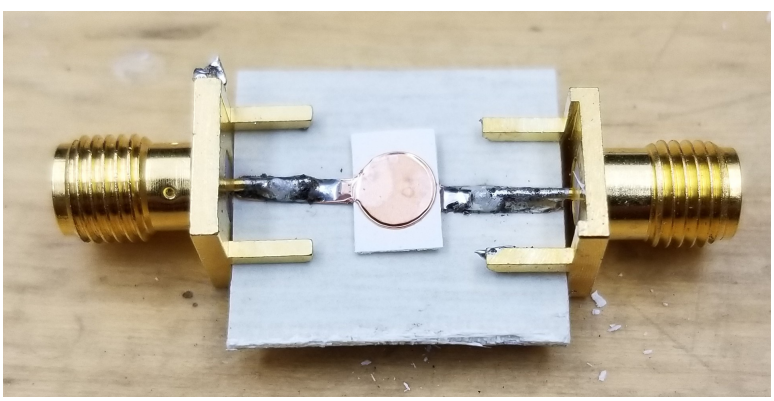

Figure 6.9: SMA connected varactor with a 5 mm plate width

connected for the unbiased points as well for added consistency. Starting with the unbiased measurement the DC power supply was left powered down and 2-port S-parameter data was measured for the 5 mm varactor. After measuring the unbiased data point the bias was increased to 30 V by turning on the power supply with the 30 V bias supplying the voltage and the variable 25 V supply set to 0 V. Before measuring the S-parameters a DMM was

used to measure the voltage across the plates to ensure the appropriate value was applied. The S-parameters were then measured for this 30 V bias point. Finally, the variable supply was set to 25 V for a total voltage across the plates of 55 V. This value was confirmed with a DMM before the S-parameter data was captured for this 55 V bias point.

To convert the measured S-parameter data to capacitance and quality factor data for the varactors Equations (6.4) and (6.5) were used in conjunction with Equation (6.3). The capacitance can be seen plotted in Figure 6.10 with two distinct frequency ranges for readability. At low frequencies below 100 MHz the capacitance was measured at 1.18 pF which

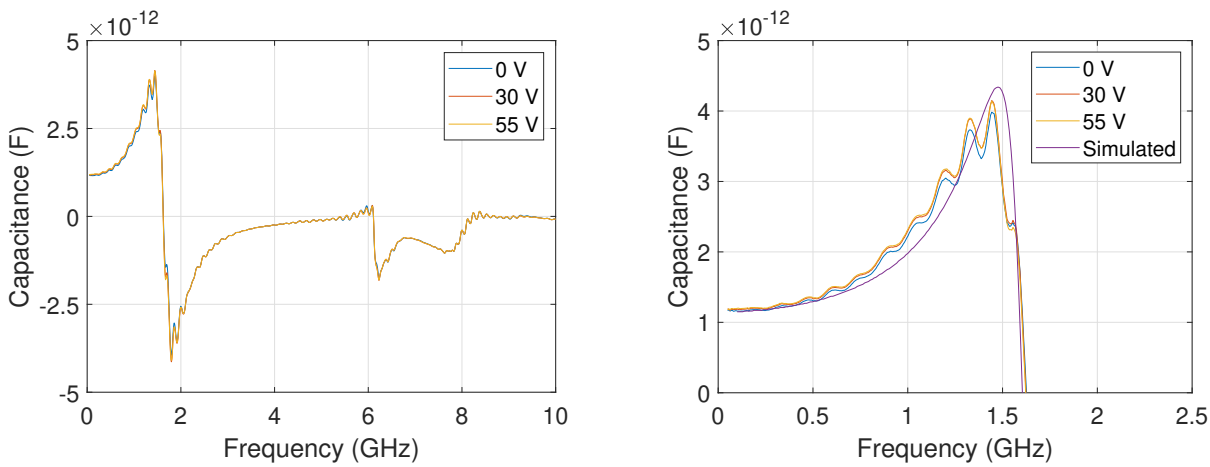

(a) (b)

Figure 6.10: Capacitance comparison between simulation and measurement for 5 mm SMA connected varactors using the HFSS model for simulation from Figure 6.1 ($\varepsilon_r = 3.4$, $\tan\delta = 0.25$)

can be back simulated to fit by tuning the properties of the ferroelectric. For this back simulation the substrate properties were left as found from the 3 mm simulation since both varactors contain identical substrate. In Figure 6.10b the HFSS simulation data can be seen fit to the measured data. To display the tunability of the varactor two frequency points were used to plot the capacitance as a function of bias as seen in Figure 6.11. For each of these points the percentage tunability can be calculated as 2.9% at 230 MHz and 3.0% at 417 MHz. These results show closer agreement with the predicted results from literature yet the back simulated vales for permittivity and loss tangent are still low and high respectively [69].

To further compare the simulated HFSS model with measurement, the quality factor was calculated and plotted as seen in Figure 6.12. For the full frequency range to 10 GHz, the

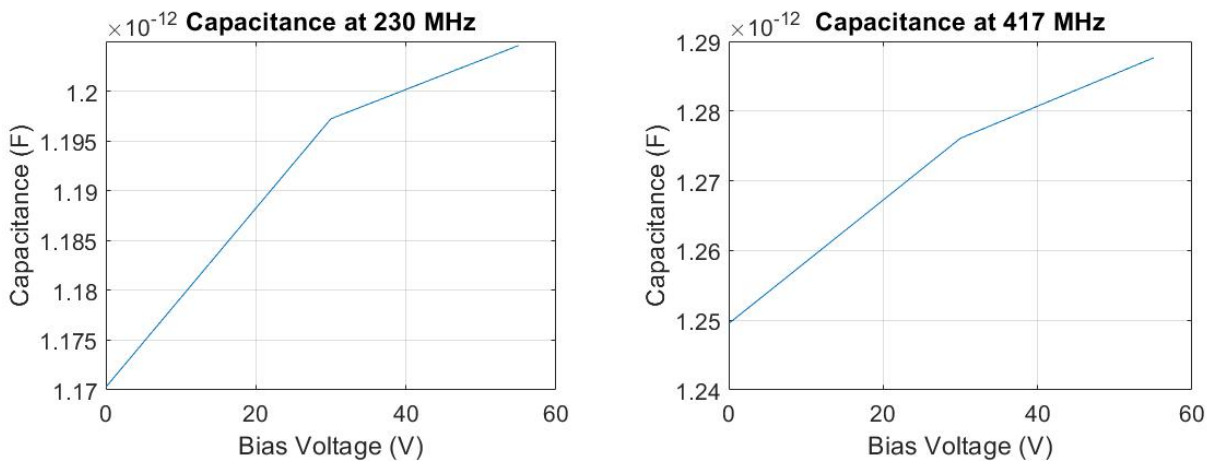

(a) (b)

Figure 6.11: Capacitance as a function of DC boas voltage for 5 mm SMA connected varactors

quality factor was considered negative at points where the varactor became inductive. This could be remedied by taking the absolute value of the imaginary component of admittance in Equation (6.5) but the investigation here is focused on the capacitive regions. For the

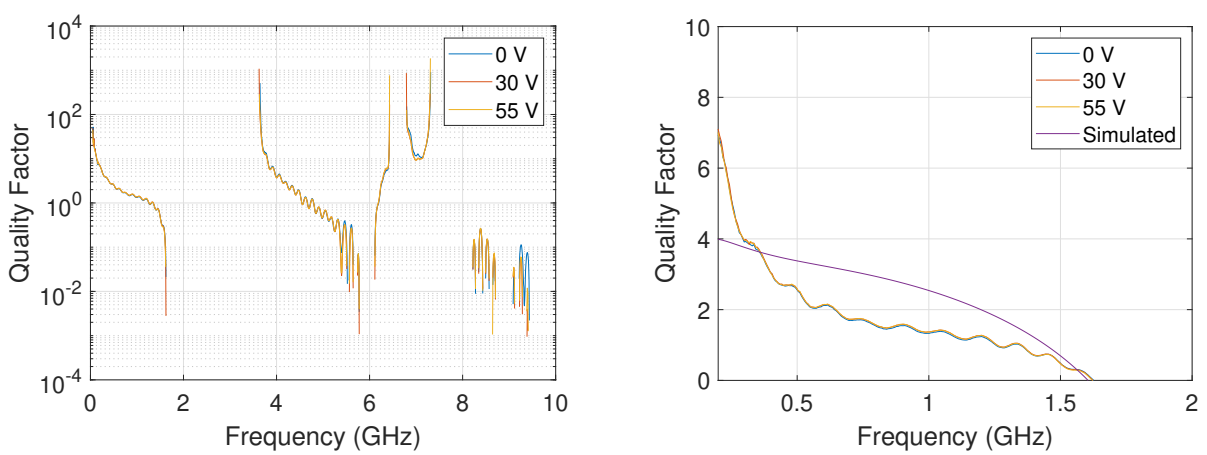

(a) (b)

Figure 6.12: Quality factor comparison between simulation and measurement for 5 mm SMA connected varactors using the HFSS model for simulation from Figure 6.1 ($\varepsilon_r = 3.4$, $\tan\delta = 0.25$)

SMA connected varactors, some tunability was found but less than expected. With such

a low tunability coupled with a low quality factor it will likely be challenging to incorporate these devices into a functional circuit. Having a low resonant frequency also presents a challenge to using these varactors above 100 MHz. While the tunability design challenges most likely need to be investigated from a material science perspective, the low resonant frequency can be addressed through an electrical analysis. An approach to increasing the resonant frequency is shown in the next section through miniaturisation and probing.

6.2 Probed varactors

To increase the resonant frequency of the varactors, their plate area and feed lengths were reduced to minimize the parasitic inductance resonating with the capacitance. The ground plane was also removed from below the varactor to reduce the shunt paracitic capacitance. While SMA connectors are a versatile tool for transitioning signals to a device, they require a section of transmission line to feed a device. This transition can introduce enough paracitics to disrupt a sensitive measurement. To increase the sensitivity of measurement, the varactor was redesigned to be measured with a Picoprobe as seen in Figure 6.13 with 250 um pitch and GSG configuration. An EM model in ADS was used as seen in Figure 6.14 with a

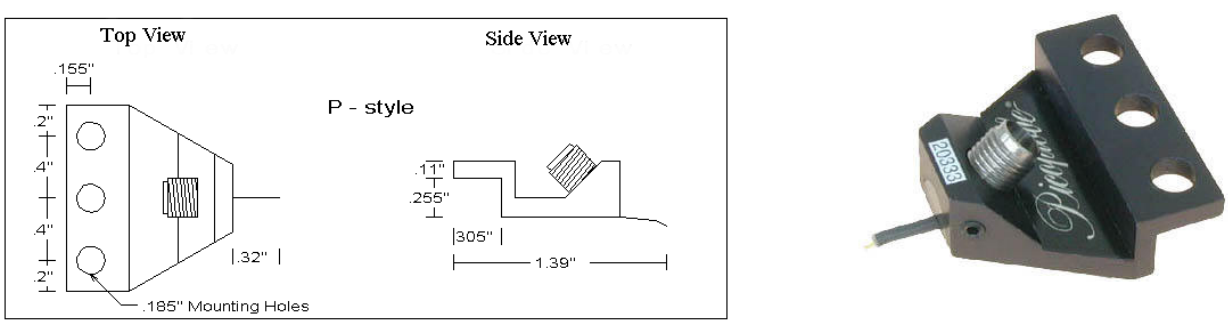

Figure 6.13: P-style GGB model 40a Picoprobe diagram [73]

coplanar ground plane spaced for probe landing. The plate radius was reduced to 300 um and the feedlines were made 500 um (see Figure 6.14). For fabrication the Cricut cutter was used to trace out the varactor plates from copper tape. With such tight tolerances, all pieces

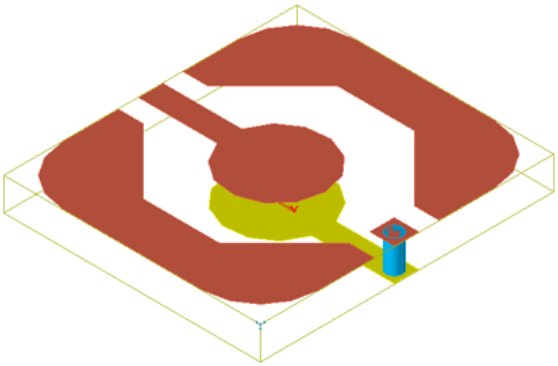

Figure 6.14: ADS EM varactor model with 600 um plates. The entire substrate is made variable for this model to capture the effect of the tunable ferroelectric.

were cut individually and aligned by hand under a microscope. Cutting the ground plane with the Cricut was not possible due to the narrow gap which required the co-planar ground to be cut manually with a knife under a microscope. To assemble the varactor, a piece of structural Rogers RO4350 dielectric without cladding was used to assemble the device [74]. With the bottom plate and ground plane placed on the RO4350, the ferroelectric was placed above the bottom plate followed by the top plate as seen in Figure 6.15. To measure the

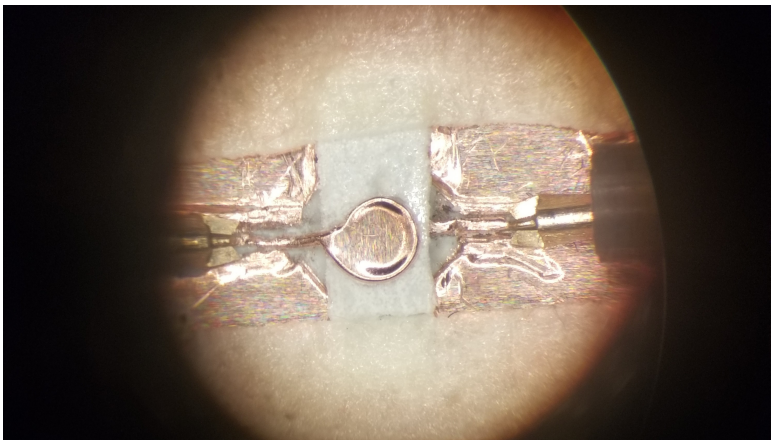

Figure 6.15: Microscope image of BST varactor and Picoprobes landed for measurement

varactors a probing station was used connected to a VNA and power supply for DC bias as seen in Figure 6.16. A variable 25 V power supply was used to provide the DC bias across the plates. Rather than use external bias tees at the probe ports, the power supply was connected through the VNA internal bias tees. The rest of the measurement process was

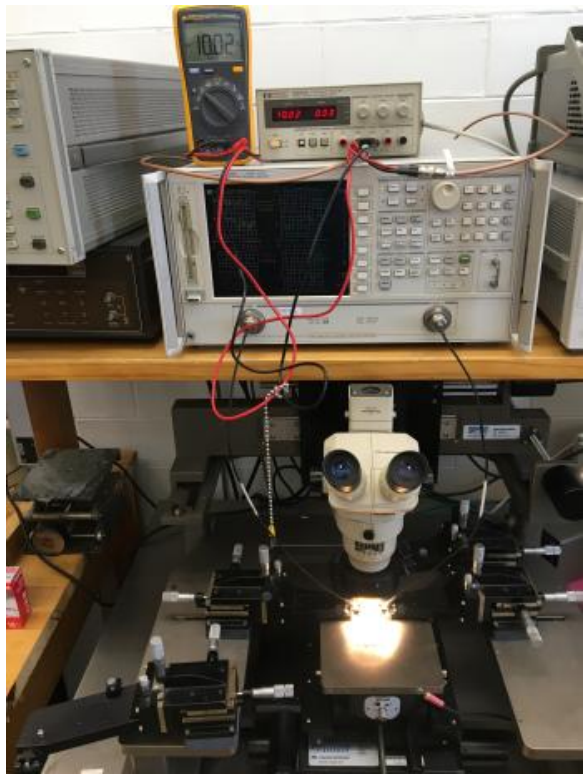

Figure 6.16: Varactor probing station with VNA, DMM and 25 V variable DC power supply

performed with the same methodology used for the SMA connected varactors with the DC power supplies connected for the unbiased points for consistency. Starting with the unbiased measurement, the DC power supply was powered on with the output set to 0 V while 2-port S-parameter data was measured with the VNA. After measuring the unbiased data point, the bias was increased to 10 V and verified across the varactor plates with a DMM before measuring the S-parameters for the 10 V bias point. Finally, the variable supply was set to 25 V and confirmed with a DMM before the S-parameter data was captured for the 25 V bias point.

To convert the measured S-parameter data to capacitance and quality factor data for the varactors, Equations (6.4) and (6.5) were used in conjunction with Equation (6.3). Comparing the measured results to the simulation using ferroelectric substrate values $\varepsilon_r = 3.4$ and $tan\delta = 0.25$, a reasonable likeness can be seen for the capacitance value at sub-GHz frequencies in Figure 6.17. At higher frequencies the physical varactors resonate just below 11 GHz

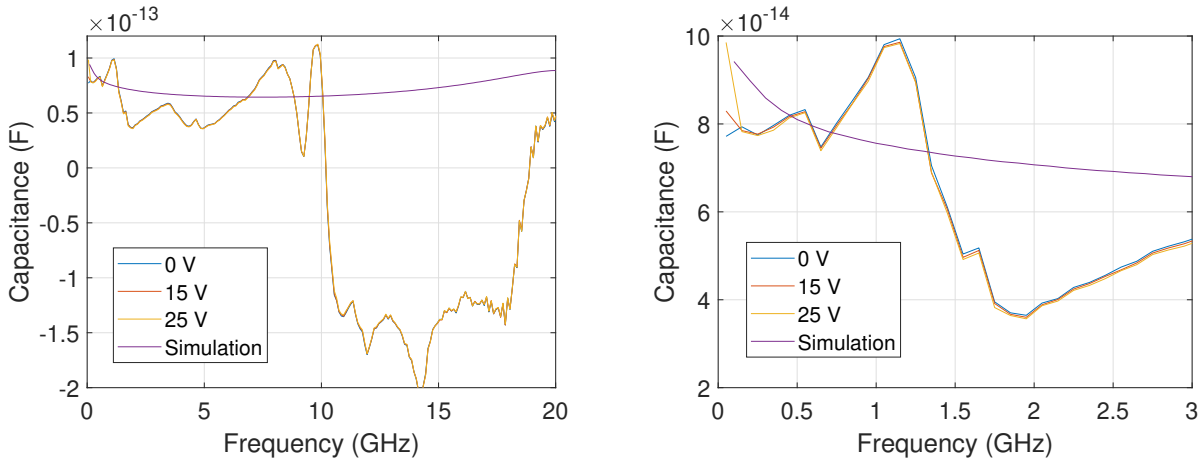

(a) (b)

Figure 6.17: Capacitance comparison between simulation and measurement for probed varactors using the ADS model for simulation from Figure 6.14 ($\varepsilon_r = 3.4$, $\tan\delta = 0.25$)

while the simulated varactors display no resonance upto 20 GHz. This could be due to the extra rounding in the feedline and ground plane causing additional paracitic capacitance at the input and output port.

The simulated quality factor shows a similar low frequency peak as the measured values in Figure 6.18 yet remains in the GHz range and does not display a resonance. It has been

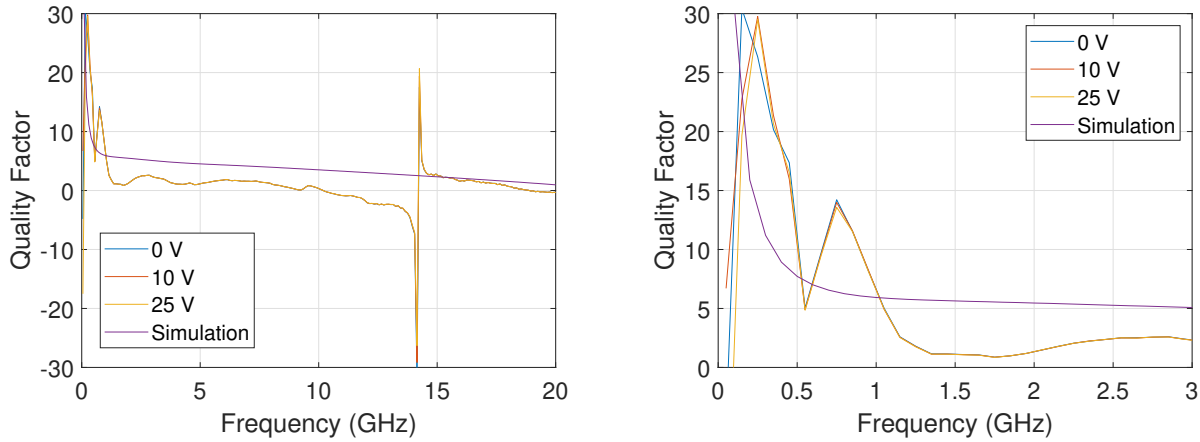

(a) (b)

Figure 6.18: Quality factor comparison between simulation and measurement for probed varactors using the ADS model for simulation from Figure 6.14 ($\varepsilon_r = 3.4$, $\tan\delta = 0.25$)

shown that printed material doped with BST can be used to make RF capacitors yet more

investigation could be done to improve the tunability and loss of the substrate. Figure 6.17 shows that the resonant frequency of the varactors can be brought above 10 GHz using the copper tape process yet the noise and variablity in these measurements makes the results seem less reliable compared to those presented for the larger SMA connected varactors. The results presented in this chapter demonstrate that 3D printing and the CNC knife tracing process can generate capacitors for use at sub-GHz frequencies. Figures 6.6 and 6.10 show that the 3 mm and 5 mm plate width varactors show stable capacitance around 6.7 pF and 1.2 pF respectively but more work should be done to improve the tunability of the substrate and resolution of the copper traces to make these capacitors tunable at GHz frequencies.

Chapter 7

Conclusions and Future Work

7.1 Conclusions

The electrical properties of SLA printable resin were characterised and used to produce three Luneburg lens antennas. These lenses were measured to improve the gain of a radiating element producing a beamforming effect, although more work needs to be done improving the reliability of the measured results. It was also shown that CNC knife tracing with a Cricut cutter and copper tape can be used to take advantage of copper's high bulk conductivity on delicate substrate materials for characterization of polymer and production of ferroelectric varactors.

The Luneburg lens was able to produce beamforming in x-band, in particular the 4.5 cm radius lens with 4 mm cells showed an increase in peak gain of 2.9 dB at 12 GHz over the bare waveguide. While these results are encouraging there is a great deal of noise and ripple present in the measurements which should be smoothed before increasing confidence in the measured results.

Cutting a microstrip Butler matrix with the knife tracing tool demonstrated how quickly a beam steering circuit can be made with relatively simple tools. Althouh the design should be limited to planar fabrication in future to eliminate disruption from poor contact creating

through hole vias and undefined tolerance cutting ground plane copper by hand. While the peak gain of the array was limited to 0.79 dB, some degree of beam steering was observed as a function of input port.

Design and assembly of the lumped element Matrix showed an alternative method for producing a four element phased array ideally suited to sug-GHz frequencies. The measured values for this design are still well outside what can be be accounted for by component variations. As the control design produced by standard PCB manufacturing it would seem that the most likely cause for error would be in the assembly and soldering of the board. Repeat copies should be assembled and checked for consistency as some level of damage or inconsistency among the components seems to be the only explanation for sure a large discrepancy.

Production and analysis of the ferroelectric varactors showed that capacitive circuits can be produced using 3D printing and CNC copper knife tracing. More work needs to be done on the substrate itself to improve tunability and the resolution of the knife tracing and assembly process needs to be improved to increase the self resonant frequency making the circuits appropriate for use at higher frequencies. A combination of these improvements could produce flexible varactors for use in GHz applications.

7.2 Future work

7.2.1 Luneburg lens antenna

While the Luneburg lens antennas improved gain of the feeding waveguide in the measurements that were taken, there is more work to be done removing variabilty in the measurements. One analysis would be a more thorough investigation into the impact of cell geometry on the performance of the lens. While a simple box cell was used for this design, the symmetric nature of the lens along the z-axis would make a cell design utilizing this geometry ideal. Rather than creating a box cell it could be made rectangular with solid walls along the

z-axis. This would allow for higher density at a given box width making the gaps between fill boxes necessarily larger. This could help with the merging issues experiences for the 2 mm cells.

7.2.2 Microstrip Butler matrix

Further work on the microstrip matrix should include an investigation of the S-parameters across the device by removing the array and measuring at the array ports. This could provide some valuable insight for troubleshooting the radiation pattern. A design should also be manufactured on a single layer to more accurately reflect the capabilities of the CNC cutting process rather than be obscured by the tolerances of manual alignment for drilling and cutting of the bottom conductor.

7.2.3 Lumped Butler matrix

Another board should be assembled for the lumped matrix to compare with the existing model. It seems that the errors present for this circuit are too significant to be explained by tolerances and therefor might be the result of damage somewhere on the board. Assembly of an additional unit would allow for comparison to find consistencies or potentially validate the simulated results.

Another lumped matrix could be designed using a more advanced IC technology such as CMOS. This would allow far more control over the lumped components involved and the whole circuit could be simulated to extract the S-Parameters at the frequency of interest. A CMOS IC would be significantly more expensive than surface mount components on FR4 but could allow the frequency of operation to be significantly increased.

7.3 Ferroelectric varactors

To improve on the varactors, an investigation should be done into the printed BST. Examples in literature have shown a high permittivity and tuning range from doped BST nano-particles [68]. Increasing the tunability of the substrate is important for making the capacitor circuits tunable varactors. In addition to investigating the printed BST chemistry the varactors could be designed to reduce the gap between electrodes for increased bias at low voltage levels. A combination of more sensitive substrate material with a stronger electric field bias would be a large increase to varactor's tunability with bias voltage.

These capacitors should also be integrated into a flexible device for application demonstration. As a flexible device they would be an ideal candidate for integration into wearable technology. In conjunction with a printed inductor the capacitors could be used to generate a bandpass input filter for a transceiver or to impedance match a flexible antenna.

Bibliography

[1] Brian Keogh and Anding Zhu. "Wideband self-interference cancellation for 5G full-duplex radio using a near-field sensor array". In: *2018 IEEE MTT-S International Microwave Workshop Series on 5G Hardware and System Technologies (IMWS-5G)*. 2018, pp. 1–3. DOI: 10.1109/IMWS-5G.2018.8484398.

[2] Pilsoon Choi, Dimitri A. Antoniadis, and Eugene A. Fitzgerald. "Towards Millimeter-Wave Phased Array Circuits and Systems For Small Form Factor and Power Efficient 5G Mobile Devices". In: *2019 IEEE International Symposium on Phased Array System Technology (PAST)*. 2019, pp. 1–5. DOI: 10.1109/PAST43306.2019.9021005.

[3] Cricut. *Cricut Shop - Cricut Maker*. URL: https://cricut.com/en_us/machines/cricut-maker-machines/cricut-maker.html (visited on 12/05/2021).

[4] Trevor S. Bird. *Fundamentals of Aperture Antennas and Arrays : From Theory to Design, Fabrication and Testing*. First. West Sussex, U.K.: Wiley, 2008.

[5] Alexey Korotkov and Yuriy Mitelman. "Comparison of luneburg lens antennas made from homogeneous material". In: *2018 Ural Symposium on Biomedical Engineering, Radioelectronics and Information Technology (USBEREIT)*. 2018, pp. 334–337. DOI: 10.1109/USBEREIT.2018.8384617.

[6] Riccardo Colella et al. "Customizing 3D-Printing for Electromagnetics to Design Enhanced RFID Antennas". In: *IEEE Journal of Radio Frequency Identification* 4.4 (2020), pp. 452–460. DOI: 10.1109/JRFID.2020.3001043.

[7] Philippe Ratajczak. "Design of a 3D Printed Luneburg Lens Antenna for Multiple Beams Applications at mm-wave Frequencies". In: *2019 13th European Conference on Antennas and Propagation (EuCAP)*. 2019, pp. 1–4.

[8] Bhavana Deore et al. "Direct printing of functional 3D objects using polymerization-induced phase separation". In: *Nature Communications* 12.1 (2021), p. 55. DOI: 10.1038/s41467-020-20256-3.

[9] John M. Jordan. *3D Printing*. First. Cambridge: MIT Press, 2019.

[10] Joan Horvath. *Mastering 3D Printing*. First. CA: Apress: Berkeley, 2014.

[11] Formlabs. *High Performance 3D Printers, Finally Within Reach*. URL: https://formlabs.com/ (visited on 05/25/2022).

[12] Prusa Research. *Original Prusa i3 MK3S+*. URL: https://formlabs.com/ (visited on 05/25/2022).

[13] Machine Design. *What's the Difference Between Stereolithography and Selective Laser Sintering?* URL: https://www.machinedesign.com/3d-printing-cad/article/21831851/whats-the-difference-between-stereolithography-and-selective-laser-sintering (visited on 05/25/2022).

[14] Hubs. *What is FDM (Fused Deposition Modeling) 3D printing?* URL: https://www.hubs.com/knowledge-base/what-is-fdm-3d-printing/ (visited on 05/25/2022).

[15] Hossein Saghlatoon et al. "X band 3D-Printed Electrically-Small Luneburg Lens". In: *2020 IEEE International Symposium on Antennas and Propagation and North American Radio Science Meeting*. 2020, pp. 1465–1466. DOI: 10.1109/IEEECONF35879.2020.9329820.

[16] L. C. Gunderson and G. T. Holmes. "Microwave luneburg lens". In: *Applied Optics*. Vol. 7. 5. 1968, pp. 801–804. DOI: 10.1109/MWSYM.2011.5972738.

[17] Benjamin Fuchs et al. "Design Optimization of Multishell Luneburg Lenses". In: *IEEE Transactions on Antennas and Propagation* 55.2 (2007), pp. 283–289. DOI: 10.1109/TAP.2006.889849.

[18] Zachary Larimore et al. "Additive Manufacturing of Luneburg Lens Antennas Using Space-Filling Curves and Fused Filament Fabrication". In: *IEEE Transactions on Antennas and Propagation* 66.6 (2018), pp. 2818–2827. DOI: 10.1109/TAP.2018.2823819.

[19] Min Liang et al. "An X-band Luneburg Lens antenna fabricated by rapid prototyping technology". In: *2011 IEEE MTT-S International Microwave Symposium*. 2011, pp. 1–4. DOI: 10.1109/MWSYM.2011.5972738.

[20] Yue Dong, Xin Min, and Woo Soo Kim. "A 3-D-Printed Integrated PCB-Based Electrochemical Sensor System". In: *IEEE Sensors Journal* 18.7 (2018), pp. 2959–2966. DOI: 10.1109/JSEN.2018.2801459.

[21] U. Daalkhaijav et al. "Rheological modification of liquid metal for additive manufacturing of stretchable electronics". In: *Adv. Mater. Technol* 3.4 (2018), p. 1700351.

[22] Callen Votzke et al. "3D-Printed Liquid Metal Interconnects for Stretchable Electronics". In: *IEEE Sensors Journal* 19.10 (2019), pp. 3832–3840. DOI: 10.1109/JSEN.2019.2894405.

[23] Eric Macdonald et al. "3D Printing for the Rapid Prototyping of Structural Electronics". In: *IEEE Access* 2 (2014), pp. 234–242. DOI: 10.1109/ACCESS.2014.2311810.

[24] Chiyen Kim et al. "3D Printed Electronics With High Performance, Multi-Layered Electrical Interconnect". In: *IEEE Access* 5 (2017), pp. 25286–25294. DOI: 10.1109/ACCESS.2017.2773571.

[25] Khaled Alhassoon et al. "Broadband RF Characterization and Extraction of Material Properties in 3-D Printed Composite Substrates for Magnetically Tuned Circuits". In: *IEEE Transactions on Microwave Theory and Techniques* 69.3 (2021), pp. 1703–1710. DOI: 10.1109/TMTT.2020.2971979.

[26] Ryan Bahr et al. "RF characterization of 3D printed flexible materials - NinjaFlex Filaments". In: *2015 European Microwave Conference (EuMC)*. 2015, pp. 742–745. DOI: 10.1109/EuMC.2015.7345870.

[27] K. Alhassoon et al. "Broadband and Accurate Material Characterization of 3D Manufactured RF Structures". In: *2018 IEEE MTT-S International Microwave Workshop Series on Advanced Materials and Processes for RF and THz Applications (IMWS-AMP)*. 2018, pp. 1–3. DOI: 10.1109/IMWS-AMP.2018.8457147.

[28] J.-M. Heinola, K.-P. Latti, and P. Silventoinen. "Dielectric characterization of printed wiring board materials: a comparison of ring and T-resonator based measurement methods". In: *CEIDP '05. 2005 Annual Report Conference on Electrical Insulation and Dielectric Phenomena, 2005.* 2005, pp. 629–632. DOI: 10.1109/CEIDP.2005.1560761.

[29] Ligin Alphonsa and R. Resmi. "S parameter analysis of split ring resonator for various substrate materials". In: *2017 International Conference on Circuit ,Power and Computing Technologies (ICCPCT)*. 2017, pp. 1–6. DOI: 10.1109/ICCPCT.2017.8074194.

[30] J.R. Bray and L. Roy. "Microwave characterization of a microstrip line using a two-port ring resonator with an improved lumped-element model". In: *IEEE Transactions on Microwave Theory and Techniques* 51.5 (2003), pp. 1540–1547. DOI: 10.1109/TMTT.2003.810136.

[31] D. Preetha and T. Jayanthy. "Analysis of different types of coupling for microstrip ring resonator". In: *2014 International Conference on Science Engineering and Management Research (ICSEMR)*. 2014, pp. 1–5. DOI: 10.1109/ICSEMR.2014.7043561.

[32] Keysight. *85052D Economy Mechanical Calibration Kit, DC to 26.5 GHz, 3.5 mm.* URL: https://www.keysight.com/ca/en/product/85052D/economy-mechanical-calibration-kit-dc-26-5-ghz-3-5-mm.html (visited on 03/27/2022).

[33] Keysight. *PathWave Advanced Design System (ADS).* URL: https://www.keysight.com/zz/en/products/software/pathwave-design-software/pathwave-advanced-design-system.html (visited on 03/25/2022).

[34] MathWorks. *MATLAB.* URL: https://www.mathworks.com/products/matlab.html (visited on 03/25/2022).

[35] David M. Pozar. *Microwave Engineering.* New York, N.Y.: John Wiley and Sons, 1998.

[36] Rudolf Karl Luneburg and Max Herzberger. *Mathematical Theory of Optics.* First. Berkeley: University of California Press: IEEE Press, 1964.

[37] Carl Pfeiffer and Anthony Grbic. "A Printed, Broadband Luneburg Lens Antenna". In: *IEEE Transactions on Antennas and Propagation* 58.9 (2010), pp. 3055–3059. DOI: 10.1109/TAP.2010.2052582.

[38] G. Peeler and H. Coleman. "Microwave stepped-index luneberg lenses". In: *IRE Transactions on Antennas and Propagation* 6.2 (1958), pp. 202–207. DOI: 10.1109/TAP.1958.1144575.

[39] Ryan A. Bahr et al. "3D-Printed Omnidirectional Luneburg Lens Retroreflectors for Low-Cost mm-Wave Positioning". In: *2020 IEEE International Conference on RFID (RFID).* 2020, pp. 1–7. DOI: 10.1109/RFID49298.2020.9244891.

[40] Yangbo Xie et al. "Microwave metamaterials made by fused deposition 3D printing of a highly conductive copper-based filament". In: *Applied Physics Letters* (2017). DOI: 10.1063/1.4982718.

[41] Chun-Wei Pan, Malcolm Ng Mou Kehn, and Oscar Quevedo-Teruel. "Microwave focusing lenses by synthesized with positive or negative refractive index split-ring resonator metamaterials". In: *2015 International Workshop on Electromagnetics: Applications and Student Innovation Competition (iWEM).* 2015, pp. 1–2. DOI: 10.1109/iWEM.2015.7365057.

[42] Esra Doğan, Emin Unal, and Dilek Kapusuz. "New generation WIMAX antenna based on metamaterial superstrate". In: *Journal of Optoelectronics and Advanced Materials* 7.11-12 (2013), pp. 1002–1010.

[43] Anrong Chen and Tao Yang. "A Folded Planar Luneburg Lens for Multi-Beams Antennas Application". In: *2021 IEEE MTT-S International Wireless Symposium (IWS).* 2021, pp. 1–3. DOI: 10.1109/IWS52775.2021.9499349.

[44] A. N. Korotkov, S. N. Shabunin, and V. A. Chechetkin. "The cylindrical luneburg lens discretization influence on its radiation parameters". In: *2017 International Multi-Conference on Engineering, Computer and Information Sciences (SIBIRCON)*. 2017, pp. 394–398. DOI: 10.1109/SIBIRCON.2017.8109914.

[45] Shiyu Zhang et al. "3D-printed graded index lens for RF applications". In: *2016 International Symposium on Antennas and Propagation (ISAP)*. 2016, pp. 90–91.

[46] Ashutosh Patri and Jayanta Mukherjee. "Fish-eye shaped dielectric flat lens design utilizing 3-D printing technology". In: *2016 IEEE International Symposium on Antennas and Propagation (APSURSI)*. 2016, pp. 1843–1844. DOI: 10.1109/APS.2016.7696628.

[47] Sebastian G. Wirth and Ivor L. Morrow. "Near-Field Microwave Sensor Composed of 3D Printed Antennas and Lenses". In: *2018 IEEE MTT-S International Conference on Numerical Electromagnetic and Multiphysics Modeling and Optimization (NEMO)*. 2018, pp. 1–4. DOI: 10.1109/NEMO.2018.8503209.

[48] F. Gaufillet and É. Akmansoy. "Graded Photonic Crystals for Luneburg Lens". In: *IEEE Photonics Journal* 8.1 (2016), pp. 1–11. DOI: 10.1109/JPHOT.2016.2521261.

[49] Injoong Nam et al. "Advanced Lens for Antenna Gain Enhancement using 3D Printing Technology". In: *2018 International Symposium on Antennas and Propagation (ISAP)*. 2018, pp. 1–2.

[50] Xudong Chen et al. "Robust method to retrieve the constitutive effective parameters of metamaterials". In: *Physical Review E* 70 (1 July 2004), p. 016608. DOI: 10.1103/PhysRevE.70.016608. URL: https://link.aps.org/doi/10.1103/PhysRevE.70.016608.

[51] Nagui Mikhail. *Anechoic Chamber Horn Antenna Catalog*. 2009. URL: http://www.doe.carleton.ca/~nagui/labequip/antenna/horn_antennas.pdf (visited on 11/20/2021).

[52] Han Ren et al. "A Novel Design of 4 × 4 Butler Matrix With Relatively Flexible Phase Differences". In: *IEEE Antennas and Wireless Propagation Letters* 15 (2016), pp. 1277–1280. DOI: 10.1109/LAWP.2015.2504719.

[53] S. Abdullah et al. "A First Implementation of a Single-Layer 4x4 Butler Matrix on Flexible PET Using Printed Silver". In: *2021 IEEE USNC-CNC-URSI North American Radio Science Meeting (Joint with AP-S Symposium)*. 2021, pp. 1–2.

[54] Ali Tajik, Ahmad Shafiei Alavijeh, and Mohammad Fakharzadeh. "Asymmetrical 4 × 4 Butler Matrix and its Application for Single Layer 8 × 8 Butler Matrix". In: *IEEE Transactions on Antennas and Propagation* 67.8 (2019), pp. 5372–5379. DOI: 10.1109/TAP.2019.2916695.

[55] Yue Cao et al. "A Compact 38 GHz Multibeam Antenna Array With Multifolded Butler Matrix for 5G Applications". In: *IEEE Antennas and Wireless Propagation Letters* 16 (2017), pp. 2996–2999. DOI: 10.1109/LAWP.2017.2757045.

[56] Zulfi and Achmad Munir. "Experimental Characterization of Miniaturized Meander Line-Based 4×4 Butler Matrix". In: *2021 IEEE International Conference on Communication, Networks and Satellite (COMNETSAT)*. 2021, pp. 258–262. DOI: 10.1109/COMNETSAT53002.2021.9530781.

[57] Krzysztof Wincza and Slawomir Gruszczynski. "Miniaturized broadband 4 × 4 Butler matrix designed with the use of quasi-lumped coupled-line couplers". In: *2012 8th International Caribbean Conference on Devices, Circuits and Systems (ICCDCS)*. 2012, pp. 1–4. DOI: 10.1109/ICCDCS.2012.6188906.

[58] Lu Ning and Liguo Sun. "Design of compact 4×4 X-band Butler with lump element based on IPD technology". In: *2013 Proceedings of the International Symposium on Antennas Propagation*. Vol. 01. 2013, pp. 492–495.

[59] Shakeeb Abdullah et al. "A New Closed-Form Approach (Equation) for Accurately Predicting the Efficiency of Square Patch Planar Antennas". In: *2021 IEEE 19th International Symposium on Antenna Technology and Applied Electromagnetics (ANTEM)*. 2021, pp. 1–2. DOI: 10.1109/ANTEM51107.2021.9518992.

[60] Pasternack Enterprise. *Microstrip Patch Antenna Calculator*. URL: https://www.pasternack.com/t-calculator-microstrip-ant.aspx?gclid=Cj0KCQiA_c-0BhDFARIsAIFg3ewpaFguo5S4ooTMeKZ5N26v7waQXM0-Ziq_wD9lhI_G3E1y4vDBqAAaAkdiEALw_wcB (visited on 09/12/2021).

[61] Rogers Corporation. *RO3006 Laminates*. URL: https://rogerscorp.com/advanced-electronics-solutions/ro3000-series-laminates/ro3006-laminates (visited on 03/27/2022).

[62] Jian-An Hou and Yeong-Her Wang. "A Compact Quadrature Hybrid Based on High-Pass and Low-Pass Lumped Elements". In: *IEEE Microwave and Wireless Components Letters* 17.8 (2007), pp. 595–597. DOI: 10.1109/LMWC.2007.901775.

[63] Robert J. Weber. *Introduction to Microwave Circuits: Radio Frequency and Design Applications*. First. New York, N.Y.: IEEE Press, 2015.

[64] Spartak Gevorgian. *Ferroelectrics in Microwave Devices, Circuits and Systems*. London, U.K.: Springer, 2009.

[65] M.H. Weatherspoon and L.P. Dunleavy. "Experimental validation of generalized equations for FET cold noise source design". In: *IEEE Transactions on Microwave Theory and Techniques* 54.2 (2006), pp. 608–614. DOI: 10.1109/TMTT.2005.862674.

[66] M. Seif et al. "Characterization, modeling and comparison of 1/f noise in Si/SiGe:C HBTs issued from three advanced BiCMOS technologies". In: *2017 29th International Conference on Microelectronics (ICM)*. 2017, pp. 1–4. DOI: 10.1109/ICM.2017.8268847.

[67] N. O. Sadiku Matthew. *Elements of Electromagnetics*. Sixth. New York, N.Y.: Oxford University Press, 2015.

[68] Mahdi Haghzadeh, Craig Armiento, and Alkim Akyurtlu. "All-Printed Flexible Microwave Varactors and Phase Shifters Based on a Tunable BST/Polymer". In: *IEEE Transactions on Microwave Theory and Techniques* 65.6 (2017), pp. 2030–2042. DOI: 10.1109/TMTT.2017.2659227.

[69] Mahmoud Al Ahmad et al. "Wide-Tunable Low-Field Interdigitated Barium Strontium Titanate Capacitors". In: *IEEE Microwave and Wireless Components Letters* 17.11 (2007), pp. 769–771. DOI: 10.1109/LMWC.2007.908044.

[70] Haixiang Sun et al. "Optimizing the Electrical Conductivity of Screen Printed Silver Conductive Tracks by Post Treatment". In: *2018 International Flexible Electronics Technology Conference (IFETC)*. 2018, pp. 1–3. DOI: 10.1109/IFETC.2018.8583905.

[71] Gaozhi George Xiao et al. "Screen printing RF antennas". In: *2016 17th International Symposium on Antenna Technology and Applied Electromagnetics (ANTEM)*. 2016, pp. 1–2. DOI: 10.1109/ANTEM.2016.7550245.

[72] James C. Rautio. "N -Port T-Networks and Topologically Symmetric Circuit Theory". In: *IEEE Transactions on Microwave Theory and Techniques* 58.4 (2010), pp. 705–709. DOI: 10.1109/TMTT.2010.2041516.

[73] GGB Industries. *PICOPROBE MODEL 40A*. 2017. URL: https://ggb.com/home/model-40a/ (visited on 06/10/2021).

[74] Rogers Corporation. *RO4350B Laminates*. URL: https://rogerscorp.com/advanced-electronics-solutions//ro4000-series-laminates/ro4350b-laminates (visited on 03/27/2022).